Hall Magnetometry of Electrodeposited Superconducting Pb Mesostructures

Engbarth, Miles

Award date:
2010

Awarding institution:
University of Bath

HALL MAGNETOMETRY OF ELECTRODEPOSITED SUPERCONDUCTING PB MESOSTRUCTURES

Miles Engbarth

A thesis submitted for the degree of Doctor of Philosophy

University of Bath

Department of Physics

April 2010

Abstract

Hall probe magnetometry measurements have been used to investigate the magnetic state of various Pb microcrystals grown by electrodeposition, where careful control of deposition parameters has allowed the tuning of their architectures. The internal flux distribution when in the superconducting state is seen to be highly dependent on the size and geometry of the investigated samples. In nanowires single flux vortex states are seen to form, showing typical type II behaviour. As the diameter of the nanowires increases these vortex states are seen to bunch together, behaviour that begins to approach that of a type I superconductor. Measurements of Pb triangles with sloped sides show the formation of giant vortex states typical of type I behaviour. These results also highlight the importance of geometry on surface barriers and the corresponding effect these have on flux distribution. Investigation of an icosahedron shows how symmetry effects can determine the stability of different flux states. Experimental results are in good agreement with Ginzburg-Landau calculations.

Acknowledgements

I would like to thank my supervisor Prof. S. J. Bending for giving me the opportunity to undertake this work and for his encouragement, support and enthusiasm throughout all its stages.

The Ginzburg-Landau simulations presented in this work were all carried out by Dr. M. V. Miloševič (Department of Physics, University of Bath and Departement Fysica, Universiteit Antwerpen) who has helped to provide invaluable insight into the workings of mesoscopic superconductors. The technicians from the University of Bath have provided a great deal of help throughout the course of this work, and I would like to thank Dr. Spartaco Landi, Wendy Lambson, Bob Draper and Paul Reddish in particular.

Many thanks go to the members of the Nanosciences Group, particularly Nick Lambert, John Neal, Malcolm Connolly, Sara Dale and André Müller.

Finally I would like to thank my family and friends for all their support and encouragement over the years.

Contents

Chapter 1

Overview

1.1 Motivation

Superconductivity is a macroscopic quantum phenomenon characterised by dissipationless supercurrents and perfect diamagnetism. Bulk superconductors are divided into either type I or type II on the basis of their magnetic properties; ideal type I materials exhibit perfect diamagnetism up to a critical field, H_c, while type II materials allow the penetration of flux-quantised vortices in the mixed state above a lower critical field, H_{c1}. This simple division, however, breaks down completely in mesoscopic superconductors (whose sizes are comparable to the superconducting coherence length, ξ) due to boundary conditions imposed on the order parameter by the geometrical confinement as well as surface barriers and demagnetising effects.

It is well known that arbitrarily-shaped bulk type I samples do not exhibit perfect diamagnetism all the way up to the critical field, H_c. Shape-dependent demagnetising effects lead to an enhancement of the surface fields and, once these reach H_c, flux penetrates into the body of the sample. The intermediate state formed consists of coexisting superconducting and normal domains, and the latter can have complex structures and topologies, organising themselves so that the maximum local fields are limited to H_c. Indeed, magneto-optic imaging has recently been used to revisit the problem of the equilibrium structure of the intermediate state in bulk Pb with compelling new evidence that it corresponds to an array

of flux tubes [1] rather than the lamella-like domains proposed by Landau many years ago [2]. Recent modelling of small, although not strictly mesoscopic, type I superconducting squares [3] reveals complex geometric flux patterns that conform with the square sample symmetry due to interactions with the surface barriers. As the size of type I samples is reduced to mesoscopic dimensions such geometric confinement becomes stronger still. Indeed the intermediate state may even become energetically unstable, while superconductivity can actually be enhanced at surfaces which are parallel to an applied magnetic field (surface superconductivity). As a consequence the flux structures formed become intimately dependent on the size, shape and symmetry of the samples investigated.

Many important investigations of mesoscopic superconductors have been reported to date, but nearly all have used nanopatterned polycrystalline films, [4], [5], [6], in which disorder and thin film geometry lead to type II behaviour. Recent breakthroughs in electrocrystallisation on HOPG substrates [7], however, allow one to grow single crystal lead structures that are clean enough and wide enough to remain type I, but small enough to exhibit striking mesoscopic effects.

Hall probe magnetometry [8] offers an ideal approach for the magnetic characterising of such mesoscopic samples allowing single flux quantum resolution at low temperatures in a wide range of magnetic fields.

1.2 Structure of Thesis

The thesis begins with a broad overview of superconductivity in Chapter 2. This introduces the phenomenological theories of superconductivity that in turn describe the superconducting lengthscales which are fundamental in determining superconducting behaviour. The important differences in type I and type II superconductors is described and focus is given to the behaviour of type I superconductors in magnetic fields. Chapter 3 gives an introduction to electrodeposition and the methods used during the course of this work to fabricate samples. Chapter 4 explains how Hall probes can be used to characterise the magnetic properties of superconductors and goes on to describe their fabrication and the experimental method employed in using them. The final three chapters detail the results of magnetisation measurements of different mesoscopic samples. Chapter 5 deals with Pb nanowires of different thicknesses. Chapter 6 presents results obtained for 3D Pb triangles and Chapter 7 describes the strongly geometry related flux

structures of an icosahedron and tripod. The conclusions to these investigations are presented in Chapter 8 along with suggestions for further work.

Chapter 2

Introduction to Superconductivity

2.1 History

Superconductivity was discovered in 1911 by Heike Kamerlingh Onnes [9]. In 1908 Onnes managed to liquefy helium for the first time [10], which he used to study the resistivity, ρ, of metals at low temperature. It was unknown at the time how ρ would behave at low temperature. Some, like Onnes, believed that ρ would drop with temperature and for a pure metal would eventually go to zero at zero temperature. Others thought that it would level out at some low temperature, whilst some thought that close to absolute zero the electrons would freeze, effectively making ρ infinite. Onnes first experimented on gold at low temperature and found that ρ became constant and not zero, which he attributed to impurities in the gold. Onnes could only make mercury (Hg) purer than gold and whilst experimenting with this observed that instead of following any of the expected behaviours ρ suddenly dropped to an immeasurably small value at about 4.2K (figure 2.1).

Onnes realised that the Hg had passed into a new, superconducting state. It was soon shown that several other metals and alloys, including tin (Sn) and lead (Pb) [11], also displayed perfect conductivity when cooled to a critical temperature, T_c, and carrying a current less than a critical current density, J_c.

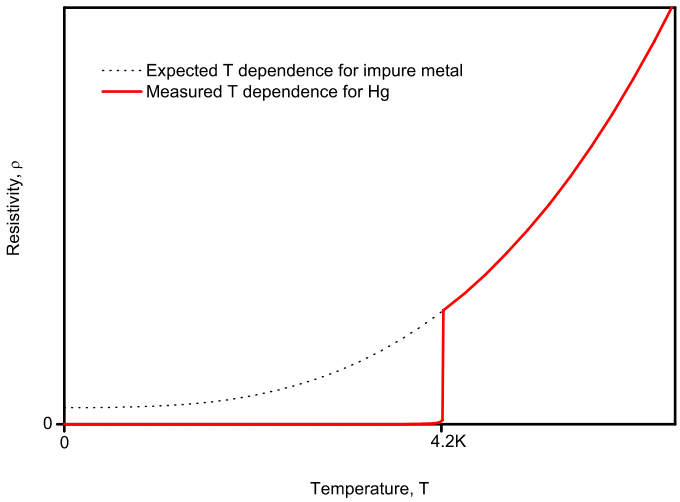

Figure 2.1: Expected temperature dependence of ρ alongside the temperature dependence as measured by Onnes for Hg.

2.2 The Meissner Effect

In 1933 Meissner and Ochsenfeld [12] discovered a second fundamental characteristic of superconductors in that they display perfect diamagnetism, their magnetic susceptibility, χ, is -1. They found that a magnetic field, below a temperature dependent critical field strength $H_c(T)$, applied to a superconductor is expelled from the interior of the superconductor resulting in the magnetisation curve shown in figure 2.3. Not only this, but any field smaller than $H_c(T)$ that permeates a body in the normal state will be expelled from the body when it enters the superconducting state. This is a critical difference between a superconductor and a perfect conductor, which would be expected to trap flux in the body as illustrated in figure 2.2.

The Meissner effect is a result of spontaneously induced surface supercurrents that perfectly cancel the field inside the superconductor, whilst reinforcing the field outside it. Logically these currents can not exist solely at the surface, as this would involve an infinite current density, and hence decay over some characteristic lengthscale into the superconductor. The discovery of the Meissner effect was an important step in understanding superconductivity and it demonstrated that superconductivity is more than just perfect conduction.

A superconductor becomes normal when a critical magnetic field is applied because the change in energy caused by the magnetic field cancels the free energy difference between the normal and superconducting state. Any material acquires

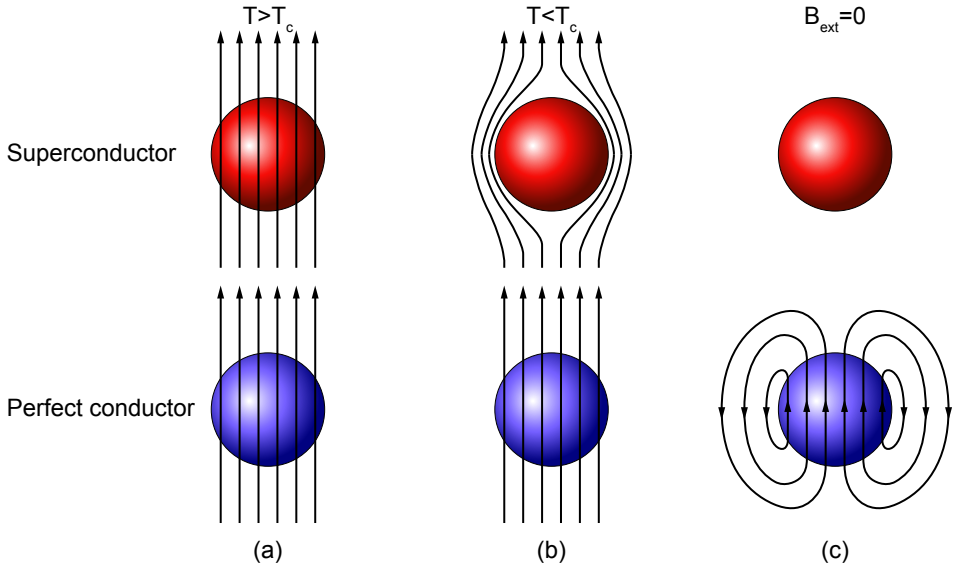

Figure 2.2: Comparison of superconducting and perfectly conducting spheres in a magnetic field. (a) In the resistive regime both spheres behave the same allowing the applied field to penetrate. (b) Below the critical temperature the resistance drops to zero, the superconductor expels the field whilst the perfect conductor still allows field to penetrate. (c) Still below the critical temperature the external field is removed, there is zero field in the superconductor but flux is trapped in the perfect conductor.

a magnetisation, M, in an applied field H_a. This causes a change in its free energy, ΔG

$$\Delta G(H_a) = -\mu_0 \int_0^{H_a} M.dH. \tag{2.1}$$

For a superconductor in the Meissner state $M = -H$ hence

$$\Delta G(H_a) = \frac{\mu_0 {H_a}^2}{2}. \tag{2.2}$$

2.3 The London Equations

By considering the consequences of zero resistance and assuming currents in superconductors are a result of the local magnetic field, F. London and H. London, [13], were able to define equations that went a long way to describing two of the key features of superconductivity. These equations are phenomenological in that they are not a logical consequence of fundamental principles, nor do they explain the cause of superconductivity.

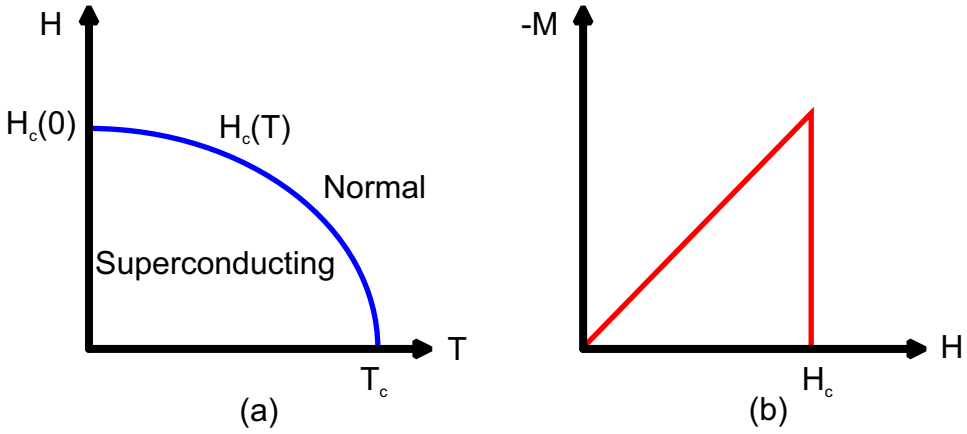

Figure 2.3: (a) Magnetic phase diagram for a superconductor showing the temperature dependence of the critical field. (b) Magnetisation curve for a superconductor.

By applying classical mechanics to electron motion and relating this to electrical conductivity the following relationship is obtained

$$m\frac{d\mathbf{v}}{dt} = e\mathbf{E} + \frac{m\mathbf{v}}{\tau}, \tag{2.3}$$

where τ is the damping time, that is, the typical time taken for an electrons velocity to go to zero due to scattering effects.

A key step in the formulation of the London equations is the assumption that the total electron density, n, in a superconductor can be split into a normal part, n_n, and a superconducting part, n_s. These are temperature dependent such that $n = n_s$ at $T = 0$ and n_s decreases continuously to zero at $T = T_c$. It would then be expected that while the normal electrons have a typical value for τ, the super electrons move without dissipation and hence have an infinite τ. The τ component can therefore be ignored from equation 2.3 as in the superconducting state all current is carried by the super electrons. Equation 2.3 therefore becomes

$$\frac{d\mathbf{v}_s}{dt} = \frac{e\mathbf{E}}{m}. \tag{2.4}$$

This can be taken in conjunction with the definition of current density ($\mathbf{J}$=ne$\mathbf{v}$), and taking the time derivative of both sides gives

$$\mathbf{E} = \frac{d}{dt}\left(\frac{m}{n_s e^2}\mathbf{J}_s\right), \tag{2.5}$$

where $\mathbf{J}_s$ is the supercurrent density. Equation 2.5 is the first London equation

and it describes perfect conductivity as there is no electric field in the superconductor unless the supercurrent is changing.

The Maxwell equation $\frac{d\mathbf{B}}{dt} = -\nabla \times \mathbf{E}$ can then be applied to equation 2.5 to get

$$\frac{d\mathbf{B}}{dt} = -\frac{m}{n_s e^2}\nabla \times \frac{d\mathbf{J}_s}{dt}. \tag{2.6}$$

Taking the time derivative of another Maxwell equation, $\nabla \times \mathbf{B} = \mu_0 \mathbf{J}_s$, and substituting this into equation 2.6, then after applying the vector identity $\nabla \times (\nabla \times \mathbf{A}) = \nabla(\nabla.\mathbf{A}) - \nabla^2\mathbf{A}$ and remembering that $\nabla.\mathbf{B} = 0$ the following is obtained

$$\frac{d\mathbf{B}}{dt} = \frac{m}{\mu_0 n_s e^2}\nabla^2 \frac{d\mathbf{B}}{dt}. \tag{2.7}$$

This suggests the screening of time-dependent magnetic fields. It does not however explain the Meissner effect which leads to the expulsion of a static field from a superconductor i.e. the screening of time independent magnetic fields. F. and H. London, knowing of the Meissner effect, suggested that equation 2.7 also applied to time independent magnetic fields such that

$$\mathbf{B} = \frac{m}{\mu_0 n_s e^2}\nabla^2 \mathbf{B}. \tag{2.8}$$

This can be simplified by defining

$$\lambda_L = \sqrt{\frac{m}{\mu_0 n_s e^2}}, \tag{2.9}$$

where λ_L has dimensions of length. Furthermore it can be shown [14] that the solution to equation 2.8 is

$$B(x) = B(0)e^{-x/\lambda_L}, \tag{2.10}$$

where x is the depth into the superconductor measured from the surface. Hence the magnetic field only penetrates to a depth λ_L within the superconductor (see figure 2.4) and it is possible to say that the field has been excluded from the centre of the superconductor i.e. the Meissner effect. λ_L is hence known as the penetration depth. As this is inversely related to the supercurrent density it follows that magnetic field penetration into the superconductor increases as T increases, with complete penetration when $T = T_c$.

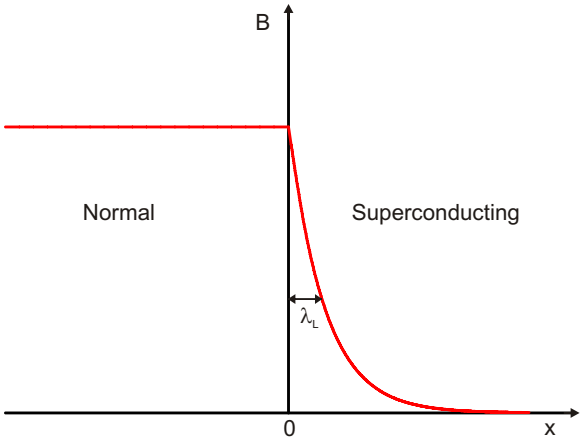

Figure 2.4: Decay of the magnetic flux density inside a superconductor over the penetration depth.

2.4 Ginzburg-Landau Theory

Unlike the London equations that are based on classical mechanics and electromagnetism, the Ginzburg-Landau (GL) theory [15] is based on quantum mechanics. It builds on earlier work by Landau on second order phase transitions [16] and presumes that the behaviour of superconducting electrons can be described by a complex pseudowavefuntion, ψ, such that

$$\psi(\mathbf{r}) = |\psi(\mathbf{r})|\, e^{i\phi(\mathbf{r})}. \tag{2.11}$$

It is also assumed that ψ can be used as an order parameter for the superconducting phase transition and so

$$n_s{}^* = |\psi|^2, \tag{2.12}$$

where $n_s{}^*$ is the supercurrent carrier density. This was perhaps an obvious choice, as an analogy can be drawn with superfluid liquid helium where it was known that $|\psi|^2$ can be used to describe the superfluid density. Because of this relationship, $|\psi|^2$ will equal zero when $T = T_c$. Ginzburg and Landau assumed that the free energy of the superconductor depended on $|\psi|^2$ (it could not depend on ψ as this is complex) and so expanded the free energy, $f(|\psi|^2(T))$, in a series in powers of $|\psi|^2$ via a Taylor expansion about the point $T = T_c$

$$f(|\psi|^2) = f(|\psi_0|^2) + \frac{df(|\psi_0|^2)}{d\,|\psi|^2}(|\psi|^2 - |\psi_0|^2) + \frac{1}{2}\frac{d^2 f(|\psi_0|^2)}{d\,|\psi|^4}(|\psi|^2 - |\psi_0|^2)^2 + \ldots \tag{2.13}$$

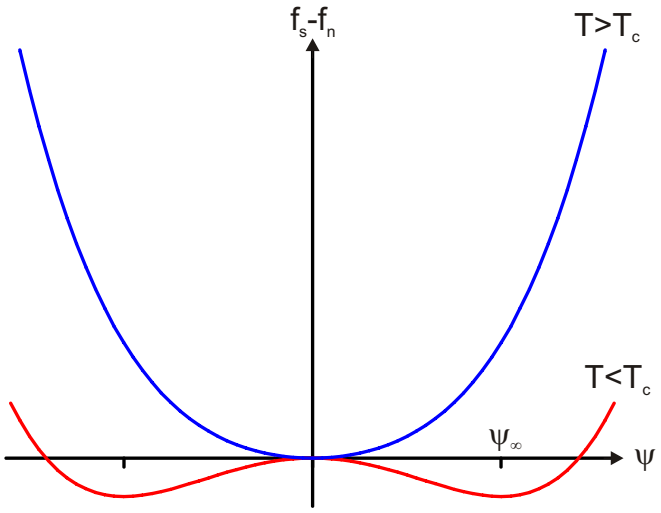

Figure 2.5: Free energy functions for T >T_c and T <T_c.

where $\psi_0 = \psi(T_c) = 0$, allowing the above to be simplified. It should also be noted that $f(|\psi_0|^2)$ is the free energy at $T = T_c$, i.e. the free energy of the normal state. It is reasonable to ignore terms beyond $|\psi|^4$ so long as T is close to T_c where $|\psi|^2 \to 0$. Considering this, and by defining coefficients $\alpha(T)$ and $\beta(T)$ so that they replace the differential components, equation 2.13 is simplified to

$$f_s = f_n + \alpha(T)\,|\psi|^2 + \frac{\beta(T)}{2}\,|\psi|^4\,, \tag{2.14}$$

where f_s and f_n are the superconducting and normal free energy densities respectively. By inspection of equation 2.14 it is apparent that for physical solutions to this equation β must be positive, else the minimum energy will be achieved for arbitrarily high values of $|\psi|^2$. By differentiating equation 2.14 with respect to ψ the minimum free energy, and hence the most stable state, is determined by

$$\alpha\psi + \beta\,|\psi|^2\,\psi = 0. \tag{2.15}$$

This has the trivial solution of $|\psi|^2 = 0$, but only represents the minimum energy for $\alpha > 0$ corresponding to the normal state ($T > T_c$). For $\alpha < 0$ the minimum energy obtained from equation 2.15 is

$$|\psi|^2 = {n_s}^* = -\frac{\alpha}{\beta}. \tag{2.16}$$

This is illustrated in figure 2.5, where the label ψ_∞ is used because ψ only reaches this value infinitely deep into a superconductor.

Because $\alpha(T)$ is negative below T_c and positive above T_c it can be said that $\alpha(T_c) = 0$. It is therefore reasonable to perform a Taylor expansion of $\alpha(T)$ for values of $T \approx T_c$, keeping only the first term to get

$$\alpha(T) = \alpha'(T - T_c), \tag{2.17}$$

where α' is a constant, this highlights the temperature dependence of α near T_c.

So far it has been assumed that the system is homogeneous, that is ${n_s}^*$ is constant and the minimum energy is achieved by $\psi = \psi_\infty$ everywhere. For real superconductors boundary conditions must be considered that will impose fields, currents and gradients. It is not obvious how electromagnetic fields should couple to the system, for instance there is no analogue in superfluid helium, but Ginzburg and Landau correctly drew a direct parallel with quantum mechanics where the kinetic energy in a magnetic field is given by

$$\frac{1}{2m^*} \left|(-i\hbar\nabla - e^*\mathbf{A})\psi\right|^2. \tag{2.18}$$

Here m^* is the mass of the supercurrent charge carrier[1] and e^* is its charge and $\mathbf{A}$ is the electromagnetic vector potential, where $\mathbf{B} = \nabla \times \mathbf{A}$. Here $-i\hbar\nabla - e^*\mathbf{A}$ is known as the canonical momentum, where the quantum mechanical momentum operator, $-i\hbar\nabla$, has been expanded to include the momentum associated with the vector potential, $e^*\mathbf{A}$. Combining this with the expression for the magnetic field in equation 2.2, the full expression for an inhomogeneous superconductor in a magnetic field becomes

$$f_s = f_n + \alpha(T)\left|\psi\right|^2 + \frac{\beta(T)}{2}\left|\psi\right|^4 + \frac{1}{2m^*}\left|(-i\hbar\nabla - e^*\mathbf{A})\psi\right|^2 + \frac{\mu_0 H^2}{2}. \tag{2.19}$$

Now instead of $\psi = \psi_\infty$ everywhere, $\psi(\mathbf{r})$ adjusts itself so that the overall free energy, which is given by the volume integral of equation 2.19, is minimised. This is a variational problem that can be solved by standard methods [18], the result of which are the famous GL equations

$$\alpha\psi + \beta\left|\psi\right|^2\psi + \frac{1}{2m^*}\left(-i\hbar\nabla - e^*\mathbf{A}\right)^2\psi = 0. \tag{2.20}$$

[1]This is known from BCS theory [17] to be a pair of electrons, the Cooper pair. Hence $e^* = 2e$, ${n_s}^* = n_s/2$ and $m^* = 2m$

$$\mathbf{J_s} = -\frac{ie^*\hbar}{2m^*}\left(\psi^*\nabla\psi - \psi\nabla\psi^*\right) - \frac{e^*}{m^*}\psi^*\psi\mathbf{A}, \tag{2.21}$$

where $\mathbf{J_s}$ is the supercurrent density.

A solution to equation 2.20 can be found by considering the simplified case of an inhomogeneous superconductor when no fields are present ($\mathbf{A} = 0$) [19], which leads to a characteristic length scale, ξ, being defined

$$\xi(T) = \sqrt{\frac{\hbar^2}{2m^*\left|\alpha\right|}}. \tag{2.22}$$

ξ is known as the GL coherence length and represents the shortest characteristic lengthscale over which $\psi(\mathbf{r})$ can vary.

This is not the first time a coherence length has been introduced. The Pippard coherence length ξ_0 was first suggested [20] to introduce non-local effects into the London equation, noting that n_s can only change over a finite lengthscale. This is different from the GL coherence length which diverges at T_c whilst ξ_0 remains constant. It may be somewhat confusing to use such similar notation for the two lengthscales, however they are related and at low temperature for sufficiently pure metals $\xi(T) \approx \xi_0$.

The other important lengthscale, the penetration depth from London theory equation 2.9, when combined with equation 2.16 of GL theory results in

$$\lambda(T) = \sqrt{\frac{m\beta}{2\mu_0\left|\alpha\right|e^2}} \tag{2.23}$$

Hence from equation 2.17 it is apparent that both $\xi(T)$ and $\lambda(T)$ depend on $\frac{T_c}{T_c - T}$, as shown in figure 2.6, and as a result the ratio

$$\kappa = \frac{\lambda(T)}{\xi(T)} \tag{2.24}$$

is constant for a given superconductor. κ is known as the GL parameter. This important result will be further explored in a later section.

The main limitation of the GL equations should be apparent from the method used to derive them, specifically that the elimination of higher terms from the power series expansion is only reasonable for when T is close to T_c. Nevertheless,

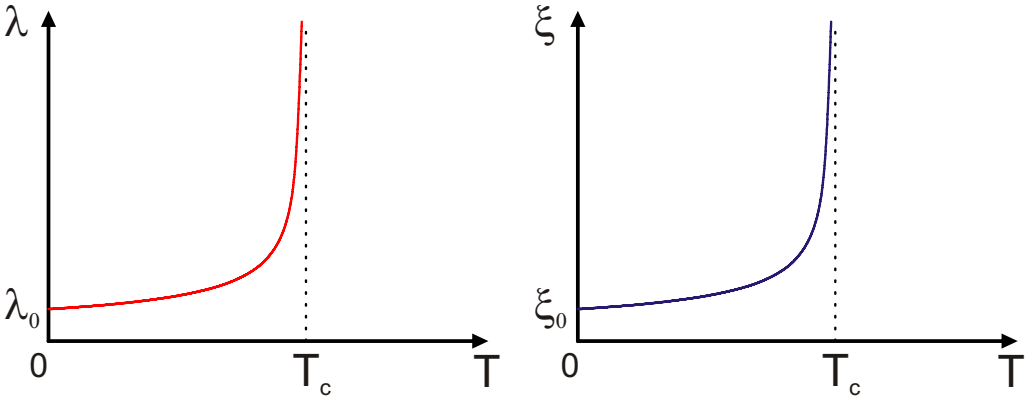

Figure 2.6: Temperature dependence of the superconducting penetration depth and coherence length.

the GL equations have proved very useful to explain the behaviour of superconductors and are especially good at predicting behaviour near phase transitions such as at the critical field.

2.5 Fluxoid Quantisation

As already mentioned, the superconducting order parameter is represented by $\psi = |\psi| e^{i\phi}$. Current carrying states are connected to gradients in the phase, ϕ, of the wavefunction. For instance $\psi = |\psi| e^{i(\mathbf{p}.\mathbf{r})/\hbar}$ is a current carrying state, where $\mathbf{p}$ is the momentum of the supercurrent charge carrier. This can be incorporated into the second GL equation (2.21) for zero applied field ($\mathbf{A} = 0$) to give a supercurrent density of

$$\mathbf{J_s} = \frac{e^*\mathbf{p}}{m^*}|\psi|^2 = \frac{e^* {n_s}^* \mathbf{p}}{m^*}. \tag{2.25}$$

Hence

$$\mathbf{p} = \frac{m^*\mathbf{J_s}}{e^* {n_s}^*}. \tag{2.26}$$

Consider now the situation highlighted in figure 2.7 where a total flux, Φ, permeates a normal 'hole' surrounded by a uniform superconducting region. If currents are flowing around the hole then there will be a phase difference between two points (labelled X and Y in figure 2.7) of an arbitrary path drawn around the hole given by

$$(\Delta\phi)_{XY} = \int_X^Y \frac{\mathbf{p}}{\hbar} d\boldsymbol{l}, \tag{2.27}$$

where $d\boldsymbol{l}$ is an element of the line joining points X and Y. As mentioned in section

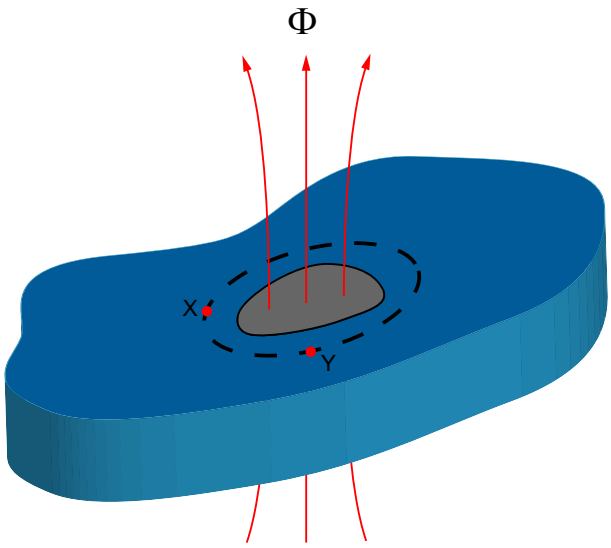

Figure 2.7: Flux flow through a normal region surrounded by a superconducting area.

2.4 the momentum in an applied magnetic field is replaced with a canonical momentum that includes the momentum contribution from the field, hence $\mathbf{p} \rightarrow \mathbf{p} + e^*\mathbf{A}$. This combined with equation 2.26 and equation 2.27 leads to

$$(\Delta\phi)_{XY} = \frac{m^*}{\hbar {n_s}^* e^*} \int_X^Y \mathbf{J}.d\mathbf{l} + \frac{e^*}{\hbar} \int_X^Y \mathbf{A}.d\mathbf{l}. \tag{2.28}$$

By inspection it is apparent that there are two components to the overall phase change; a phase difference due to the current flow, and a phase difference due to the enclosed flux.

It follows that the phase change after going around the whole loop is

$$\Delta\phi = \frac{m^*}{\hbar {n_s}^* e^*} \oint \mathbf{J}.d\mathbf{l} + \frac{e^*}{\hbar} \oint \mathbf{A}.d\mathbf{l}. \tag{2.29}$$

Using the identity from Stokes' theorem $\oint \mathbf{A}.d\mathbf{l} = \iint_s \nabla \times \mathbf{A}.ds$ and remembering that $\mathbf{B} = \nabla \times \mathbf{A}$ this then becomes

$$\Delta\phi = \frac{m^*}{\hbar {n_s}^* e^*} \oint \mathbf{J}.d\mathbf{l} + \frac{e^*}{\hbar} \iint_s .\mathbf{B}.ds \tag{2.30}$$

However, the wavefunction is by definition single valued, therefore the total phase change after going around a complete loop must be $n \times 2\pi$. Also notice that

$\iint_s \mathbf{B}.ds$ is the total flux within the hole, i.e. Φ, therefore

$$\Phi = \frac{nh}{e^*} - \frac{m^*}{{n_s}^* {e^*}^2} \oint \mathbf{J_s}.d\mathbf{l}. \tag{2.31}$$

The screening currents that encircle a normal hole rapidly decay to zero and so it is reasonable to assume that $\mathbf{J_s} = 0$ for a loop drawn sufficiently far from hole, hence

$$\Phi = \frac{nh}{e^*} = n\Phi_0. \tag{2.32}$$

Here the value $\frac{h}{e^*} = \frac{h}{2e}$ is clearly the smallest non-zero value for Φ, hence it is defined as the superconducting flux quantum, Φ_0. This result allows two important conclusions to be drawn, firstly any flux that is surrounded by a superconducting region is quantised and secondly that the minimum amount of flux in such a region is a single flux quantum, Φ_0.

2.6 Type II Superconductors and the Mixed State

The two length scales ξ and λ defined by the GL equations describe what happens at a normal/superconducting (N/S) interface. Each lengthscale is directly correlated to an opposing energy contribution to the system and as such the ratio of the two, κ, can provide a large amount of information. For typical pure superconductors, $\kappa << 1$ i.e. ξ is much greater than λ. In 1957 Abrikosov [21] considered the consequences of $\kappa > 1$ i.e. $\xi < \lambda$. He did this by examining the boundary between normal and superconducting regions of a material, an illustration of which is given in figure 2.8.

The simplest way to analyse this boundary, using an approach similar to that of [22], is to consider the impact on the overall free energy of the system due to the different lengthscales. ξ describes the length over which n_s increases to its bulk value. If the interface has an area A this rise in n_s will increase the free energy of the interface by roughly

$$(f_n - f_s)A\xi. \tag{2.33}$$

λ describes the magnetic penetration depth and so when the critical magnetic field, H_c, is applied the change in free energy due to the exclusion of magnetic

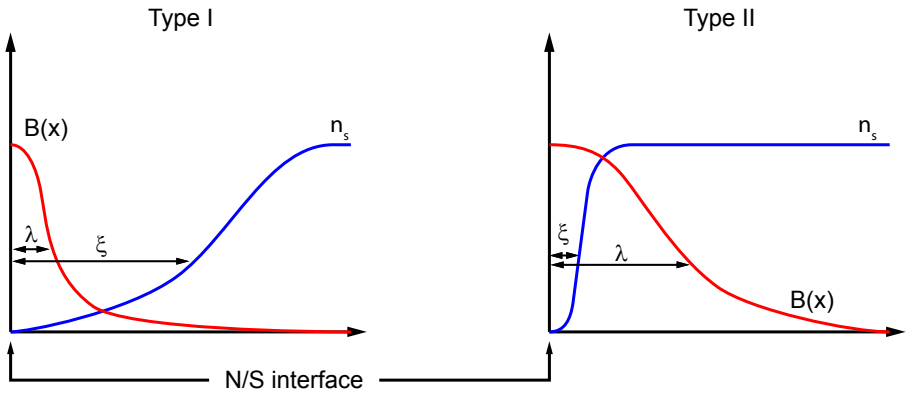

Figure 2.8: Illustration of the decay in magnetic field and recovery of superconductivity over the respective lengthscales at a normal/superconducting interface, for a type I and type II superconductor.

field at the interface will be about

$$-\frac{1}{2}\mu_0 {H_c}^2 A\lambda. \tag{2.34}$$

Hence because of these two length scales it can be said that the net interface energy per unit area, σ is

$$\sigma \approx \frac{1}{A}((f_n - f_s)A\xi - \frac{1}{2}\mu_0 {H_c}^2 A\lambda), \tag{2.35}$$

and remembering that when a critical magnetic field is applied to a superconductor it will exactly cancel the free energy difference between f_s and f_n, equation 2.35 can be simplified to

$$\sigma \approx \frac{1}{2}\mu_0 {H_c}^2(\xi - \lambda). \tag{2.36}$$

It therefore follows that if $\xi > \lambda$ ($\kappa < 1$) then there is a positive surface energy, i.e. any N/S interface will act to increase the overall free energy of the system. If $\xi < \lambda$ ($\kappa > 1$) then there is a negative surface energy. The more thorough examination given by Abrikosov finds the result that the crossover is actually at $\kappa = \frac{1}{\sqrt{2}}$.

When the surface energy is positive, the lowest energy state is achieved by having as little S/N interface as possible, as is the case in type I superconductors in the Meissner state. However, when the surface energy is negative, the more S/N interface there is, the lower the energy state. Abrikosov called these superconductors type II superconductors.

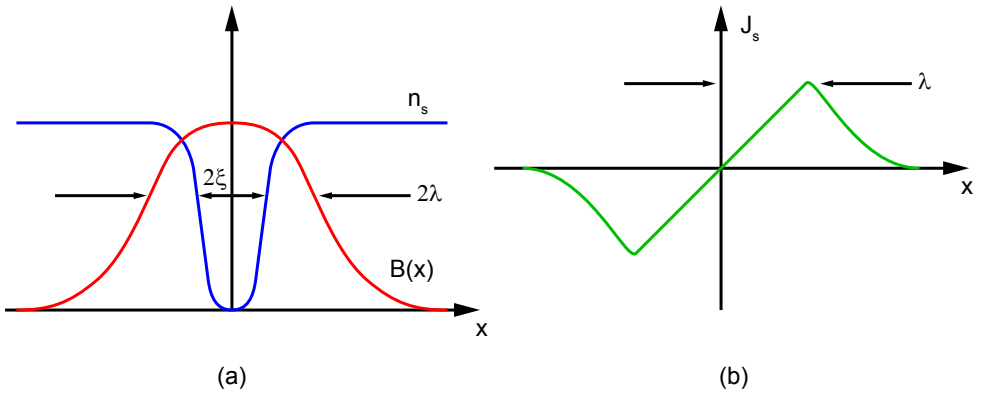

Figure 2.9: Cross-section through an isolated vortex illustrating its structure. (a) Magnetic field and superconducting charge carrier density with respect to distance from the centre of the vortex . (b) Supercurrents flow around the vortex so that at a point either side of the vortex they will be flowing in opposite directions.

Type II superconductors maximise the S/N interface by allowing flux to penetrate the superconductor so long as a certain minimum field, H_{c1}, is applied. This minimum field is necessary to overcome the surface screening currents and make the mixed state energetically favourable. The flux penetrates the superconductor in the form of cylindrical vortices of flux that have normal cores and are encircled by supercurrents. The lowest energy state is found when these vortices have as little flux as possible, however there is a minimum size such vortices can become. As described previously there is a lower limit to the amount of flux they can carry, which is exactly one flux quantum, Φ_0. Also, the shortest distance superconductivity can recover over is ξ meaning vortices will have a normal core with a diameter of 2ξ, while penetration of the magnetic field to a depth of λ means that supercurrents will encircle the core with a diameter of 2λ (figure 2.9).

The encircling supercurrents will cause vortices to interact with each other if they become close enough. Neighbouring vortices will have currents flowing in opposite directions at their closest point, as illustrated in figure 2.10, and hence will be repelled from each other. Abrikosov showed that these vortices form a periodic lattice as the repulsive force causes them to maximise their spacing, although he mistakenly thought that the lowest energy state was for a square lattice. It was later shown by Kleiner *et al.* [24] that the lowest energy state is found with a triangular lattice (figure 2.10). It should be noted that the difference in energy of these two lattices is very small and it is possible for the underlying crystal structure to have an affect on the vortex lattice and cause a square lattice to form.

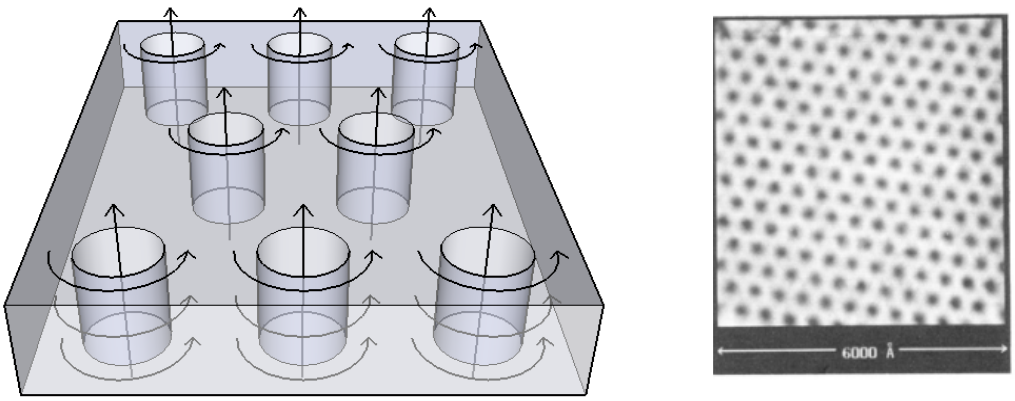

Figure 2.10: Triangular vortex lattice. (a) Sketch showing Abrikosov lattice, each vortex has a line of flux flowing through it with encircling supercurrents that cause the vortices to repel each other. (b) Scanning-Tunnelling-Microscope image of the Abrikosov lattice in superconducting $NbSe_2$, reproduced from [23].

Abrikosov also showed that the lattice spacing is dependent on the magnetic field so that as the field is increased, the vortices move closer together until at an upper critical field, H_{c2}, their cores begin to overlap and the superconductor is driven normal. However, because of the partial flux penetration, the diamagnetic energy cost of holding the field out is less, so H_{c2} can be much greater than the thermodynamic critical field H_c.

Because of flux penetration in type II superconductors, the magnetic phase diagram and magnetisation curve (figure 2.11) differs from a that of a type I superconductor (figure 2.3) between H_{c1} and H_{c2}.

It is important at this point to mention the special case of thin films where their thickness is $t < \lambda$. As shown by Pearl [25] in such cases the consequence of a 2D geometry on Maxwell's equations must be considered. This alters the effect of the screening currents, resulting in an effective penetration depth of

$$\Lambda = \frac{\lambda^2}{t}. \tag{2.37}$$

Clearly the 2D geometry greatly increases the effective penetration depth, but another effect of this is to alter the rate of spacial decay of the supercurrents. In

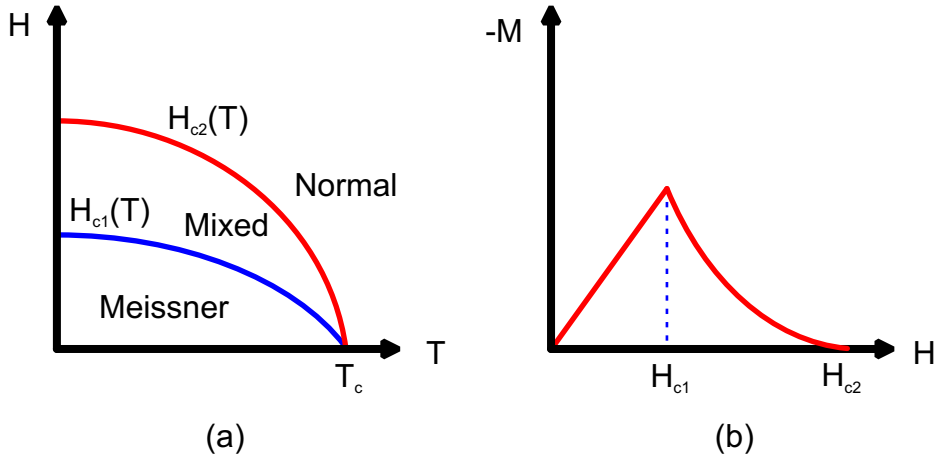

Figure 2.11: a) Magnetic phase diagram for a type II superconductor showing the temperature dependence of the two critical fields. (b) Magnetisation curve for a type II superconductor showing the Meissner state below H_{c1} and the mixed state between H_{c1} and H_{c2}.

a bulk superconductor the current decays as $exp(-r/\lambda)$ but in a thin film this changes to $1/r^2$ meaning that vortices will interact over a much longer range. This result is not only important for typical type II superconductors, but also for superconductors that are type I in bulk as rather than use the bulk value of the GL parameter the effective value, κ^*, must be used instead given by

$$\kappa^* = \frac{\Lambda}{\xi}. \tag{2.38}$$

The value of κ^* that differentiates between type I and type II behaviour is the same as for κ and so a type I superconductor will become type II if it is thin enough.

2.7 Demagnetising Fields and the Intermediate State

Despite having a positive surface energy, there are instances where it is possible for stable N/S interfaces to form inside type I superconductors in a departure from the Meissner state. This is due to the demagnetising effect which is related to a sample's geometry. The easiest way to visualise this effect is to consider a superconductor in the Meissner state as in figure 2.12(a). Field lines are bunched up around the equator and separated at the poles, hence at the equator the field at the surface of the superconductor is larger than the applied field, and at the poles it is less. This means that when the applied field increases to a level determined

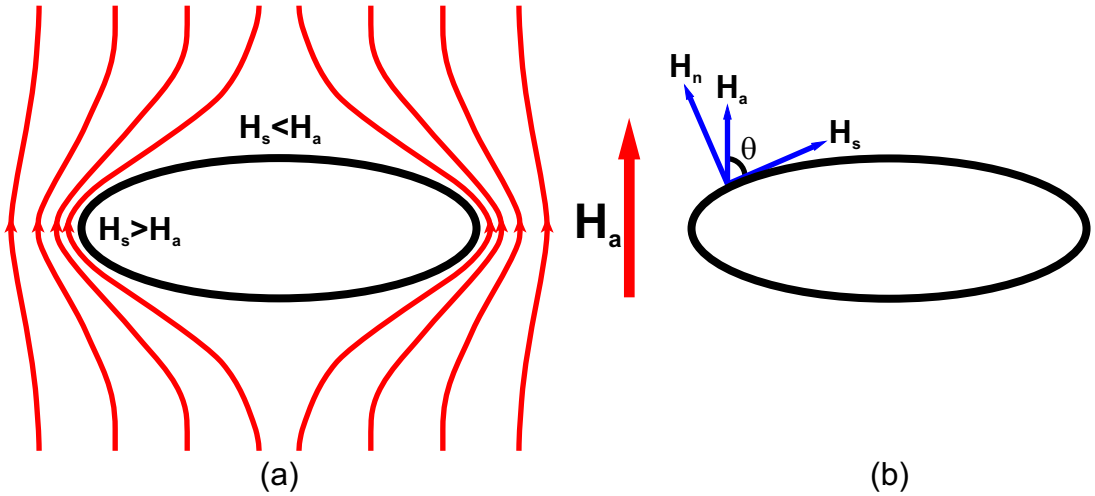

Figure 2.12: Superconducting ellipsoid in an applied field $\mathbf{H_a}$. (a) Sketch illustrating effect of Meissner state on field lines and hence the field at the surface. (b) Sketch illustrating direction of field components at the surface where $\mathbf{H_n}$ is the component normal to the surface and $\mathbf{H_s}$ is the component parallel to the surface.

by the shape of the superconductor, the field at the surface can reach the critical field before the applied field reaches this critical value, making some parts of the superconductor turn normal whilst other parts remain superconducting.

A more thorough analysis is as follows: when a magnetic field $\mathbf{H_a}$ is applied to a superconductor an additional field is induced known as the demagnetising field. This is true for all materials but the effect is particularly pronounced for superconductors due to their perfect diamagnetism, where $\chi = -1$ (values of $\chi \approx 10^{-4}$ are typical for normal metals). The internal magnetising field, $\mathbf{H_i}$, of a sample is therefore related to the applied field and the sample's demagnetising field, $\mathbf{H_D}$, and in the case of a homogeneous internal field the following applies

$$\mathbf{H_i} = \mathbf{H_a} - \mathbf{H_D} = \mathbf{H_a} - \eta\mathbf{M}. \tag{2.39}$$

where η is the demagnetising factor, which is determined by the shape of the sample and the applied field direction and ranges from zero to one.

In order to ensure a homogeneous internal field the case of an ellipsoid is considered with a magnetic field applied along one of its principal axes. The flux density $\mathbf{B}$ is defined as

$$\mathbf{B} = \mu_0(\mathbf{H_i} + \mathbf{M}), \tag{2.40}$$

which combined with equation 2.39 gives

$$\frac{\eta \mathbf{B}}{\mu_0} + (1-\eta)\mathbf{H_i} = \mathbf{H_a}. \tag{2.41}$$

However, for a superconductor in the Meissner state $\mathbf{B} = 0$ so

$$\mathbf{H_i} = \frac{\mathbf{H_a}}{(1-\eta)}. \tag{2.42}$$

The fields of both the internal and external surfaces are tangential and continuous, hence equation 2.42 can be adapted to give the field at the surface, $\mathbf{H_s}$. By also noting that the normal component of $\mathbf{B}$, B_n, is zero at the surface the following is true

$$\mathbf{H_s} = \frac{H_a sin\theta}{(1-\eta)}\hat{\mathbf{t}}, \tag{2.43}$$

where θ is the angle between the applied field and the tangent to the surface as illustrated in figure 2.12(b), and $\hat{\mathbf{t}}$ is the unit vector tangential to the surface. It is now apparent that the field will be zero at the poles and a maximum at the equator. This maximum value will be greater than $\mathbf{H_a}$ by an amount dependent on η. η is well defined only for ellipsoids, see for example [26], but important results are found by extending the dimensions of an ellipsoid to certain limiting cases. For instance, as illustrated in figure 2.13(a), η is zero for a long thin cylinder or plate in a parallel field (i), $\frac{1}{3}$ for a sphere (ii), $\frac{1}{2}$ for a long cylinder in a perpendicular field (iii) and 1 for an infinite flat slab in a perpendicular field (iv). For other 3D shapes ν can be approximated to a reasonable degree as being equal to the demagnetising factor for the largest inscribed ellipsoid, as suggested by Torre [27].

The consequence of this for superconductors is that when the external field reaches the value $H_a = (1-\eta)H_c$, the field at the equator will equal the critical field and drive the edge region normal. Clearly the whole superconductor will not turn normal as the field will then be equal to H_a everywhere which is less than H_c. Similarly it is not stable for a normal region to form around the edge because as the field penetrates the superconductor, the local field decreases taking it below the critical field. Instead field penetrates the superconductor and forms a series of normal and superconducting regions, limiting the maximum local fields to H_c. In type II superconductors these take the form of microscopic vortices in the mixed state as discussed previously. In type I superconductors the surface energy of the interface between normal and superconducting regions

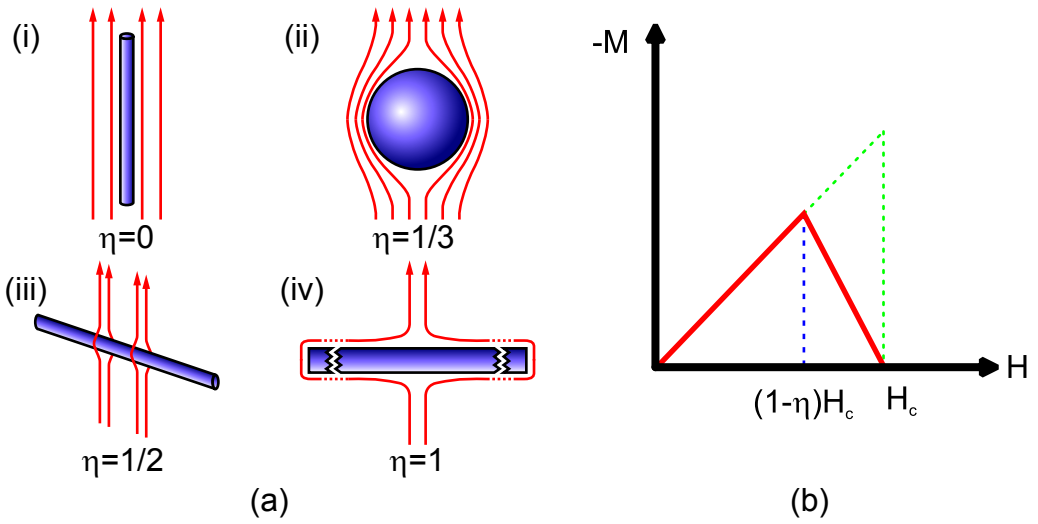

Figure 2.13: (a) Demagnetising factor for various shapes made by extending an ellipsoid along the relevant axes. (b) Magnetisation curve for a type I superconductor with demagnetising factor η. When the applied field is above $(1-\eta)H_c$ the superconductor is in the intermediate state. The green dotted lines represent the Meissner response for a demagnetising factor of zero.

allows macroscopic domains to form while forcing the interface to minimise its area. This is known as the intermediate state and causes the magnetisation curve to be modified as shown in figure 2.13(b).

Landau [2] considered the case of an infinite flat slab in a perpendicular field. As already noted, this has a value of 1 for η meaning it will be in the intermediate state for all non zero applied fields. In this case the domains are arranged perpendicular to the surface of the slab in order to minimise their area through the slab as shown in figure 2.14. The period of these lamina, d, has two components; a width for the normal region, d_n, and a width for the superconducting region, d_s, where $d = d_n + d_s$. The field in the superconducting regions is zero and in the normal regions is $H_n(T)$ (which in most instances is equal to $H_c(T)$ but can be lower as will be shown later). Therefore the total flux applied, Φ_a, to a single lamina period of length L will be

$$\begin{aligned} \Phi_a &= H_a L d = H_n L d_n. \\ \therefore d_n &= \frac{\Phi_a}{H_n L} = \frac{H_a}{H_n} d. \end{aligned} \tag{2.44}$$

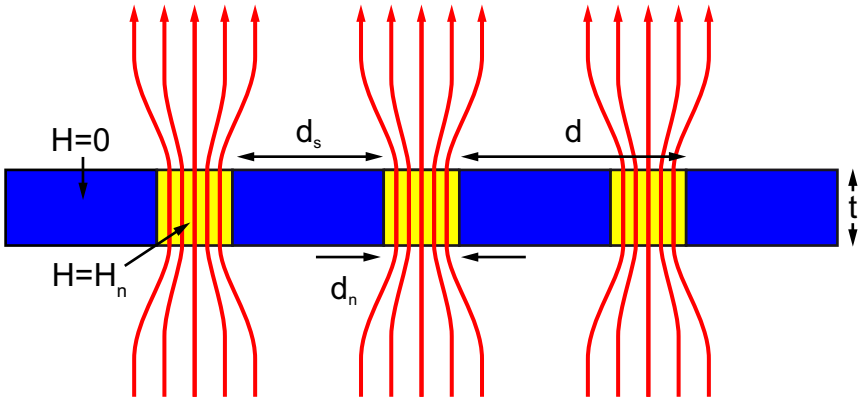

Figure 2.14: A type I superconducting flat slab in the intermediate state. The width of each superconducting and normal section, d_s and d_n, is dependent on the applied field and temperature. The overall period, d, also depends on the material and thickness, t, of the slab.

and from the earlier definition of d

$$\begin{aligned} \frac{H_a}{H_n} d + d_s &= d. \\ \therefore d_s &= \left(1 - \frac{H_a}{H_n}\right) d. \end{aligned} \tag{2.45}$$

Hence the widths d_n and d_s vary with applied field and temperature, but similar to vortices in type II superconductors the minimum width will be 2ξ and the flux through any normal region surrounded by a superconducting area still has to be quantised.

The top down arrangement of the domains can be far more complicated than this simple periodic structure suggests, and for a flat slab in a perpendicular field the conventional view is of twisting laminar structures although it has been shown experimentally [28] that it is possible to straighten out laminar structures by applying a field tilted in the direction of the lamina. However, energy differences between different domain configurations are small and depend largely on sample properties allowing not only laminar structures to form, but also tubular domains and bubbles. Prozorov has recently shown [1] that it is possible to find both laminar structures and bubbles in the same sample at the same applied field depending on whether flux was entering or leaving the sample. Figure 2.15 is taken from this work and is included to illustrate the appearance of these two phases. Laminar domains are probably most commonly found and easiest to analyse and many of the same physical considerations apply to all intermediate state so it is worth exploring this further.

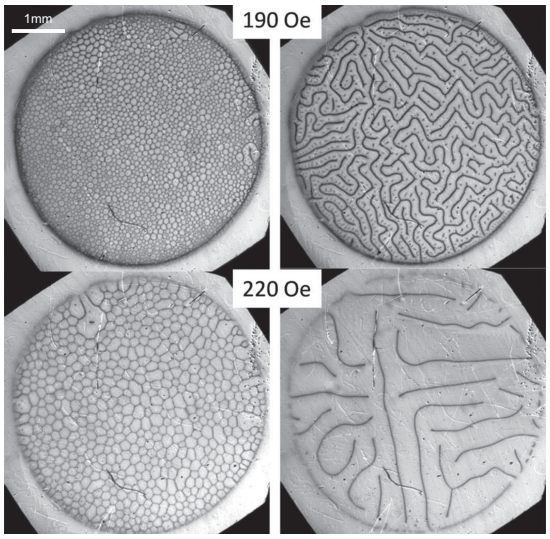

Figure 2.15: Examples of laminar and bubble domains from [1]. In this case bubbles form as flux penetrates the sample (increasing field, shown on the left) and lamina form as flux leaves the sample (decreasing field, shown on the right).

To determine the size of the period of the laminar structure consideration must be made of different energy contributions to the system so that they can be minimised. This can be done by following a similar approach to that used by both Huebener [29] and also de Gennes [30]. The first energy contribution considered, F_1, is the interface energy of the N/S domain walls, the principle behind which has already been covered in equation 2.36. For a superconducting slab with thickness t and a laminar structure with period d, equation 2.36 can be modified to give the increase in energy per unit area of the slab due to the N/S interface,

$$F_1 = \frac{1}{2}\mu_0 {H_c}^2 \delta \frac{2t}{d}. \tag{2.46}$$

Here $\delta = \xi - \lambda$ and is sometimes referred to as the wall energy term, and $2t/d$ is the total area of the domain walls per unit area of the slab. As previously discussed this energy term is positive for type I superconductors and favours a minimisation of the N/S surface area and hence a large period laminar structure.

The second energy contribution, F_2, arises due to the energy difference between the non-uniform magnetic field distribution outside the superconductor and a uniform magnetic field that would exist if the superconductor became normal or if flux was allowed to penetrate such that the domain period was infinitely thin. This energy contribution is therefore reduced with the size of the laminar period and so in this regard acts in the opposite direction to F_1. The non-uniform field

outside the superconductor is perhaps best imagined as a bending of field lines and can be seen in figure 2.14. Here the field in the normal region is H_n and the distance over which the non-uniform field extends is related to the period, d, hence the excess energy density caused by this is of the form

$$F_2 = \frac{1}{2}\mu_0 {H_n}^2 .2d.f(\tilde{h}), \tag{2.47}$$

where $f(\tilde{h})$ is a function of the reduced field $\tilde{h} = H_a/H_c$. While numerical calculations for $f(\tilde{h})$ have been given by Landau and Lifshitz [31], Tinkham [19] has managed to achieve a similar result using a simple physical argument that considers the difference in energy densities between a uniform and non-uniform field at the surface of the superconductor and multiplies this by the distance over which the non-uniform field returns to a uniform one. This argument is re-created here as understanding it provides insight into the nature of this energy contribution.

The energy density of the field in the normal regions is $\frac{1}{2}\mu_0 {H_n}^2$ so the average energy density of the field at the surface of the superconductor can be found by multiplying this by the fraction of the superconductor that is in the normal state, $\rho_n = d_n/d$, as there is zero field at the surface of the superconducting regions:

$$\frac{1}{2}\mu_0 \rho_n {H_n}^2. \tag{2.48}$$

The energy density of a uniform field is $\frac{1}{2}\mu_0 {H_a}^2$ so substituting in equation 2.44 this becomes

$$\frac{1}{2}\mu_0 {\rho_n}^2 {H_n}^2, \tag{2.49}$$

and so the excess energy density at the surface of the superconductor due to the laminar structure is

$$\frac{1}{2}\mu_0(\rho_n - {\rho_n}^2){H_n}^2 = \frac{1}{2}\mu_0 \rho_n \rho_s {H_n}^2, \tag{2.50}$$

where $\rho_s = d_s/d = 1 - \rho_n$ is the fraction of the superconductor in the superconducting state. F_2 will then depend on the length over which the non-uniform magnetic field relaxes either side of the slab. Tinkham approximated this length to be $d\rho_s\rho_n$ making F_2

$$F_2 = \mu_0 {\rho_n}^2 {\rho_s}^2 d{H_n}^2. \tag{2.51}$$

The overall energy difference due to the laminar intermediate state, $(F_1 + F_2)$,

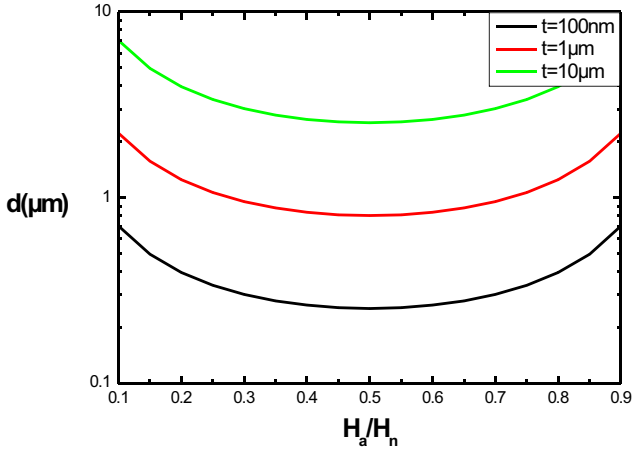

Figure 2.16: Dependence of laminar period, d, on applied field from equation 2.53 for three slab thicknesses of Pb ($\delta \approx 40nm$).

can now be minimised to determine the optimal value of d to be

$$d = \frac{(t\delta)^{1/2} H_c}{\rho_n \rho_s H_n} \approx \frac{(t\delta)^{1/2}}{\rho_n \rho_s}, \tag{2.52}$$

which from previous definitions of ρ_n and ρ_s becomes

$$d \approx \frac{(t\delta)^{1/2}}{\frac{H_a}{H_n} - (\frac{H_a}{H_n})^2}. \tag{2.53}$$

To see how this affects a type I superconductor, the predicted behaviour from this equation is shown in figure 2.16 for a Pb slab, where $\delta \approx 40nm$. As is clear from equation 2.53 the laminar period increases with the thickness of the slab, but it is interesting to note that at $t \approx 1\mu m$, $d \approx t$. For much thicker slabs d is generally much less than t, and for much thinner slabs d is much larger than t. This has important implications for the behaviour of mesoscopic samples. Thin samples with mesoscopic widths (i.e. several coherence lengths, which for Pb is around $1\mu m$), will be much smaller than the laminar domain and it is only when the sample is thicker that it will have a comparable size to the domain. Hence in order to study the intermediate state in mesoscopic samples it is necessary to investigate truly 3D samples.

As shown above, when there is a non-zero demagnetising factor account must be made of the additional surface energies involved and this is also true when considering the critical field at which superconductivity is destroyed. As has already been noted, these surface energies increase the overall energy of the system for a

type I superconductor in the intermediate state and so it is not surprising that this effect can decrease the critical field of a superconductor that enters the intermediate state, H_{cI}. These additional energies will also have an impact on the value of H_n. In order to determine the size of this effect with regard to the critical field it is necessary to minimise the free energy of the entire system. In terms of the Helmholtz free energy for a sample with volume V and a zero demagnetising factor the following applies

$$\begin{aligned} F_n &= V f_n + \tfrac{1}{2}\mu_0 V {H_a}^2. \\ F_s &= V f_s, \end{aligned} \tag{2.54}$$

where F_n and F_s are the total free energies of the normal and superconducting states respectively, and f_n and f_s are the free energy densities for the normal and superconducting states. It is useful to discuss this in terms of the energy per unit volume, so for a flat slab in the intermediate state the energy contributions F_1 and F_2 need to be added, but the values for these given earlier were per unit area so they need to be divided by the thickness of the slab. F_n and F_s also need to be adjusted so that they relate to the fraction of the slab that is normal or superconducting. Finally, using the definition of the thermodynamic critical field, $f_n - f_s = \frac{1}{2}\mu_0 {H_c}^2$, the total free energy per unit volume can be written as

$$f_I = \rho_s f_s + \rho_n(f_s + \tfrac{1}{2}\mu_0 {H_c}^2 + \tfrac{1}{2}\mu_0 {H_n}^2) + \frac{F_1 + F_2}{t}. \tag{2.55}$$

Using the earlier definitions of ρ_n and ρ_s, and by substituting the optimal laminar period form 2.53 into terms for F_1 and F_2 this becomes

$$f_I = f_s + \tfrac{1}{2}\mu_0 \rho_n {H_c}^2 + \tfrac{1}{2}\mu_0 \frac{{H_a}^2}{\rho_n} + 4(1-\rho_n)\left(\frac{\delta}{t}\right)^{\frac{1}{2}} \tfrac{1}{2}\mu_0 H_c H_a. \tag{2.56}$$

It can now be seen that the surface energy terms are proportional to $\left(\frac{\delta}{t}\right)^{\frac{1}{2}}$, hence if the thickness of the superconductor is large compared to the wall-energy term, δ, then these additional energy terms become negligible and when the energy is minimised it is found that $H_n = H_c$. Otherwise when f_I is minimised with respect to ρ_n it is found that

$$H_n = H_c \left[1 - 4\left(\frac{\delta}{t}\right)^{\frac{1}{2}} \left(\frac{H_a}{H_c}\right)\right]^{\frac{1}{2}}. \tag{2.57}$$

Here it can be seen that $H_n = H_c$ at zero applied field, but decreases as the applied field increases. H_{cI} can now be defined as the point when $H_a = H_{cI}$ so that $\rho_n = 1$ and remembering that $\rho_n = \frac{H_a}{H_n}$ the resulting quadratic equation can be solved to give

$$H_{cI} = H_c \left[\left(1 + \frac{4\delta}{t} \right)^{\frac{1}{2}} - 2 \left(\frac{\delta}{t} \right)^{\frac{1}{2}} \right]. \tag{2.58}$$

As this result is modelled on an idealised sample with a highly ordered laminar structure, in the literature a simpler result of $H_{cI}/H_c \approx \left[1 - \delta/t)^{1/2}\right]$ (e.g. [32]) or $H_{cI}/H_c \approx \left[1 - C\delta/t)^{1/2}\right]$ (where C is a constant between 0.8 and 2, e.g. [33]) is often used.

This result gives the impression that H_{cI} will eventually approach zero for a sufficiently thin superconductor, however the earlier result given at the end of section 2.6 for thin films means this will not be the case as for sufficiently thin films the behaviour will switch from type I to type II. This means that rather than the point at which superconductivity is destroyed being H_{cI}, it will instead be H_{c2}. Not only this but the value of H_{c2} will increase as the thickness of the film decreases due to the increase in κ^* which, as will be shown in the next section, is proportional to H_{c2}. Therefore the general behaviour expected with decreasing thickness is for the upper critical field of a type I superconducting slab in a perpendicular film to decrease as $\approx t^{1/2}$ until a certain thickness, then to increase as $\approx 1/t$. Such behaviour has been observed by Cody and Miller [33], whose results for Pb are shown in figure 2.17, with the lowest critical field being $\sim 25\%$ below H_c when the slab is $\sim 1\mu m$ thick. More recent results using muon spin resonance have not only confirmed the decrease in H_{cI} with thickness but also the predicted dependence of H_n within the normal domains on the applied field [34].

2.8 Supercooling and H_{c2}

H_{c2} has been mentioned previously as the upper critical field of type II superconductors, but it also plays a role in type I superconductors when considering the point at which superconductivity nucleates in a decreasing field. This can be best illustrated by determining what the value of H_{c2} is. An important step in doing this is to consider how $|\psi|^2$ behaves near H_{c2}.

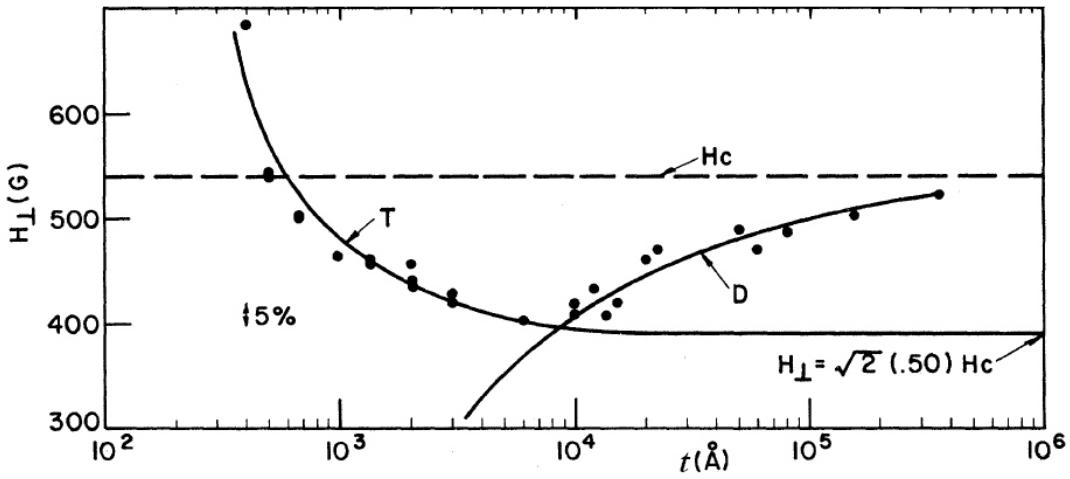

Figure 2.17: Critical perpendicular field dependence for Pb slabs on their thickness at 4.2K, from [33]. Dots represent experimental data, the line labelled T is a best fit with a 1/t dependence and the line labelled D is from the simplified form of equation 2.58. The dashed line is the bulk critical field.

In a bulk type II superconductor as the field is increased to H_{c2}, $|\psi|^2$ decreases continuously from ${\psi_\infty}^2$ to zero as vortices come closer together and start to overlap. From equation 2.16, ${\psi_\infty}^2 = -\frac{\alpha}{\beta}$, hence for fields near H_{c2}, where $|\psi|^2$ is much lower than ${\psi_\infty}^2$, $\alpha >> |\psi|^2 \beta$. This allows the GL equation given in 2.20 to lose the $\beta |\psi|^2 \psi$ term for fields near H_{c2}, leaving

$$\frac{1}{2m^*}(-i\hbar\nabla - e^*\mathbf{A})^2\psi = -\alpha\psi. \tag{2.59}$$

This is sometimes referred to as the linearised GL equation. Effectively this is the Schrödinger equation for a particle of mass m^* and charge $-e^*$ in a field $\mathbf{H} = \nabla \times \mathbf{A}$ with $-\alpha$ as the energy eigenvalue. This is a quantum mechanical problem that is well understood and for an infinite sample in a magnetic field applied along the z-axis the resulting energy eigenvalues are

$$E_{n,v_z} = \left(n + \tfrac{1}{2}\right)\hbar\omega_c + \frac{1}{2m^*}m^*{v_z}^2 = -\alpha. \tag{2.60}$$

Here v_z is the particle velocity in the z-axis, i.e. parallel to the field, and $\hbar\omega_c$ is the cyclotron energy, equal to $\hbar(e^*H/m^*)$. Hence the above can be rearranged to find H:

$$H = \left(-\alpha - \frac{{v_z}^2}{2}\right)\frac{m^*}{(n+\frac{1}{2})\hbar e^*}. \tag{2.61}$$

Remembering that $-\alpha$ is positive, clearly the highest field is obtained for $n = v_z = 0$, and is defined as H_{c2}. It is useful to determine H_{c2} in relation to H_c but

in order to do this H_c must first be found in terms of α. This can be done by combining equations 2.2, 2.14 and 2.16 to get

$$\frac{\alpha^2}{2\beta} = \frac{\mu_0}{2} {H_c}^2. \tag{2.62}$$

Equations 2.61 and 2.62 can now be combined with the earlier expressions given for λ and ξ, and noting that $\kappa = \lambda/\xi$ this gives

$$H_{c2} = \kappa\sqrt{2}H_c. \tag{2.63}$$

Hence when $\kappa > \frac{1}{\sqrt{2}}$, then $H_{c2} > H_c$ and when $\kappa < \frac{1}{\sqrt{2}}$, then $H_{c2} < H_c$, highlighting again the split between type I and type II superconductors at $\kappa = 1/\sqrt{2}$.

The role of H_{c2} in type I superconductors now becomes apparent when considering the conditions necessary for the above calculations to apply, namely the need for $|\psi|^2 << {\psi_\infty}^2$. In a type II superconductor this condition is met at H_{c2} regardless of the direction in which the magnetic field is swept. For a bulk type I superconductor however, when the magnetic field is increased in the superconducting state $|\psi|^2 = {\psi_\infty}^2$, hence superconductivity is not destroyed at H_{c2}. It is only when the magnetic field is increased above H_c that the superconductor is driven normal and $|\psi|^2 = 0$. Now when the field is reduced the above considerations apply and superconductivity does not reassert itself at H_c but it can 'supercool' down to H_{c2}, at which point superconductivity will nucleate and the type I nature of the superconductor will cause a rapid jump of $|\psi|^2 \rightarrow {\psi_\infty}^2$ everywhere. Such hysteretic behaviour is illustrated in figure 2.18. This discontinuous jump is indicative of a first-order phase transition, unlike the second-order phase transition due to the continuous change of $|\psi|^2$ at H_{c2} in a type II superconductor. Like other first-order phase transitions this allows supercooling and also superheating, which will be explored later.

2.9 Surface superconductivity and H_{c3}

In practice H_{c2} represents the lowest field a bulk type I superconductor can be supercooled to, but is not necessarily the actual supercooling field. This is often limited by defects that allow superconductivity to nucleate at higher fields as can be seen in the work of Feder and McLachlan [35]. The surface of a superconductor also plays a large role in the determination of the supercooling

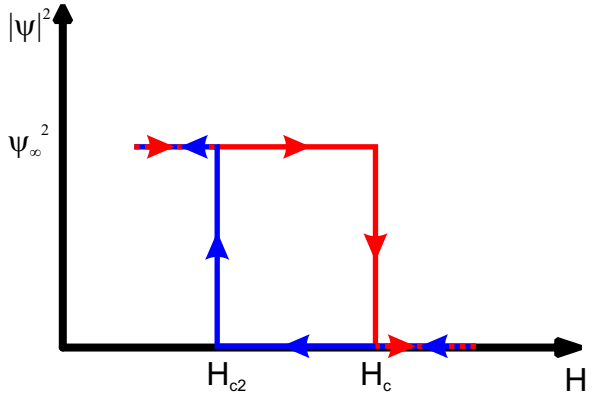

Figure 2.18: Hysteretic behaviour of the order parameter in a type I superconductor showing first-order phase transitions at the critical fields allowing supercooling of the normal state down to H_{c2}.

field and so far no account has been taken of this. Indeed for a superconductor to be supercooled down to H_{c2} the surface must be treated, for example coated in a normal conductor as was done in the work just cited, so as to remove these surface effects.

The effect of the surface of a superconductor in terms of the nucleation field was first investigated by Saint-James and de Gennes [36], who considered a semi-infinite sample that occupies the half-space $x > 0$, with $x < 0$ occupied by vacuum or an insulator. This was done in a way similar to the method used above to determine H_{c2}, although complicated by the need to consider boundary conditions imposed by the surface. For a field applied parallel to the surface Saint-James and de Gennes determined that the appropriate Schrödinger equation takes the form of a harmonic oscillator where the boundary conditions to be fulfilled become $d\psi/dx = 0$ at $x = 0$ and $x = \infty$. This has the minimum potential located at x_0 and for large values of x_0, i.e. far from the surface, the boundary conditions can be ignored and the solution will then take the usual form for a harmonic oscillator of

$$\psi = Aexp\left[-\tfrac{1}{2}\left(\frac{x - x_0}{\xi(T)}\right)^2\right]. \tag{2.64}$$

This solution also fulfils the boundary conditions at $x_0 = 0$ and in both cases the resulting energy eigenvalue gives a nucleation field equal to H_{c2}. This solution shows that the wavefunction extends to a region of about $\xi(T)$ around x_0, hence the nucleation of superconductivity will only be affected by the surface if it takes place within a depth of about ξ of the surface. In order to determine what this

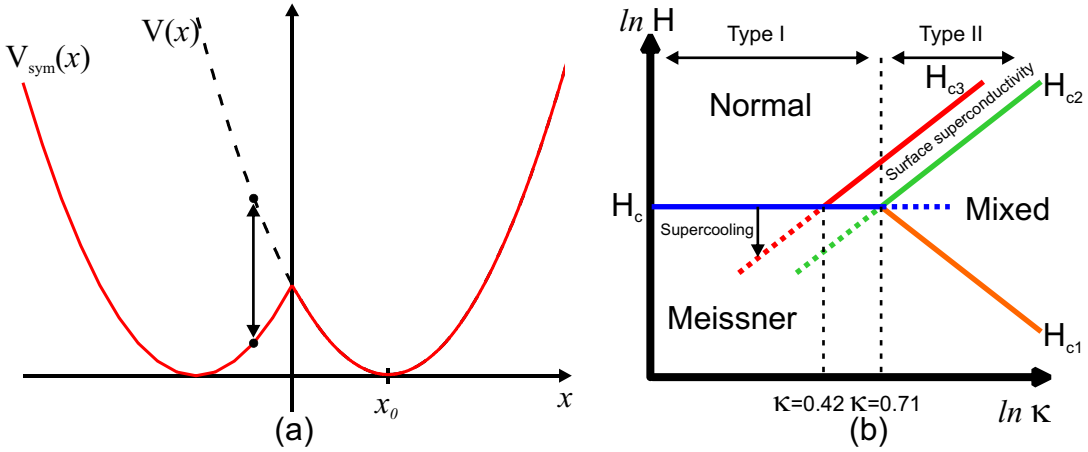

Figure 2.19: (a) Sketch illustrating the difference between the harmonic potential $V(x)$ and the symmetrised potential $V_{sym}(x)$ when $x_0 > 0$ showing that $V_{sym}(x) < V(x)$ hence the lowest energy state is lower for $V_{sym}(x)$. (b) Phase diagram highlighting how the separation of phases by various critical fields is related to the value of κ, after [37].

effect is, it is necessary to first consider how the potential, V(x), for intermediate values of x_0 can satisfy the boundary conditions. Saint-James and de Gennes did this by using the standard potential well for a harmonic oscillator that applies here when $x_0 = 0$ and $x_0 >> \xi(T)$ of $V(x) = (e^{*2}H^2/2m^*)(x - x_0)^2$ and making it symmetrical (let this new potential be labelled $V_{sym}(x)$) about $x = 0$ such that

$$\begin{aligned} V_{sym}(x) &= (e^{*2}H^2/2m^*)(x - x_0)^2, \quad (x > 0). \\ V_{sym}(x) &= V(-x), \qquad\qquad\qquad\quad (x < 0). \end{aligned} \tag{2.65}$$

As this is symmetrical about $x = 0$ it will automatically satisfy the boundary condition of $d\psi/dx = 0$ at $x = 0$. It should also be apparent that for $x_0 > 0$ the symmetrised potential is lower than $V(x)$ for all of the region $x < 0$, this is illustrated clearly in figure 2.19(a). As already stated, the eigenvalue related to $V(x)$ gives a nucleation field of H_{c2} hence if $V_{sym}(x)$ is lower than $V(x)$ then the associated eigenvalue will also be lower, making nucleation easier and therefore occurring at a higher field.

Saint-James and de Gennes used tabulated Weber functions to determine the exact value of the eigenvalue associated with the above symmetrised potential to be a factor of 0.59 lower than for the case with no surface boundaries hence the associated nucleation field, labelled H_{c3}, is

$$H_{c3} = 1.695 H_{c2} = 1.695 \left(\sqrt{2}\kappa H_c\right) \tag{2.66}$$

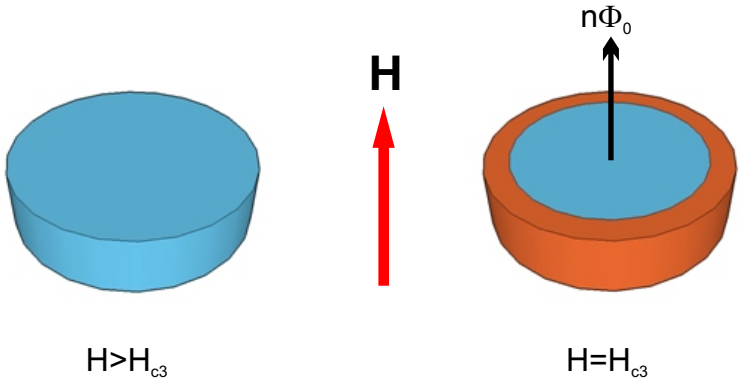

Figure 2.20: Formation of a giant vortex in a reducing field. When $\kappa > 1.695\sqrt{2}$ superconductivity nucleates first on the surface leaving a normal core, the flux though which is quantised hence when $n > 1$ this is referred to as a giant vortex.

The role of κ in dividing different behaviours can now be explained and is illustrated in figure 2.19(b). For values of κ where H_{c3} is less than H_c this effect will only be seen when the superconductor is supercooled, with superconductivity nucleating at the surface at H_{c3} before spreading to the rest of the superconductor. Hence supercooling tends to be limited by H_{c3}. For larger values of κ, where H_{c3} is greater than H_c, superconductivity is able to exist on the surface to a depth of $\approx \xi$ when it has been destroyed in the rest of the superconductor allowing the formation of the giant vortex state. This is when a superconducting ring on the surface encloses a normal core meaning the flux through the normal region will contain an integer number of flux quanta, the formation of such giant vortices is shown in figure 2.20. For large superconductors giant vortices will contain an enormous number of flux quanta (this can easily be in excess of 1×10^9 in a cm^2 sample) and so the idea that the flux is quantised loses meaning. It does however play a far more important role in flux structures of mesoscopic samples, where the giant vortex contains only a small number of flux quanta.

Saint-James and de Gennes also considered how the angle of the applied field affects the nucleation field, and found that when H is normal to the surface, the nucleation field becomes H_{c2} again. As the applied field is changed from normal to parallel, the nucleation field varies from H_{c2} to H_{c3} smoothly, although Saint-James and de Gennes did not specifically do this calculation. Hence for a sphere, or cylinder perpendicular to the applied field, superconductivity will nucleate in a band around the equator, before extending towards the poles as the applied field is reduced from H_{c3} to H_{c2} as shown in figure 2.21(a).

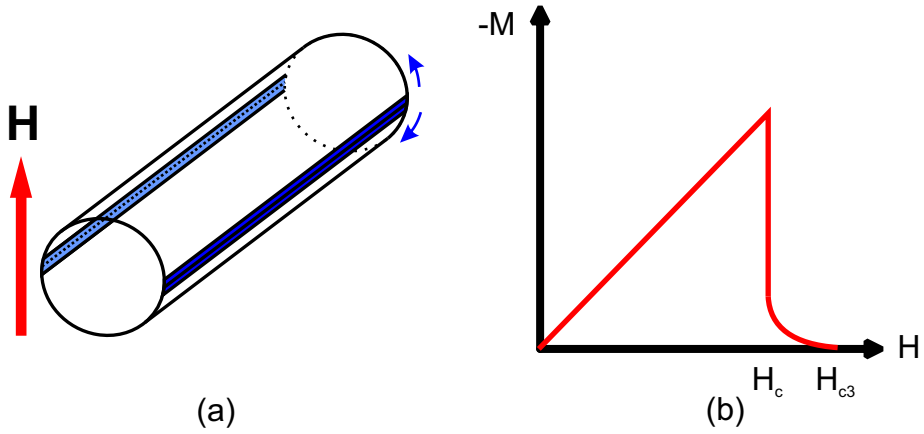

Figure 2.21: (a) Cylinder in a perpendicular field. In a reducing field superconductivity nucleates at H_{c3} at the equator and expands towards the poles (blue arrows) as the field is reduced further. (b) Magnetisation curve for a type I superconductor displaying surface superconductivity.

Surface superconductivity on a type I superconductor can be recognised in a magnetisation curve by an abrupt change in slope as the superconductor switches from the Meissner or intermediate state followed by a characteristic tailing off beyond the critical field as illustrated in figure 2.21(b). Whilst this may be a small effect for bulk samples, it is clearly going to have a much larger impact on mesoscopic sized samples where the superconducting sheath occupies a significant fraction of the sample. In fact it is reasonable to believe that for mesoscopic samples the value of H_{c3}, which is a surface effect, will be enhanced by a larger surface to volume ratio. It is now known that this is indeed the case and ultimately this is related to the increase in particle energy with increasing confinement, which is a well known phenomenon in quantum mechanics such as with the "particle in a box" problem (although the boundary conditions are very different in this case).

This effect was originally investigated, for example by Fink [38], by using the same method as in [36] but then introducing a second, parallel surface to form a slab of thickness d. For $d >> \xi$ the solution for H_{c3} is the same as before, as would be expected when the two surfaces are too far apart to interact. If the previous solution is now considered, where the minimum of the potential and hence the point at which superconductivity nucleates is $\approx \xi$ within the surface, then it should be apparent that at some critical thickness $\approx 2\xi$ the two potentials from each surface will overlap with the minimum being in the centre of the slab. Below this thickness the minimum, and hence the nucleation point, is always in the centre and so when superconductivity nucleates the entire sample

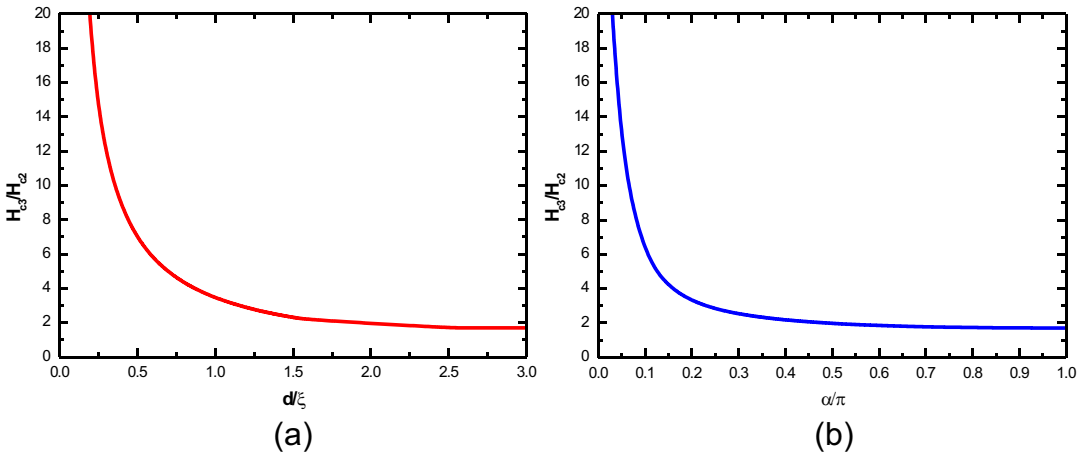

Figure 2.22: (a) Dependence of the nucleation field, H_{c3}, of a slab on its thickness, d, after [38]. (b) Dependence of the nucleation field of an infinite wedge as a function of the wedge angle, α, after [39].

becomes superconducting - there is no room for any vortices. Above this thickness superconductivity nucleates at the sides allowing vortices to form in the centre and for a range of thicknesses the two sides will interact/reinforce each other. Fink found that for $d/\xi \gtrsim 2.5$, H_{c3} is the same as for a single surface, that is $1.695H_{c2}$, and for $d/\xi \lesssim 1.6$ H_{c3} is greatly enhanced as $\mathrm{H_{c3}} \approx 2\sqrt{3}H_{c2}\frac{\xi}{d}$, which gives a value for H_{c3} of $2.17H_{c2}$ when $d/\xi = 1.6$. Between these two thicknesses there is a smooth transition in the value of H_{c3}, with the critical thickness above which a normal region is allowed being $d_c = 1.84\xi$. This dependence of H_{c3} on ξ is shown in figure 2.22(a).

The critical thickness can be altered by restricting the geometry of the sample further. For instance, Schweigert and Peeters [39] found that for a square sample normal regions could not exist alongside surface superconductivity when the side of the square was less than 2.33ξ. Furthermore they confirmed an earlier result [40] that surface superconductivity is further reinforced at the corners of the square. This is due to reinforcement of superconductivity in a wedge, which is essentially the same effect as the increase in surface superconductivity with increased confinement. Superconductivity in a wedge is a problem that has been tackled before, e.g. [41] and [42], and is approached using the same starting point as [36] but then transferring the equations and boundary conditions to cylindrical co-ordinates as this is more convenient for a wedge geometry. The wedges are then modelled as two long surfaces that meet at the origin.

By solving the GL equations numerically Schweigert and Peeters were able to do

more than just determine the angular dependence of the nucleation field, shown in figure 2.22(b), they could also determine the nucleation field for arbitrarily shaped samples. From this it can be seen that the enhancement of surface superconductivity at corners works in combination with the enhancement due to decreasing sample size. For example, for a large square superconductivity nucleates first at the corners at $H_{c3} \approx 1.96H_{c2}$, and will nucleate at ever increasing fields as the size of the square decreases. In triangles this is even more pronounced, e.g. $H_{c3} \approx 2.4H_{c2}$ for a large equilateral triangle, due to the sharper corners. Such increases in H_{c3} have been shown experimentally, for example by Dikin *et al* [43] in their work on superconducting mesoscopic curved stars. Clearly the effects of surface superconductivity will have a large impact on any superconducting mesoscopic sample with clean surfaces.

2.10 Superheating

As has already been stated, the superconducting-to-normal phase transition of a type I superconductor in the presence of a magnetic field is first-order and as such the observation of superheating is to be expected. This means that the magnetic field can be increased to a point such that the total energy of the superconductor is greater than that of the normal state and the transition to the normal state is delayed. Effectively there is a surface barrier opposing the entry of flux into the superconductor.

Superheating of the Meissner state is also possible in type II superconductors, delaying the onset of the mixed state beyond H_{c1}. It was in type II superconductors where the physical origin of the surface barrier was first discussed by Bean and Livingstone [44] for $\kappa >> 1$. Bean and Livingstone achieved this by considering the forces acting on the first vortex to enter a semi-infinite superconducting half-space when it is near the surface. At the surface of a superconductor there must be zero current normal to the surface. When a vortex within a superconductor is close to its surface this boundary condition greatly complicates the current distribution around the vortex. However, it is possible to regain the simpler model of an isolated vortex by placing an image anti-vortex the same distance outside the superconductor, as illustrated in figure 2.23. The vortex will then experience two competing forces. The first is due to Meissner screening currents that drives the vortex into the bulk of the superconductor and is dependent on the applied field. As already covered in section 2.6 the force on a vortex due a current density

J is $J\Phi_0$ so this first force is

$$F_1 = J(x)\Phi_0, \tag{2.67}$$

where J is (from [19])

$$\begin{aligned} J &= J_0 e^{-x/\lambda}. \\ J_0 &= \frac{H}{\mu_0 \lambda}. \end{aligned} \tag{2.68}$$

The second force is an attractive force towards the surface from the image vortex and is independent of the applied field.

$$F_2 = -J_i(2x)\Phi_0, \tag{2.69}$$

where $J_i(2x)$ is the current density due to the image vortex a distance $2x$ from it. For low values of x this is

$$J_i = \frac{e\hbar n_s}{2m.2x}. \tag{2.70}$$

For any non-zero applied field the repulsive force will dominate far from the surface, however for a vortex to enter the superconductor this force must be greater at the surface than the image force. The smallest distance these forces can be resolved over is the radius of the vortex ξ, hence there is a critical "barrier field" H_s that is reached when the magnitude of these two forces equal each other at a distance ξ within the surface of the superconductor. This can be simplified by noting that very near the surface $J(x) \approx J_0$, as is the case here for $\kappa >> 1$, hence when $F_1 = |F_2|$ then $J_0(H = H_s) = J_i(2\xi)$. Using the earlier definitions of λ and Φ_0 this gives

$$H_s = \frac{\Phi_0}{4\pi\lambda\xi}. \tag{2.71}$$

Relating this to H_c where $H_c = \Phi_0/2\pi\lambda\xi$ (again from [19]) then

$$H_s = \frac{H_c}{\sqrt{2}}. \tag{2.72}$$

This approach is often referred to as a "London approximation", as it assumes the London equation applies everywhere except for the core of the vortex with radius ξ. This is useful as treating a vortex as such a solid construct allows the simple calculations above to be used which in turn provide a good 'feel' for the physical origin of the barrier field. There are however a few drawbacks to this approach. One is that the choice of vortex radius is somewhat arbitrary and as can be seen from the above calculations the value of H_s is highly dependent on

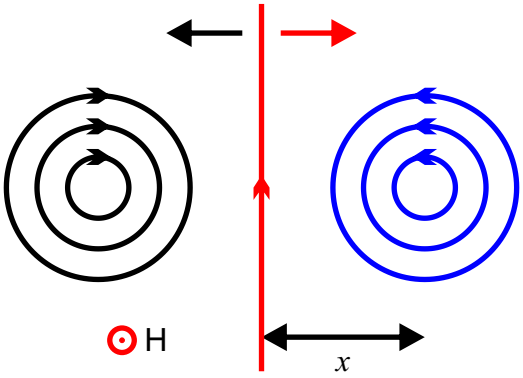

Figure 2.23: Sketch showing a vortex (blue) distance x inside a superconductor in an applied field H and the resulting repulsive force due to its interactions with the Meissner currents at the surface (red) and the attractive force from its image vortex (black) an equal distance outside the superconductor.

this. Another is that when the applied field is near H_s the order parameter $|\psi|$ (and hence n_s) is greatly reduced even before a vortex has nucleated.

This reduction in $|\psi|$ forms the basis of a more robust method of determining the value of the barrier field for $\kappa >> 1$ using the GL equations, first performed by de Gennes [45]. Because this considers the case of an increasing field there is a starting point of $\psi = \psi_\infty$ hence the linearised GL equations can not be used. The GL equations can be simplified in another way though since because $|\psi|$ is reduced before a vortex has nucleated, the GL equations need only be considered in one dimension (two dimensions are only needed after nucleation has taken place). By introducing a reduced order parameter $f = \psi/\psi_\infty$ and substituting into the original GL equations, then for a superconducting half-space in the region $x > 0$ with applied field along the z-axis, the one-dimensional GL equations are obtained [15]

$$\begin{aligned} \frac{1}{\kappa^2}\frac{\partial^2 f}{\partial x^2} &= f(-1 + f^2 + \mathbf{A}^2). \\ \frac{\partial^2 \mathbf{A}}{\partial x^2} &= f^2 \mathbf{A}. \end{aligned} \tag{2.73}$$

Clearly this can be simplified for large κ, then by applying appropriate boundary conditions (the same as those used for surface superconductivity) de Gennes determined the maximum field for which there is a solution to be

$$H_s = H_c \tag{2.74}$$

He also found that at this field $f(0)$ (the reduced order parameter at the surface)

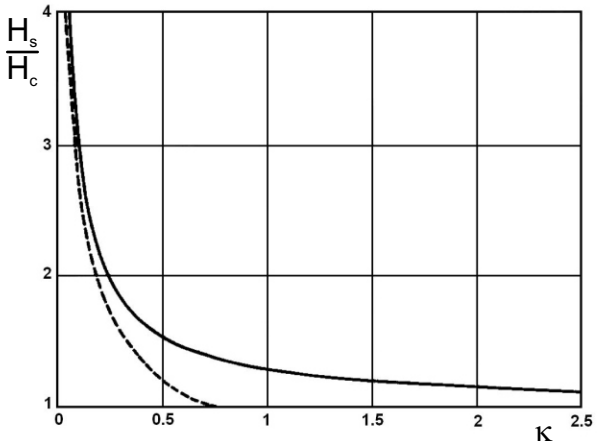

Figure 2.24: Superheating field as a function of κ as calculated by Matricon and Saint-James [47] for a range of κ. For small κ the result matches that of the Orsay group [46] (shown as the dotted line) and for large κ $H_s \rightarrow H_c$ as expected form de Gennes [45].

goes from 1 in zero field, to zero at H_s, i.e. there is a barrier to flux entry until the order parameter is completely suppressed at the surface.

This method has been extended to type I superconductors by the Orsay group [46] for $\kappa << 1$. In this case the one-dimensional GL equations and boundary conditions are simplified by noting that for $\lambda << \xi$ in the region $x < \lambda$ f is nearly constant ($f \sim f(0)$) and for $x > \lambda$ $\mathbf{A}$ is negligible and can be omitted from the equations. The maximum field above which there is no solution is then found to be

$$H_s = \kappa^{-\frac{1}{2}} 2^{-\frac{1}{4}} H_c. \tag{2.75}$$

This time $f(0)$ is found to decrease from 1 to $1/\sqrt{2}$ with no solutions below this. This suggests that the barrier field increases to infinity as $\kappa \rightarrow 0$. At first glance this superheating effect may seem extreme, but makes sense when considering the following: the magnetic field penetrates a superconductor to a depth of λ, while the Cooper pair interactions, i.e. the excitations that influence n_s at the surface, are spread out over a distance ξ, meaning that for $\lambda << \xi$ the ability of the magnetic field to depress the order parameter is much weaker than when λ and ξ are comparable in length. It then follows that for small values of κ much higher magnetic fields are needed to overcome this barrier effect.

Later work by Matricon and Saint-James [47] has determined the superheating fields for values of κ between these two extremes by solving the exact one-dimensional GL equations rather than simplified versions of them. Their results

are shown in figure 2.24 and confirm the earlier results for small and large values of κ.

These results assume that all the instabilities of interest are displayed in one dimension, although there is no guarantee that this is the case. Indeed when the Orsay group published their predictions the then available experimental data had found much lower levels of superheating, for instance Garfunkel and Serin [48] found $H_s = 1.17H_c$ in tin rather than the predicted value of $2.7H_c$ (assuming $\kappa = 0.1$). This suggested that either the above assumption is wrong, for instance the effect of thermal excitations may need to be considered, or that the experimental samples had not been prepared rigorously enough, such as with the minimisation of surface defects. It was only with later results, for example the work on indium spheres by Fink *et al.* [49], [35], where more careful treatment of the surfaces allowed the effects of defects to be removed and the predicted superheating fields to be observed.

More recently time-dependent 2D GL simulations [50] show agreement with the results of Matricon and Saint-James, the time-dependent nature of the simulations allow thermal noise fluctuations to be considered and are shown to be negligible for low temperature superconductors. This work also shows, like the work on indium spheres, the importance of the surface preparation. A coating of a normal conductor changes the boundary conditions such that the order parameter is already zero at the surface of the superconductor, this removes the surface barrier and hence no superheating is seen. Similarly defects will also depress the order parameter at the surface reducing the superheating field. An important result found by Feder in [35] is that as the size of the surface defects becomes negligible compared to $\xi(T)$ and $\lambda(T)$ their effects on superheating and supercooling disappear.

2.11 The Geometrical Barrier

So far demagnetising fields have only been considered for uniform ellipsoids and their limiting cases. To understand a wider range of real world behaviour it is important to consider what role demagnetising fields play in different geometries and how this may change the behaviour of the intermediate state. Some of the earliest work done in this direction was by Provost *et al.* [51] who carried out a systematic investigation into Pb disks with different shaped edges in order to

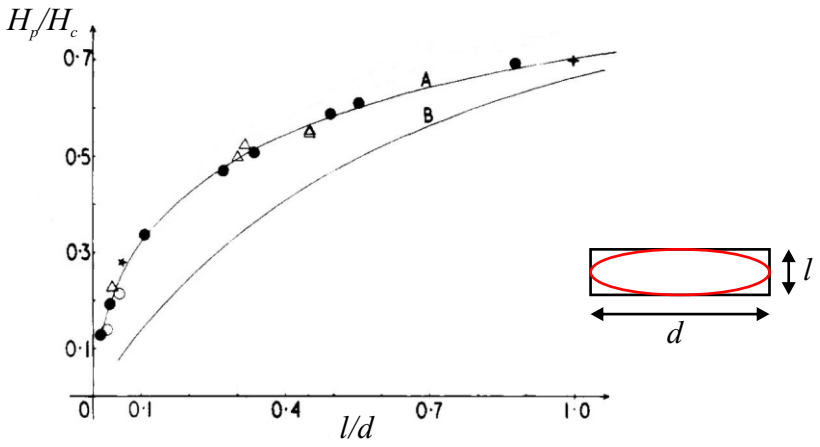

Figure 2.25: Normalised penetration field, H_p/H_c, vs. aspect ratio, l/d, for thin Pb disks with rectangular cross sections, from [51]. Experimental data points match well with the computed dependence, shown in curve A. Curve B shows the penetration field for an inscribed ellipsoid, illustrated in the sketch.

better understand previous results showing irreversible magnetisation behaviour. The cross sections of the disks ranged from elliptical, getting progressively flatter, to rectangular. Elliptical disks were found to have reversible magnetisations, with the magnetisations becoming more irreversible the flatter the disks became and the field of first penetration, H_p also increasing. An ellipse with diameter d and thickness l will, for $l/d << 1$, have a demagnetising factor of $\eta = 1 - \frac{l}{d}$ [52]. One would therefore expect a value of H_p for a thin disk to be $\approx (l/d)H_c$, instead it is found to be $\approx \sqrt{l/d}H_c$ for disks with rectangular cross sections, as shown in figure 2.25. The mechanism leading to such irreversible behaviour was more fully explained by Fortini *et al.* [53] and [54].

The simplest way to explain the observed behaviour is by reference to a superconductor with a rectangular cross section as in figure 2.26. The demagnetising effect is strongest at the corners and so the local field here will quickly rise to H_c even in low applied fields allowing flux to penetrate. At this point the penetration of flux through the corners is reversible, this means that if the field is reduced the flux will leave the corners and the magnetisation of the sample will return to the original value. As the field is increased flux cuts through more of the corners increasing the length of the flux tube penetrating the sample. Clearly at some point the total length of the penetrating flux will be longer than if a flux tube passed through the sample in a straight line. Because the energy of the flux tube is proportional to its length, and if one also takes into account the relaxation of magnetic field lines that occurs when flux penetrates, it should be apparent that

a lower energy state will be achieved by allowing the flux to penetrate through the body of the superconductor rather than through the corners. It is important to note that this point is reached before the flux penetrating the opposite corners meet at the equator. Flux is unable to spontaneously form within a superconductor, a consequence of fluxoid quantisation, instead it must migrate in from the edges. Hence flux cannot penetrate through the body until the size of the normal corners increases to a point when they touch, which will happen when the local field at the equator reaches H_c. It should also be noted that this will occur at a higher applied field than for an ellipsoid with the same aspect ratio due to the energy cost associated with flux penetrating the corners. Because there is a delay in flux entering the body of the superconductor, and hence reaching a lower energy state, it can be said that there is a potential barrier due to the sample edge.

Originally this was referred to as "edge pinning", but after the effect was found to also apply in type II high temperature superconductors, [55] and [56], it is more commonly labelled a "geometrical barrier". Once a flux tube penetrates all the way through a superconductor its encircling supercurrents will interact with the Meissner screening currents, resulting in the flux tube being rapidly pushed into the centre of the sample. After a flux tube has entered the superconductor the field around the edges will relax, thus raising the barrier behind it meaning the field has to be increased to allow more flux in. If the applied field is now reduced the Meissner currents will still apply a force to the normal domain preventing its exit, hence the magnetisation has become irreversible. The process of flux penetration is illustrated in figure 2.26.

This situation differs considerably from the case of a sample with an elliptical cross section for the following reason. In this case, as already covered, the field is greatest at the equator so when the local field reaches H_c here flux will penetrate in a straight line that increases with length as it moves into the superconductor. Again the flux tube experiences an inward force from the Meissner screening currents, but it turns out that this is exactly compensated for by the increase in energy due to the increase in flux length for a given field [57]. Flux only moves further into the superconductor if the applied field is increased. Similarly when the applied field is reduced the shortening of the flux line compensates for the repulsion from the Meissner currents meaning the magnetisation is fully reversible. Hence there is no longer a potential barrier preventing a lower energy

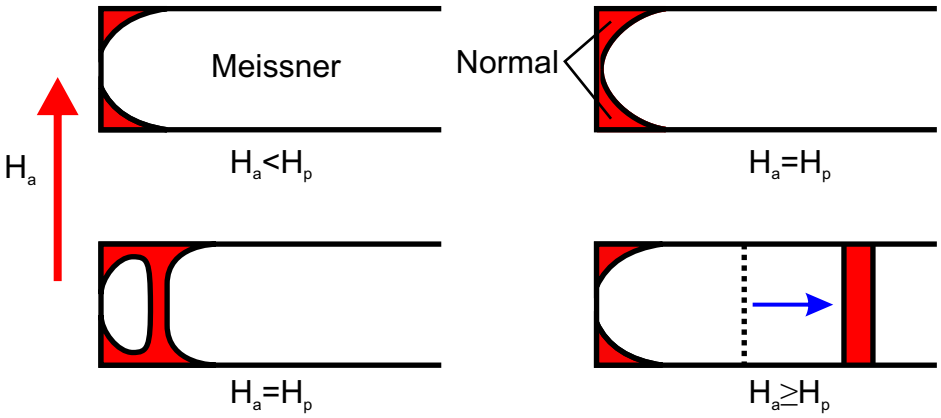

Figure 2.26: Sketch illustrating process of flux penetration into a rectangular cross sectioned superconductor in a perpendicular field.

state being achieved and so the geometrical barrier does not exist for samples with elliptical cross sections.

Other work has since been done to consider how more general shapes may give rise to a geometrical barrier. For instance Benkraouda and Clem [58] analysed a superconducting strip with a flat top and bottom, but with rounded edges. Like samples with elliptical cross sections the field is strongest at the equator and flux will penetrate reversibly in the same way through the edge sections. However, as soon as flux spans the flat sections of the strip the length of the flux stops increasing with penetration and the flux will again be pushed to the centre by the Meissner currents which will again prevent the flux from leaving if the field is reduced. The magnetisation will therefore be irreversible and the geometrical barrier still exists. The penetration field in this case is found to be $H_p = \left(1 + \sqrt{d/l}\right)^{-1} H_c$.

Another example is given by Morozov *et al.* [59] who investigates a prism geometry and find that it shows fully reversible behaviour. This does however differ from the behaviour of an ellipsoid as flux penetrates more slowly with increasing field. The general behaviour found is that in large fields, i.e lots of flux penetration, ellipsoids show a uniform field distribution while cross sections that are more tapered, such as the prism investigated, have the field concentrated towards the edges. Cross sections that are flatter than an ellipsoid have the field concentrated in the centre and show irreversible magnetisation, i.e. they display a geometrical barrier.

It is important to note that the geometrical barrier is independent of sample size and is readily seen in bulk sized superconductors. This is in stark contrast to the surface barriers that are responsible for superheating where the requirement for almost defect free surfaces makes its observation very difficult in large samples.

Chapter 3

Electrochemistry

There are several methods that can be employed to create mesoscopic superconductors. Previous work has largely focused on lithographic patterning of thin films, for example [5] and [60]. This method generally involves developing a pattern in photoresist, using optical or electron beam lithography, and thermally evaporating a metal film. An example of the results that can be obtained using this method is shown in figure 3(a). The drawback with this method is that it can only create 2D shapes, which tend to be thin, pollycrystalline metals meaning that they are invariably type II superconductors. Another method is focused ion beam (FIB) induced chemical vapour deposition, for example [61] and [62]. This method works by introducing a precursor gas containing the the desired material in the vicinity of the FIB. The FIB decomposes the gas with the volatile component being extracted by the vacuum system and the non-volatile component, e.g. a metal, being deposited. Whilst it can be used to create 3D structures, as shown in fig 3(b), it is difficult to control the 3D shape and the resulting sample is amorphous, containing a large fraction of carbon.

Electrodeposition uses a current to drive metal ions out of a solution and deposit them onto a substrate. This can be used in conjunction with nanoscale templates attached to the substrate, so that the deposited metal fills the space in the template. This method has been very successful at reproducibly creating arrays of nanowires that have uniform diameters and lengths [63], [64], an example of a nanowire grown using this method is shown in figure 3(c). This method does however limit the shape of the structures grown to the form defined

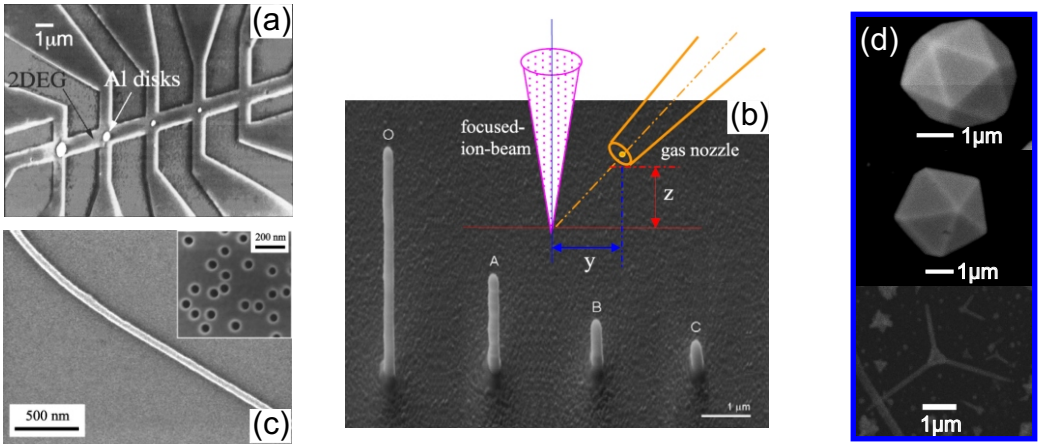

Figure 3.1: (a) Al disks deposited onto a Hall array using lithographic techniques from [5]. (b) 3D nano pillars grown using focused ion beam induced chemical vapour deposition from [62]. (c) nanowire grown using electrochemical deposition through a nanoscale template, shown in the inset, from [64]. (d) Examples of 3D Pb mesostructures grown by electrodeposition in the course of this work.

by the template. Electrodeposition can be performed without using a template where, by sacrificing some uniformity of the structures a much wider variety of mesostructures can be grown, including 3D crystallites, thin films and nanowires. By very careful control of deposition parameters the architecture can be reliably 'tuned' [7], [65], and it is possible to grow structures with very smooth faces and sharp facets. It is because such a wide range of well formed mesostructures can be grown with a good deal of predictability that this method is used in this work.

3.1 Introduction

Electrochemistry dates back to Allesandro Volta's discovery in 1793 that electricity can be produced by placing two dissimilar metals on opposite sides of a moistened paper. In 1800, Nicholson and Carlisle showed that an electric current could decompose water into oxygen and hydrogen, and in 1805 Luigi V. Brugnatelli performed the first electrodeposition.

If a metal is immersed in pure water a small number of metal atoms will enter into solution as ions, leaving electrons in the metal:

$$M(s) \rightarrow M^{x+} + xe^{-}. \tag{3.1}$$

As metal ions go into solution, a positive charge will build up in the solution and

a negative charge will build up in the metal. This makes it harder for additional ions to enter into solution. This generally means that very quickly the process comes to a halt, leaving a solution with a low concentration of metal ions (this is not necessarily true for highly reactive metals). In order for the above reaction to continue it is necessary for it to be coupled to some process that acts to restore electroneutrality. One way of achieving this is to remove excess electrons by passing them through an external circuit that forms a complete electrochemical cell. As electrons are 'drained' from the metal, more metal ions can enter into solution. Conversely, by reversing the cell and forcing electrons into the metal, we can reverse this process and enable metal ions to come out of solution and deposit onto the metal.

In electrochemical systems interest is focused on the transport of charge across the interface between chemical phases, typically an electronic conductor (electrode) and an ionic conductor (electrolyte). The electrode - electrolyte interface behaves similarly to a capacitor and this interfacial region is known as the electrical double layer. The electrode is covered by a sheath of solvent molecules and ions that are said to be specifically adsorbed. The plane that passes through the centre of these molecules is known as the inner Helmholtz plane (IHP). Because of this sheath, solvated ions can only approach the electrode to a limited distance, known as the outer Helmholtz plane (OHP). These ions interact with the electrode via long-range electrostatic forces and are said to be non-specifically adsorbed. Because of thermal agitation in the solution, these solvated ions are spread out over what is known as the diffuse layer.

Electrostatic forces that tend to attract or repel ions counterbalance random thermal motion in the diffuse layer, resulting in a non-uniform distribution of ions near the surface. Beyond the diffuse layer there are no electrostatic forces from the electrode and ions in the homogeneous bulk solution phase are not affected by the electrode. Hence it can be said that in the bulk solution electroneutrality exists and the potential, ϕ, is independent of distance. In fact the potential diminishes exponentially from the surface of the electrode over a very short distance (figure 3.1). The thickness of the diffuse layer is typically of the order of 10nm and the higher the ionic concentration, the thinner the diffuse layer.

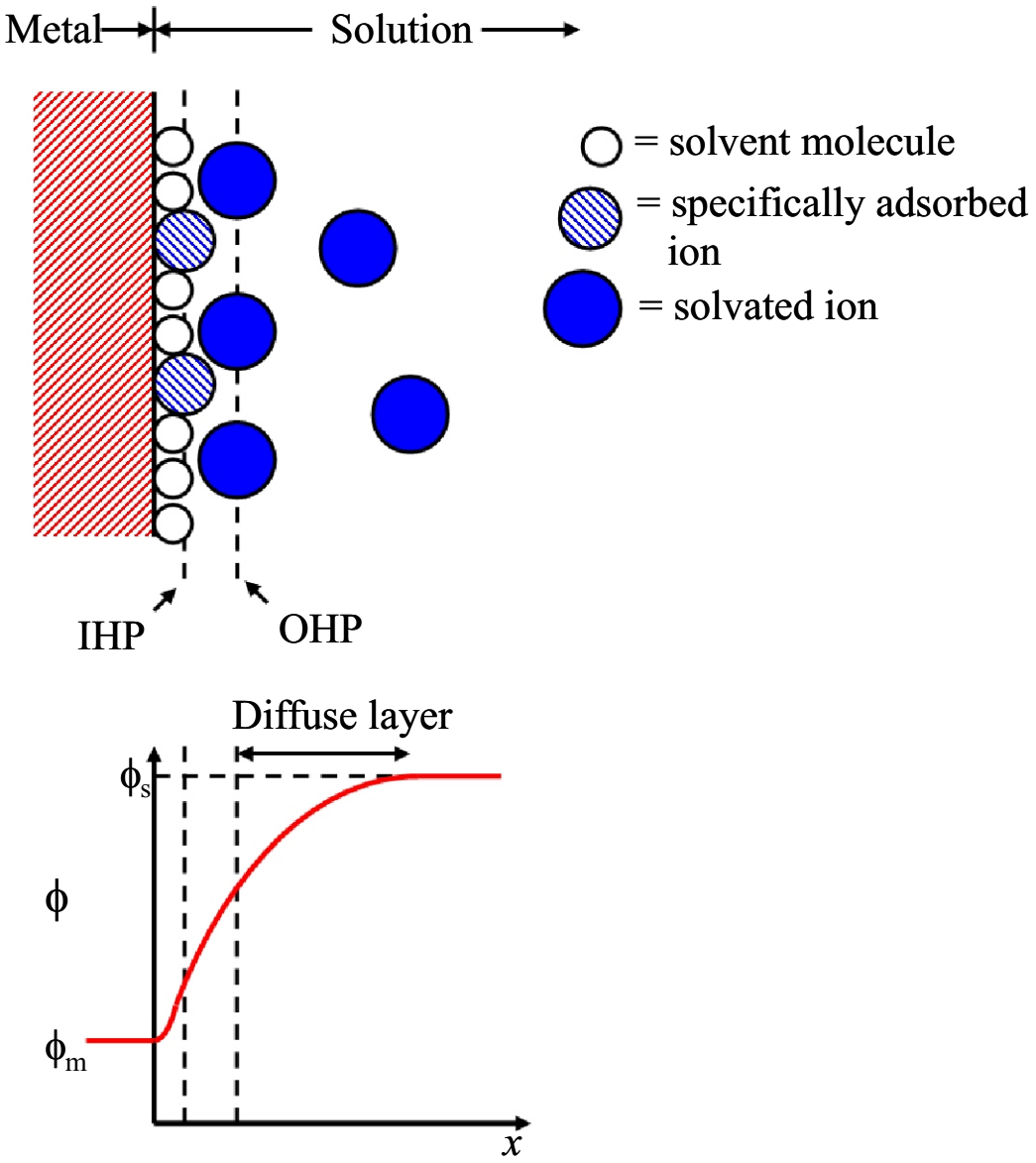

Figure 3.2: Proposed model for electrode - solution interface, the important features highlighted are the inner Helmholtz plane (IHP) and the outer Helmholtz plane (OHP). The potential profile, ϕ, across this region is shown underneath where the potential at the surface of the metal electrode, ϕ_m, decays exponentially to a constant value, ϕ_s, in the bulk solution.

3.2 Electrochemical cells

Electrochemical cells that have current flowing through them can be split into two groups, galvanic cells and electrolytic cells. A galvanic cell is one where reactions occur spontaneously at the electrodes when they are connected by an electrically conducting path through which a useful current can flow. These cells are typically used in batteries. In an electrolytic cell, an externally supplied electric current is used to drive a reaction that would not occur spontaneously. Electrodeposition is carried out using electrolytic cells.

A simple electrolytic cell for electrodeposition involves a metal ion solution, an electrode that also acts as a surface to be deposited onto, known as the working electrode, and another electrode used to complete the circuit and enable a voltage to be applied between the solution and the working electrode, known as the counter electrode. The counter electrode is typically an unreactive metal. Metal will be deposited onto the working electrode when a minimum voltage is applied across the two electrodes. This reaction depends on the potential difference between the bulk solution and the working electrode. It is however not possible to measure this due to the electrical double layer between any electrode and the bulk solution. This is because any electrode used to measure the potential difference will have its own, unknown, potential difference between it and the bulk solution, as demonstrated in figure 3.3. Therefore, to retain accurate control of the potential it is necessary to measure the relative potential difference rather than the absolute potential.

In a two electrode system, the counter electrode is used to complete the circuit and allow current to flow through the cell, and it is assumed to maintain a constant interfacial potential difference regardless of the current. These two functions are often mutually exclusive however as the flow of current causes both electrodes to become polarised, meaning the potential difference between the bulk solution and both electrodes will change by an unknown amount. Hence a third, reference, electrode is needed to serve the second function. By not drawing current its potential remains fixed and so provides a stable reference point to measure the applied voltage against throughout the experiment.

To accurately control the applied potential in a 3 electrode system, a potentiostat is used. This allows a current to flow between the working and counter electrodes

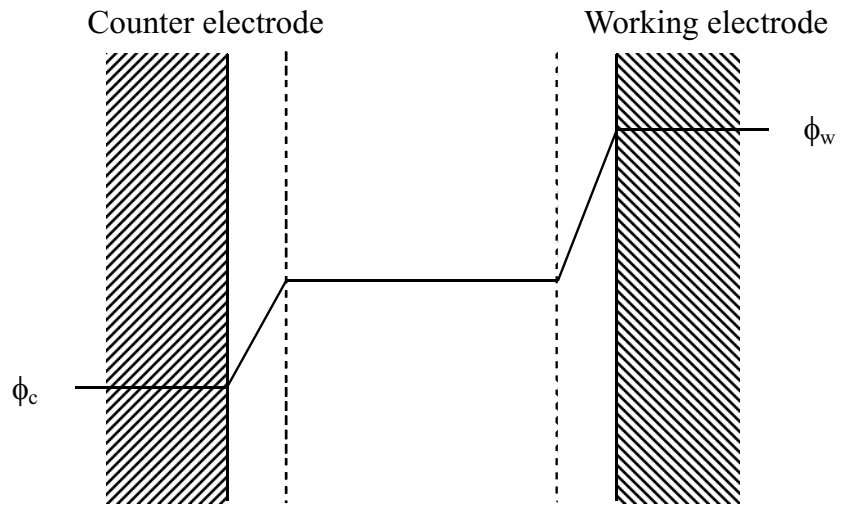

Figure 3.3: Schematic representation of potential gradients in a two electrode electrochemical cell. ϕ_c and ϕ_w represent the potential at the surface of the counter and working electrodes respectively.

whilst using a feedback circuit to control the potential applied at the counter electrode so that the true potential remains constant at the working electrode as measured by the reference electrode. For a more in-depth look at potentiostat operation the reader is referred to [66].

3.3 Crystal growth

There are many good sources of information giving an overview of crystal growth e.g. [67], [68], [69]. Some of the main concepts are introduced below.

When two bulk phases are in equilibrium any driving force that acts to disrupt the equilibrium will quickly be reflected in transforming one phase to another so that they regain equilibrium. However if there is only one bulk phase, any driving force to form a new phase will have to overcome an energy barrier to formation. If a driving force is applied that is not able to overcome the energy barrier the system is said to be supersaturated, or in metastable equilibrium. An example of such a system is a superheated or supercooled liquid. New phases necessarily form in such systems as nuclei - small clusters of molecules that are of sufficient size to form spontaneously.

The nucleation of species is usually discussed in terms of reduction in the Gibbs free energy of a system and can be described by classical nucleation theory that is

based on work by a number of people, including Gibbs [70], Volmer and Webber [71], Becker and Doring [72], Frakas [73] and others. This work originally referred to the condensation of a vapour from a liquid, but can be extended to nucleation of solids from melts and solutions [74]. The overall change in free energy, ΔG, of a system due to the formation of a small particle in solution is equal to the surface excess energy, ΔG_S, plus the volume excess energy, ΔG_V. ΔG_S is due to the interfacial tension between the particle and the supersaturated solution and is always positive, while ΔG_V is due to the formation of the bulk phase and is always negative. Assuming for simplicity a spherical small particle with radius r, then as might be expected ΔG_S is proportional to the surface area ($\propto r^2$) and ΔG_V is proportional to the volume ($\propto r^3$) of the particle. Hence

$$\begin{aligned} \Delta G &= \Delta G_S + \Delta G_V \\ &= 4\pi r^2 \gamma + \frac{4}{3}\pi r^3 \Delta G_v \end{aligned} \tag{3.2}$$

where γ is the interfacial tension, also know as the surface energy, and ΔG_v is the free energy of formation of the bulk phase per unit volume. For small values of r the surface energy term will be dominant and the change in free energy will be positive while for large values of r (i.e. bulk phases) the volume energy will dominate and the change in free energy will be negative. Clearly at some critical size there must be a crossover. By referring to figure 3.4 it becomes clear that the important turning point is reached when $d(\Delta G)/dr = 0$. At this point it is said that it has reached a critical radius, $r = r_c$, and differentiating equation 3.2 with respect to r gives

$$\frac{\Delta G}{dr} = 8\pi r\gamma + 4\pi r^2 \Delta G_v = 0 \tag{3.3}$$

Hence

$$r_c = -\frac{2\gamma}{\Delta G_v} \tag{3.4}$$

Below this size, a particle will minimise its energy by decreasing in size until it disappears and above this size a particle will minimise its energy by continuing to grow. Hence it is said that r_c represents the critical size of a stable nucleus.

The situation outlined above refers to nucleation of an isolated particle within a single phase and is known as homogeneous nucleation. For the case of electrodeposition, where the nucleation of crystals takes place on a substrate, the process is known as heterogeneous nucleation. In this case the barrier to formation of a

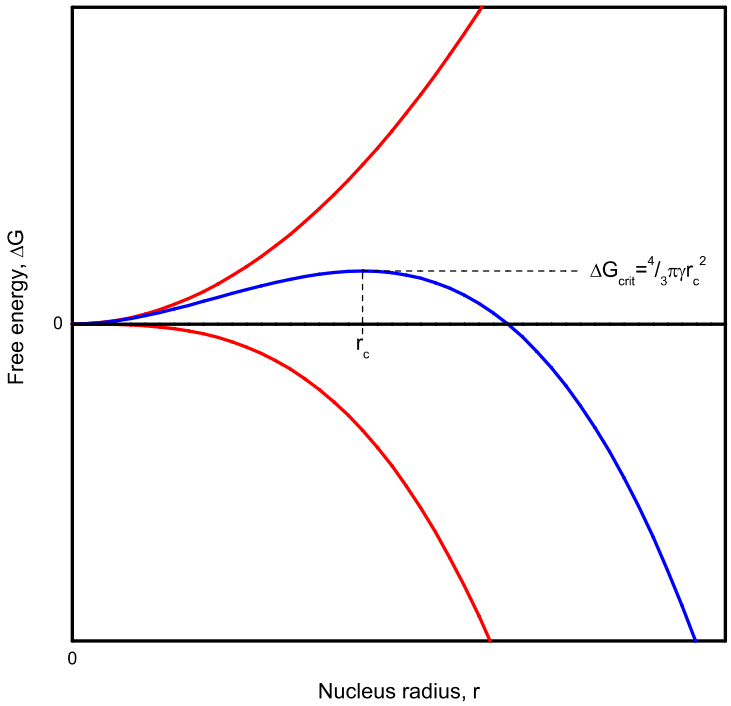

Figure 3.4: Free energy diagram illustrating the existence of a critical radius.

new phase can be much lower. The simplest way of explaining this is that for a given volume, the surface area in contact with the solution will be comparatively smaller when on a substrate than when floating in solution, thus reducing the positive energy contribution from the surface energy. For the same reason the most energetically favourable nucleation sites on a substrate will be at steps and cavities within the substrate. A more thorough review of this process can be found in [74].

The form in which an electrodeposited nucleus grows can be categorised into three distinct modes, as illustrated in figure 3.5. The growth mode is determined by several factors, perhaps the most important being the relative free energies of the electrochemically reduced metal and the electrode surface, which in turn is related to the nature and strength of the chemical bonds of the two species, and the crystallographic mismatch of their lattices. Other factors include the deposition rate and substrate temperature. For high surface free energies where there are strong chemical bonds and the atoms of the deposit are more tightly bound to the substrate than to atoms of the same crystal, the deposit will grow two dimensionally, layer by layer. If there is little lattice mismatch the metal will continue to grow in this manner, known as Frank-van der Merwe (FM) growth. However, a large lattice mismatch results in a strain energy being induced within

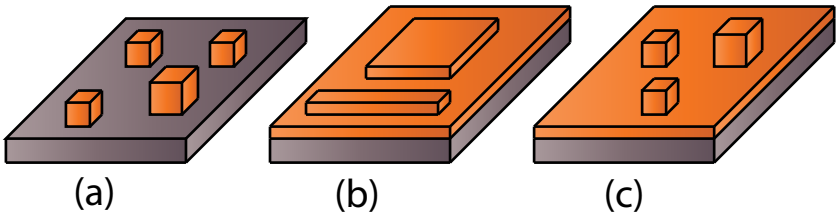

Figure 3.5: Diagram illustrating the three crystal growth modes (a) Volmer - Weber (b) Frank-van der Merwe (c) Stranski-Krastanov.

the structure of the deposited metal that increases with thickness [67]. Once a critical thickness has been reached the strain is relieved by the crystal forming 3D islands in a mode known as Stranski-Krastanov (SK) growth.

For substrates with low surface free energies, the lowest energy state is achieved by the nuclei growing as isolated 3D islands so that as little of the substrate surface is covered as possible. This is known as Volmer - Weber (VW) growth. VW growth was first shown to occur in electrodeposition by Zoval *et al.* [75]. Obviously for mesostructure growth it is necessary for the metals to be deposited in a VW growth regime, hence the need for a working electrode with a low surface energy. The substrate of choice tends to be highly oriented pyrolytic graphite (HOPG) for several reasons; it has an extremely low surface energy, low resistivity, excellent chemical inertness, and also HOPG can be grown largely defect free, providing large flat growth surfaces for mesostructure growth.

Distribution of metal nuclei on HOPG surfaces is pseudo random. Nuclei are aligned at step edges on the surface that are randomly generated each time the top layer is stripped off, whilst terraces are almost electrochemically inert [76]. This pseudo random distribution is partly responsible for an effect that can alter the growth of mesostructures that is known as interparticle diffusion coupling (IDC) [77]. When a metal particle grows by electrodeposition, it depletes the local solution of metal ions. A hemisphere of depleted solution, known as a depletion layer, will grow around the metal particle as the particle grows during the course of the deposition. If a particle is a large distance from other metal particles then it will not be affected. If, on the other hand, it is close to another metal particle then there will be an overlap of the depletion layers of each particle. This will slow the growth of the particles and can affect their geometries. For example, a particle that has another particle next to it on one side and nothing on the other will grow faster on the empty side. This effect will broaden the size distribution of deposited

mesostructures and can cause particles to grow asymmetrically. IDC can be avoided in several ways. Upon stirring the electrolyte, ions will diffuse back into the depleted layers faster making it less likely that there will be diffusional overlap. The increased agitation can however cause mesostructures to move allowing them to coalesce resulting in multi, rather than single, crystal mesostructures. A double potential step method can be used. This involves applying a large potential for a short period of time (ms) to nucleate centres on the substrate, and then the potential is reduced to a lower value sufficient to grow these centres while preventing further nucleation. Alternatively, if there is a low enough nucleation number density then the nuclei will generally not be close enough to suffer from IDC.

3.4 Pb Mesostructure Growth

Similar to crystal nucleation, the growth of a small crystal is concerned with minimising the Gibbs free energy of the system, which due to the large surface area to volume ratio of a small crystal will be highly dependent on its shape. At a constant volume the lowest energy state is dependent solely on minimising the surface energy that is achieved by forming the equilibrium shape. The equilibrium shape of a crystal must take into account the crystal lattice, different crystal faces have different crystallographic orientations and therefore different surface energies.

Crystal growth primarily occurs at steps on crystal faces as illustrated in figure 3.6. In figure 3.6 a growth unit can attach to a terrace site (a), a smooth edge (b) or a kink (c) and by doing so will attach to 1, 2 or 3 nearest neighbours respectively. The more bonds a growth unit forms with the growing crystal the lower its energy, hence the most energetically favourable growth sites are kinks. When a growth unit attaches at a kink site, it creates another kink and this process will continue until the kinks and steps of a face have been filled out creating a smooth surface. For growth to continue on such defect free surfaces it is necessary to form a 2D nucleus to provide fresh kinks and steps. As with the original nucleation this involves an initial increase in the Gibbs free energy, providing an energy barrier to the process. This causes the whole growth process to proceed layer by layer.

As shown by Xiao *et al.* [7], Pb mesostructures can be electrodeposited in a variety

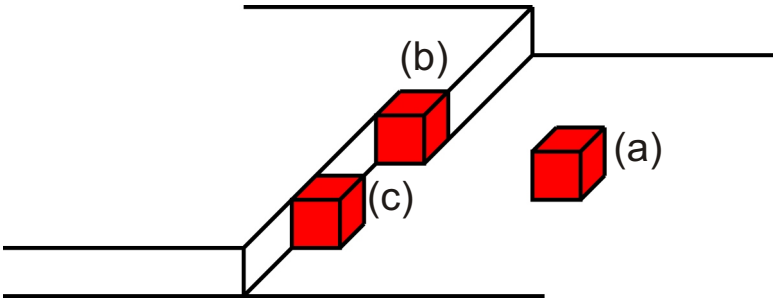

Figure 3.6: Diagram illustrating the positions available to growth units on a crystal face for a simple cubic lattice.

of shapes. These can mostly be split into 3 different categories; 3D crystals that have a pentagonal symmetry, 2D platelets that are either hexagonal or triangular in shape and 1D nanowires. The type of crystal grown is strongly linked to the reduction potential, the reduction potential being equal to the chemical potential of the electrode surface and the deposited crystals. As the reduction potential is increased, the dimensionality of the crystals grown decreases. The lower the dimensionality the larger the surface to volume ratio. As stated previously this increases the energy barrier to growth, hence the need for larger reduction potentials. The reduction potential also determines the rate of growth of the crystals. For small reduction potentials, the crystals grow slowly allowing the lowest energy state to be achieved. For very fast growth speeds the current density at the growth faces will reach the limiting diffusion current density, that is the local metal ions have been depleted and new ions are deposited at a rate determined by how quickly they diffuse into the depletion zone. It has been observed that dendrites can not grow unless this condition is met [78], [79], [80]. In this case deposition is favoured at the corners of crystals as they have the largest surface area giving them greater access to diffused ions. This growth method creates a higher surface area to volume ratio compared to more 3D growth modes, making it energetically unfavourable at smaller potentials.

According to classical crystallographic rules, the rotational symmetry of a crystal is limited to 1, 2, 3, 4 or 6-fold. It is relatively simple to show that 5-fold symmetry is forbidden in a crystal constructed from a regularly repeating unit cell on a discrete lattice. This is known as the crystallographic restriction theorem. It is perhaps unsurprising then that there has been a large amount of interest in a set of small crystals with pentagonal symmetry, usually decahedrons or icosahedrons, in the last few decades. These are known as multiply twinned particles (MTPs), sometimes referred to as pentagonal small particles (PSPs). They were

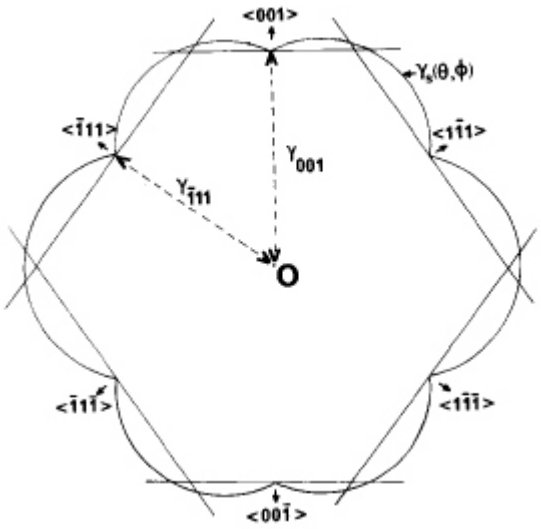

Figure 3.7: An example of a 2D Wulff construction for an fcc crystal on a (110) plane, recreated from [88].

first discovered in the early stages of epitaxial growth, almost simultaneously by Ino [81], Ino and Ogawa [82] and Allpress and Sanders [83]. There appears to be a general consensus, e.g. [84], [85], that such structures are possible due to disclinations within the crystal structure, and form because they represent intrinsic equilibrium structures that have lower energy than more conventional shapes at small sizes.

The equilibrium shape of a crystal for a fixed volume is determined by the Wulff construction, named after Georg Wulff who performed much of the early experimental work on equilibrium shapes [86]. Wulff stated that the energy of a crystal surface is proportional to the length of a vector from a common origin to the normal of a crystal face. The surface free energy for a given face has the form $\gamma_s(\theta,\phi)$ as a function of the normal direction, where θ and ϕ are spherical polar coordinates. A Wulff construction can be made by plotting this surface energy as a function of orientation then drawing the plane to the normal of this surface. This is then repeated for all crystal faces and the equilibrium shape is made up of the inner envelope of these planes. An example of this in 2D is given in figure 3.7 . This method gives the equilibrium shape for a free floating single crystal, and can be extended to crystals on a substrate [87] by including a component for the energy of adhesion for the surface in contact with the substrate.

The above method, however, only applies to single crystals and does not consider

the possibility of twinned particles. A twinned particle is created when two crystals share the same lattice points on an internal face symmetrically. By associating the energy of the twin boundary with the separate crystals within a twinned particle, Marks [88], [89] was able to consider these boundaries as external facets for individual crystals and use a Wulff construction to determine their minimum surface energy configuration. Marks used this modified Wulff construction on the structures described originally by Ino [81] and Ino and Ogawa [82], and was able to confirm that such structures represent stable equilibrium shapes. The fundamental reason why these MTP structures form is that they contain more low energy faces than single crystals of the same volume, specifically more (111) facets and less (001), while the energy of the twin boundaries are negligibly small. The total surface energies obtained for different structures were found to be in the order single crystal > decahedra > icosahedra.

The decahedra and icosahedra are made up of tetrahedral single crystals, with five in the decahedron and twenty in the icosahedron. These assemblies are not fully space filling so some form of strain must be introduced. Originally a homogeneous strain was suggested by Ino *et al.* but a more refined approach was suggested by deWit [90], of an inhomogeneous strain in the form of a disclination which is now widely accepted as the correct model e.g. [84], [85] [91]. A disclination is a rotational symmetry violation in the form of a line defect and perhaps best imagined as adding or subtracting a wedge of material and joining the faces of the cut e.g figure 3.8. The deficiency of a decahedron is a wedge of about 7.5 degrees and so can be accounted for by a single disclination, an icosahedron is slightly more complicated in that it needs 6 such disclinations.

Howie and Marks [92] extended the previous work of Marks on the modified Wulff construction to include these strains and showed that they increase with volume. This indicates that there is a stability range in terms of size of the MTP, beyond which they no longer represent the lowest energy state. Similar conclusions have been reached by others, e.g. [85]. It should be noted, however, that this does not mean there is some cut-off size, beyond which it is impossible to find MTPs. A MTP that has reached a certain size is likely to carry on growing as to turn into a single crystal would require large changes in the internal structure providing a large energy barrier to this process. In such instances the MTP would not represent the minimum energy configuration, rather it would relate to a local minimum.

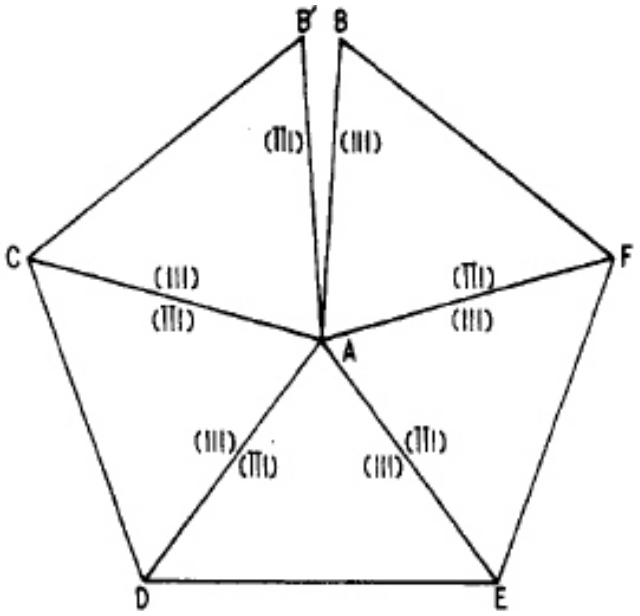

Figure 3.8: Sketch illustrating the angular gap caused by tetrahedra on a crystal lattice not being entirely space filling. In a MTP points B and B' are joined, forming a disclination. Recreated from [90].

As described by Wranglen [93], the platelet crystals are formed from a tetrahedral pyramid growth centre. The faces of the pyramid grow laterally forming a flat topped equilateral triangle. The edges of the triangle continue to grow outwards laterally but at a faster rate than the corners causing the triangle to become truncated and hence forming a hexagon. Under ideal conditions all sides will become equal and continue growing at the same rate. A schematic of this process is given in figure 3.9 alongside S.E.M. images of Pb crystals.

Again referring to Wranglen [93], the nanowires form from octahedral crystals, growing rapidly outwards layer by layer in a straight line along the (110) plane. This mode of growth results in a needle-like nanowire that is tapered at either end, a schematic of this growth mechanism and a SEM image of a typical Pb nanowire are shown side by side in figure 3.10. At even higher voltages growth centres are able to nucleate on the side of the nanowires leading to the growth of side branches and the formation of nanobrushes.

3.5 Experimental Setup

A PTFE electrochemical cell with a standard 3 electrode setup was used (figure 3.11). The cell was regularly cleaned using acetone and IPA in an ultrasonic

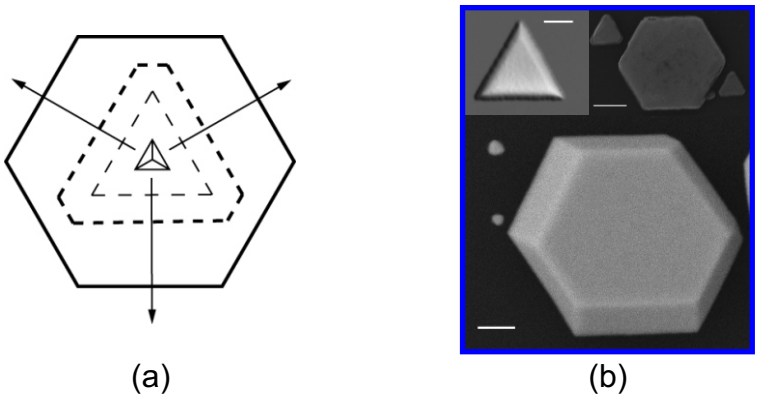

Figure 3.9: (a) Schematic showing growth process of a Pb platelet crystal. (b) S.E.M. images of Pb crystals grown during the course of this work. The scale bar in each image is $1\mu m$.

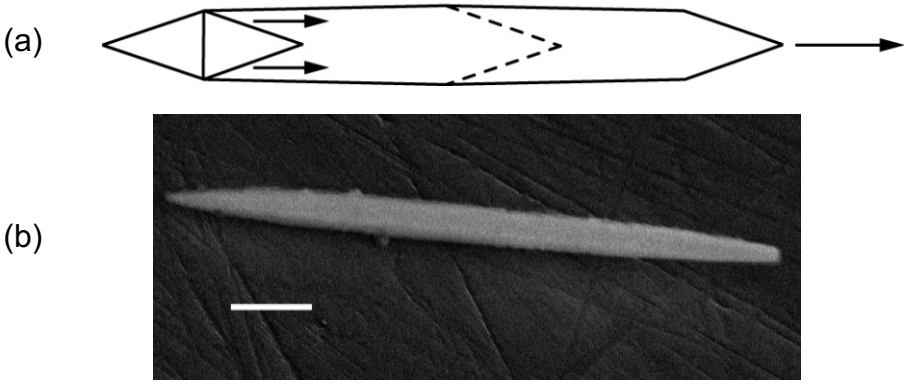

Figure 3.10: Sketch showing the growth process of a Pb nanowire (a) alongside a S.E.M. image of a Pb nanowire grown during the course of this work for comparison (b). The scale bar is $1\mu m$.

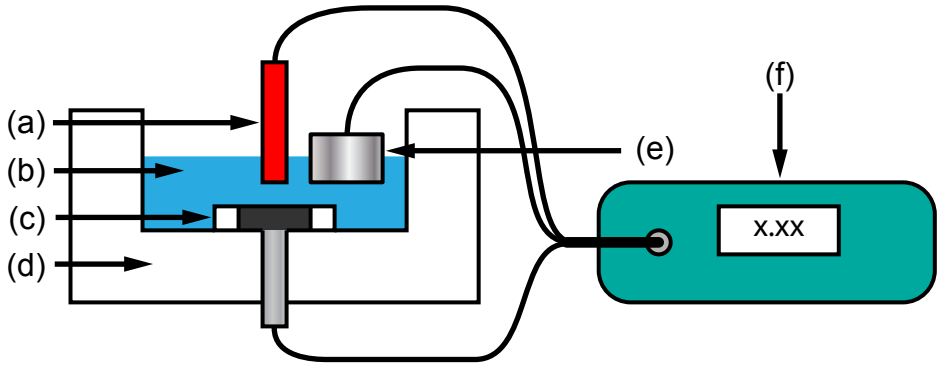

Figure 3.11: Schematic diagram of electrochemical setup. (a) Reference electrode. (b) Electrolyte. (c) Working electrode. (d) PTFE cell. (e) Counter electrode. (f) Potentiostat.

bath. The electrolyte was made up of a dilute metal solution, either Pb nitrate or Pb acetate between 1mM and 10mM, and a buffer solution of either boric acid between 0.1M and 0.4M, or 0.1M nitric acid. All solutions were made with $>$ 18MΩ D.I. water from a millipore water system, using high purity reagents (99.95% or greater) weighed on a precision balance. The counter electrode was a square of platinum foil 1.5 cm by 1.5 cm and the reference electrode was a Ag/AgCl wire. This reference electrode was chosen as it supplies a stable, well defined potential and is easy to make. A fresh reference electrode is made at the start of each set of depositions using a clean silver wire as a working electrode in a saturated NaCl solution in a two electrode setup. A Cl layer is deposited onto the silver wire by applying a potential of +2V for about 10s. A working electrode of either HOPG or boron doped diamond (BDD) was used. The HOPG was cleaned by stripping the top layer off using Scotch tape, while the BDD was cleaned using acetone and IPA in an ultrasonic bath, followed by polishing with an alumina slurry (Buehler Alpha micropolish, 1μm alumina suspension in DI water) on a polishing cloth (Buehler Microcloth) and then rinsing in DI water. The potential was applied using an MicroAutolabIII potentiostat. This was typically between -0.6V and -1.5V vs the reference electrode for between 10 and 60 seconds. After crystals have been deposited, the electrolyte is poured out of the cell and the working electrode is washed with IPA then DI water and finally blown dry with argon. The crystals were then examined under an optical microscope, AFM or SEM.

Chapter 4

Hall Magnetometry

4.1 The Hall Effect

The method used in this work to determine the magnetisation of samples is based on the Hall effect. The Hall effect was discovered in 1879 by Edwin Hall [94] and arises from the interaction between charge carriers and magnetic field, which results in a voltage that is proportional to the component of the magnetic field in a particular direction.

If a charge carrier, in this case an electron, moves through a material with drift velocity v_d, as in Figure 4.1, then when a magnetic field is applied the carrier will experience a Lorentz force, $\mathbf{F_L}$, perpendicular to both the magnetic field and the current.

The Lorentz force results in a build up of charge on one surface, in this case a negative charge at the top. This charge separation results in the development of

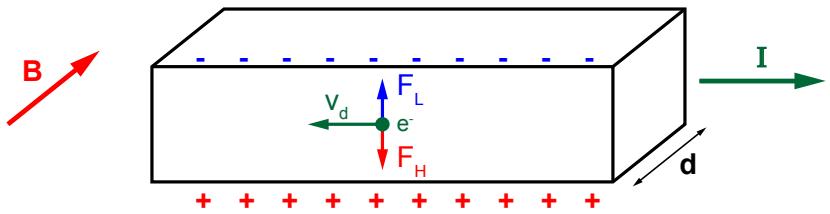

Figure 4.1: Sketch showing the forces acting on an electron moving through a charge carrier in a magnetic field, resulting in the Hall effect.

an electric field across the bar known as the Hall field, $\mathbf{E_H}$. This field will exert a force, $\mathbf{F_H}$, on the charge carriers that will directly oppose the Lorentz force. As more charge carriers move towards one side the Hall field will increase until equilibrium is reached when $\mathbf{F_L}$ equals $\mathbf{F_H}$ and the charge carriers move parallel to the initial direction of current.

The Hall field that now acts on the material causes a Hall voltage, V_H, to develop across the material. The Hall voltage is given by the following expression

$$V_H = R_H I B \tag{4.1}$$

Hence the voltage across the material is directly proportional to the magnitude of the magnetic field though the material. Here R_H is the Hall coefficient, defined as $\frac{1}{nqd}$ where d is the thickness of the material and n is the carrier density. As will be seen in the next section, for the Hall probes used in this work the charge carriers are concentrated in a 2 dimensional electron gas (2DEG). In this instance it is more common to replace the product of the 3D carrier density and thickness from above with a 2D carrier density, n_{2D}.

From equation 4.1 it follows that the sensitivity of the Hall probe will be dependent on the Hall coefficient and the applied current. Hence it is possible to increase the sensitivity of a Hall probe by reducing its carrier density or increasing the current. This is a major reason why semiconductors are generally used instead of metals in Hall probes as they have a far lower carrier density. The maximum current that can be applied in semiconductor Hall probes is usually limited by the saturation drift velocity, $v_{sat}(I_{max} \sim newv_{sat})$, or self-heating effects at room temperature, and by heating or impact ionisation at low temperature.

Perhaps the most important figure of merit for a Hall probe is the signal to noise ratio (SNR). For the types of Hall probes used in this work the SNR is usually found to be limited by the Johnson noise due to the resistance of the voltage contacts, R_V, e.g. [95] and [96]. The root mean square (RMS) voltage of the Johnson noise for a given bandwidth, Δf, is given by

$$V_N = \sqrt{4kTR_V\Delta f} \tag{4.2}$$

Hence the SNR is

$$\text{SNR} = \frac{I_{max}R_H B}{\sqrt{4kTR_V\Delta f}} \tag{4.3}$$

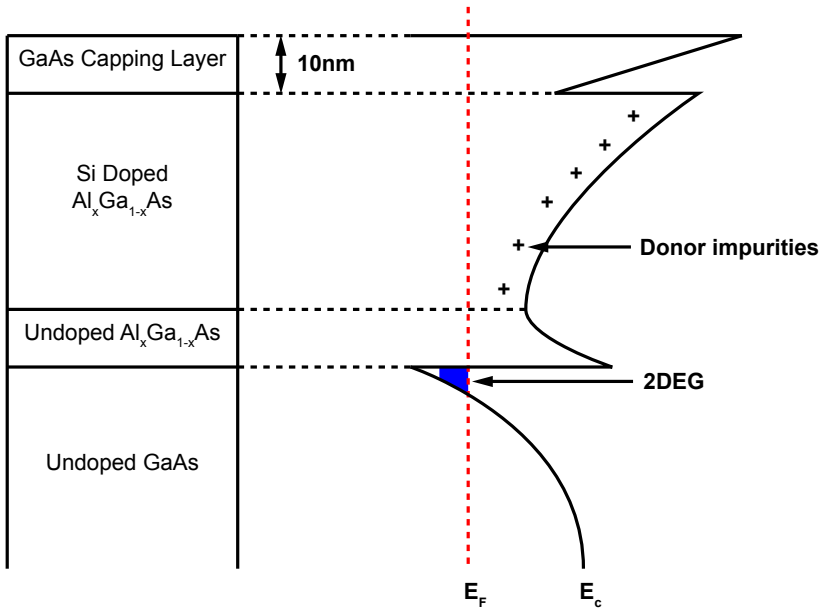

Figure 4.2: Layer structure of typical AlGaAs/GaAs heterostructure (left) and conduction band profile across the heterostructure (right).

where

$$R_V = \frac{1}{\mu n_{2D} e w} \tag{4.4}$$

and μ is the mobility of the charge carriers, w is the width of the junction. It therefore follows that

$$\text{SNR} \approx \sqrt{\frac{\mu}{n_{2D}}} \times I_{max} \tag{4.5}$$

Clearly the largest SNR will be obtained by choosing a material with a large μ and small n.

4.2 2DEG

A 2 dimensional electron gas (2DEG) is formed when one dimension is reduced so that there is no motion in that direction. 2DEGs are most commonly found in metal oxide field effect transistors (MOSFETs) where the electrons are confined to an interface between a layer of silicon and a thin SiO_2 insulating layer when a positive voltage is applied to a metal gate on top of this layer.

An alternative method of forming a 2DEG in III-V heterostructures is possible because the lattice constants of GaAs and AlAs are almost identical (atomic separations of 5.653Å and 5.660Å respectively [97]) but the band gap is different.

The band gap can be engineered by replacing a certain fraction, x, of the Ga atoms with Al to form $Al_xGa_{1-x}As$ and with the development of molecular beam epitaxy (MBE) it is now possible to control the doping of individual atomic layers grown on GaAs wafers. The interface formed between the two regions is known as a heterojunction. The difference in band gaps leads to the conduction and valence bands being modulated across the junction whilst the Fermi energy remains constant. This creates a v-shaped potential well that traps electrons at the interface to form a 2DEG, as shown in Figure 4.2. One major benefit of making 2DEGs in this way is that it allows modulation doping to be used [98]. This is a method where the Si-doped AlGaAs layer, which is used to promote conduction electrons to the conduction band, is separated from the undoped GaAs layer by an undoped AlGaAs layer. This increase in distance of impurities from the 2DEG virtually eliminates ionized impurity scattering caused by the Si dopants, which at low temperature is the dominant form of scattering and hence limits electron mobility. This greatly increases the electron mobility and hence the mean free path at low temperature, although it has little effect at higher temperatures where phonon scattering dominates.

A combination of low ionised impurity scattering and quenching of phonon scattering at low temperature, and low carrier densities in typical AlGaAs/GaAs heterostructure material means that they make excellent Hall probes for low temperature work with high sensitivity and a high SNR.

4.3 Hall Magnetometry

By using microfabricated AlGaAs/GaAs heterostructures it is possible to achieve not only excellent SNR with extremely low minimum detectable fields, but the high mobility at low temperature and the potentially small size of the Hall probes means that the electrons will move ballistically inside the Hall cross at low temperatures, i.e. the mean free path of the electrons is much larger than the width of the Hall cross. This has a distinct advantage over the case when electrons move diffusively. In the diffusive regime the Hall response depends on the field distribution within and near the Hall cross [99], severely complicating any attempt to accurately measure the magnetisation of the sample. When in the ballistic limit it has been shown [100] that the Hall effect simply measures the average magnetic

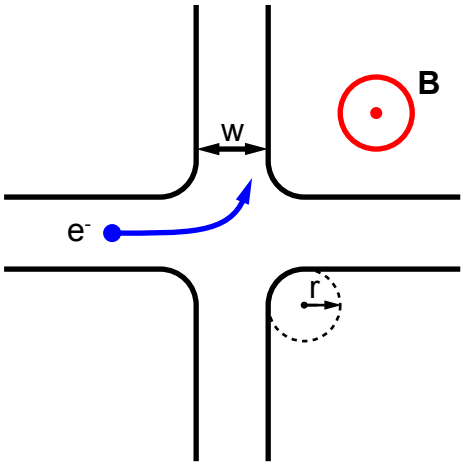

Figure 4.3: Simplified layout of a Hall cross in two dimensions showing important dimensions and electron motion in an applied field.

induction, $\langle B \rangle$, across the junction via the following simple relationship

$$R_H = \frac{\alpha \langle B \rangle}{n_{2D} e} \tag{4.6}$$

where α is a coefficient which accounts for the collimation effects of ballistic electrons. Collimation effects become more complex with increased rounding of the corners of a Hall cross, e.g. [101] and [102], but the above relationship still applies for typical devices with slightly rounded corners of radius r [103] where the average induction is taken over an area $(w+1.4r)^2$ ($\alpha \sim 1.2$ for these devices), see figure 4.3. $\langle B \rangle$ is proportional to the flux through the area of the Hall cross, hence a ballistic Hall cross will act like a micro-fluxmeter with a tiny detection loop. Knowing the average magnetic induction it is possible to define the area magnetisation as

$$M = \frac{\langle B \rangle}{\mu_0} - H \tag{4.7}$$

where H is the externally applied magnetic field. $\langle B \rangle / \mu_0$ is directly proportional to the Hall voltage so it is possible to calibrate this against a known magnetic field and hence convert the voltage into units of magnetisation.

It is important to be wary of a few experimental complications that affect ballistic Hall magnetometry. Firstly, the Hall probe will only give an accurate measure of the average magnetic inductance through it so long as the applied field is small enough such that the cyclotron orbit is much larger than the width of the junction. If the cyclotron orbit becomes smaller than the width of the junction

then the electrons will move in skipping orbits along the edge of the junction leading to the Hall response being influenced by the magnetic field in the leads and not just the junction. Secondly if the corners of the Hall cross are too rounded electrons can be 'guided' in moderate fields leading to a plateaux in the Hall response at moderate fields [104]. However this is only a problem for a corner radius larger than the width of the cross, hence it is important to make the corners nominally straight. Finally collimation effects and mesoscopic resistance fluctuations can lead to a non-linear, probe-specific background response. Such background signals can be hard to distinguish from a sample response but can be taken into account by measuring the field response above T_c and subtracting this from the sample response.

4.4 Hall Probe Design

Efficiency is improved by measuring multiple samples and so as many Hall probes as possible are put onto a chip. The best way to do this is in a linear array that allows the same current to be passed down all the Hall probes simultaneously, using only two contact pads for the current leads. There is a limit to the number of Hall probes that can be put onto each chip due to the limited number of contact pads that are able to fit on the chip, which in this case is 22. In total nine Hall probes are put in the linear array as can be seen in Figure 4.5(c).

The smaller the size of the Hall probe, the better the spatial resolution that can be obtained. The Hall probes that have been fabricated for this work have a one micron width, which is about the limit of optical lithography. Because the Hall probes are arranged in a linear array and the width of each Hall probe so small, it is important to make the leads fan out from each Hall cross. A one micron lead connecting each Hall probe would have too high a resistance and be far too susceptible to damage. If one of the current leads from a Hall probe is damaged it will prevent the use of that Hall probe and the Hall probe next to it. It is however possible to use one of the voltage leads from a Hall probe as a backup current lead so that the rest of the array can still be used.

4.5 Hall Probe Fabrication

Fabrication of the GaAs/AlGaAs 2DEG Hall probe arrays used during the course of this work was carried out using standard optical photolithographic and chemical wet etching techniques as outlined below and in figure 4.4.

1. Sample preparation: The GaAs/AlGaAs wafer was scribed and then cleaved into chips 3.75 × 3.75 mm. These chips were then cleaned by placing them in beakers of (i) 1-1-1 trichloroethane, (ii) acetone and (iii) isopropanol, in an ultrasonic bath for 5 minutes in each solvent. The chips were then blown dry with a nitrogen gun and stuck onto glass slides with photoresist to make them easier to handle.

2. Photolithography (for Ohmic contacts): Photoresist (Shipley Microposit 1813) was spun onto the chips at a speed of 5000 rpm for 30 seconds, which were then baked in an oven at 90°C for 15 minutes. They were then taken out and soaked in chlorobenzene for 3 minutes, blown dry and put back in the oven for another 15 minutes. The chips were then exposed to ultraviolet light for about 20 seconds through a chrome mask to define the Ohmic contacts, before the photoresist was developed in Microposit 351 developer for roughly 20 seconds. This removed the areas of photoresist exposed to the ultraviolet light, which was where the contacts were to be deposited as shown in figure 4.4(a). To stop the photoresist from developing further, the chips were washed in deionised water and then dried. The chlorobenzene step is used as it hardens the top layer of the photoresist so that when the features are developed the bottom layer of the photoresist will develop more, resulting in an overhanging profile. This is important as it ensures that the contact pads will not be accidentally removed during the lift-off procedure.

3. Ohmic contacts: Each chip was dipped in a solution of 1:1 HCl:H_2O for 30 seconds and then washed in deionised water to remove any surface oxides. The chips were then immediately placed into a thermal evaporator and put under high vacuum. An argon glow discharge was applied for 10 minutes to clean the surfaces of the chips. 66 nm of Ge and then 134 nm of Au were deposited, which produce a good Ohmic contact to the 2DEG when properly annealed, followed by 20nm of Ti and a further 200nm of Au, which provides a good surface for bonding wires to. After removal from the

evaporator, the chips were placed in acetone and put in an ultrasonic bath at low power. This lifts-off the unwanted metal regions, leaving just the defined contact pads as shown in figures 4.4(b) and (c).

4. Annealing: After being cleaned, each chip was placed in an annealer and the contacts annealed in a 95% N_2/5% H_2 reducing atmosphere at 430°C for 2 minutes. This produces an n^+ region below the pads which makes a low resistance Ohmic contact to the 2DEG.

5. Photolithography (for wet etching): The chips were cleaned and remounted as above, and photoresist was spun on at 5000rpm for 30 seconds. This time however they were baked for 30 minutes at 90°C, skipping the chlorobenze step. The chips were then exposed to ultraviolet light for about 2 minutes through an edgebead removal mask. The chips were then developed for about 15 seconds. This step removes all the photoresist around the edges of the chips, which are known as edgebeads. This is necessary so that when the chips are being exposed to ultraviolet light it is possible to get the mask into very close contact allowing the fine detail features to be developed properly. Occasionally the edgebeads are so thick that they will not be completely removed by this step. In this case, rather than risking overdeveloping the photoresist, it is better to fold a fine tissue in four then soaking the stiff corner in acetone and using this to carefully wipe the remaining edgebeads off by hand. This is not done for the Ohmic contacts as not only are the features so big it would make no noticeable difference, the removal of the photoresist from around the edge of the chip would result in metal being deposited there and possibly shorting out the contacts. The chips are then exposed again through an etch mask for roughly 6 seconds and then developed for 20 seconds, as can be seen in figure 4.4(d). This etch mask is used to expose the leads from the contact pads, although it does not expose the fine detail of the central Hall array, which is done in a separate photolithography/etching step using a fine etch mask.

6. Etching: The chips were dipped in 1:1 HCl:H_2O for 30 seconds to remove the surface oxides immediately before etching. They were then etched in a solution of deionised water, 30% H_2O_2 and concentrated H_2SO_4 in the ratio 160:8:1. This produced an etch rate of about 0.26 μm/min that was calibrated against a spare piece of chip. The target depth was 100 nm so an etch time of 20 seconds was sufficient. After etching the chips were washed in deionised water and the remaining resist was removed with acetone (fig-

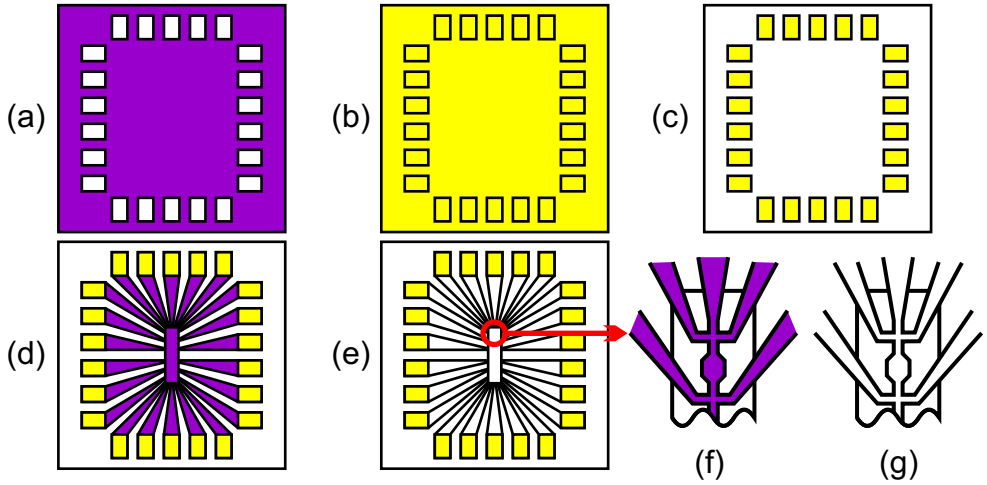

Figure 4.4: Steps for Hall array fabrication, as outlined in the text.

ure 4.4(e)). These last two steps were then repeated using a fine detail etch mask, figures 4.4(f) and (g), however this time an etch depth of about 40 nm was required. It is necessary to do this in two stages as etching occurs sideways as well as down, hence undercutting the photoresist. When etching fine details it is therefore necessary to etch as little as possible to avoid destroying small features, but it is a good idea to etch deeper for larger features, such as the leads to the Hall array, to ensure that the 2DEG is completely destroyed in these areas.

4.6 Experimental Apparatus

Once the Hall probe arrays have been fabricated it was necessary to mount them on chip carriers in order to be able to make measurements inside the cryostat. The chips were glued onto commercial ceramic leadless chip carriers using low temperature epoxy, which was cured at 100°C for 20 minutes (Figure 4.5(b)). The chip carrier and chip were electrically connected using an ultrasonic bonder that utilised 25μm diameter gold wire. This technique uses a pulse of ultrasonic energy to join the wire to the contact pads. Once attached to the chip carrier the Hall probe array can be easily plugged into the chip carrier socket that is attached to a copper sample head on the end of the sample rod. This is then inserted into the cryostat sample space which is sealed with an o-ring and clamp.

Also attached to the chip carrier socket are two side looking infra-red (IR) LEDs.

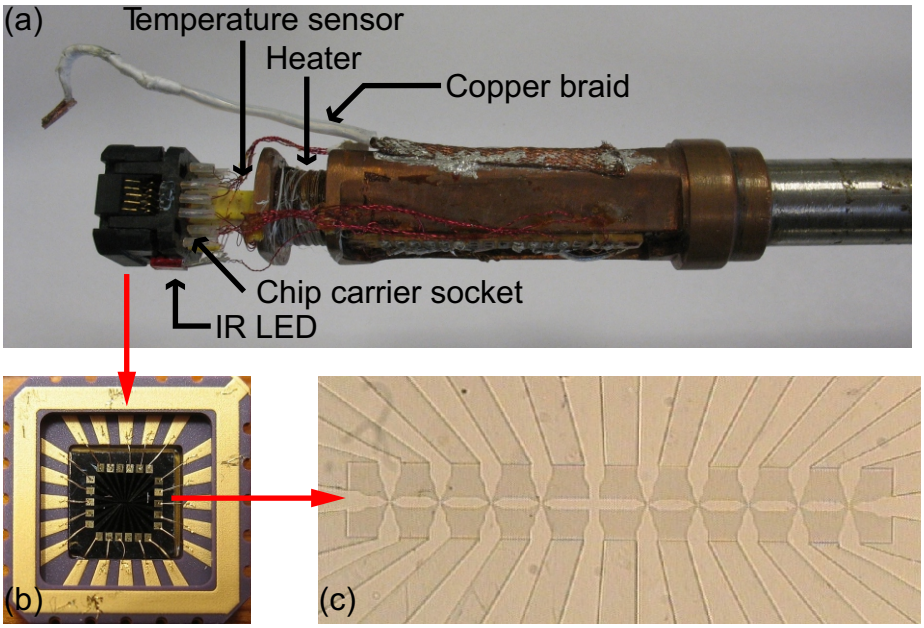

Figure 4.5: Cryostat insert. (a) Photograph of cryostat insert with labels pointing out the component parts. (b) Photograph of a Hall array glued into and bonded to a chip carrier. (c) Optical microscope image showing a magnified view of the Hall array.

These are used to illuminate the probes if they have excessively large resistances. This has the effect of exciting electrons from deep-donor states in the AlGaAs layer into the conduction band, (the persistent photoconductivity effect [105]) thereby reducing the probe resistance and improving the SNR at low temperatures. A hole has been drilled into the copper sample head so that a commercial carbon-glass temperature sensor can be embedded into it, close to the heater and the sample. There is no direct thermal link between the sample chip and copper body of the insert so one is made using a large piece of flexible copper braid that is soldered onto the insert at one end, and stuck to the back of the chip at the other. This is essential for temperature stability and accurate temperature measurements. A photograph of the cryostat insert is shown in Figure 4.5(a).

Electrical connections are made between the socket and the top of the sample rod using enamelled copper wires that are indium soldered onto the socket's gold plated legs. Indium (In) is preferred over the conventional Pb-Sn solder because of its lower critical superconducting temperature. Usually the cryostat does not operate below 4.2K so In, which has a T_c of 3.4K, will not become superconducting. Pb has a T_c of 7.2K, which could cause some problems at liquid helium temperatures and would certainly be an issue when taking measurements of Pb samples near their T_c. A breakout box plugs into the top of the sample

rod and allows connections to be made to the Hall probe array, the IR LEDs and the temperature sensor via BNC cables.

A diagram of the cryostat used is shown if Figure 4.6. The inner reservoir can be filled with either liquid helium for normal operation of 4.2K and above, or liquid nitrogen for 77K and above. It is also possible to pump on the reservoir to reduce these temperatures if required, and a temperature of 1.9K can be achieved by pumping on liquid helium. Regardless of what is in the inner cryogen reservoir, the outer cryogen reservoir is filled with liquid nitrogen, ensuring lower boil-off rates and hence a more temperature stable system.

The sample is cooled via helium exchange gas that is in contact with the walls of the sample chamber that is immersed in liquid helium. It is important to choose the pressure of the exchange gas to get the right balance between cooling to the sample and heating to the reservoir. Too low a pressure and there will not be enough cooling power to keep the temperature of the sample stable. Too high a pressure and the heater on the sample insert will cause the liquid helium to boil off at an excessive rate. A good balance was found to set the pressure to 50mbar at 100K. A lakeshore DRC-91CA temperature controller was configured to use the calibrated carbon-glass temperature sensor. This ensured high accuracy down to a stability of 0.01K at low temperatures.

The vacuum jacket of the inner Dewar was pumped down to a pressure of about 0.07mbar to provide good thermal insulation and hence slow the boil-off of cryogens. The vacuum jacket, sample space and inner dewar all connect to the same rotary pump but a series of valves allows each to be pumped on either independently or together, and for helium gas to be injected.

4.7 Making Magnetometry Measurements

To make magnetisation measurements on mesostructures it is first necessary to be able to place the mesostructures onto the Hall probe array with some precision. This is done in a number of stages using a piezoelectric micromanipulator with a step resolution of 200nm and an optical microscope with a 1000X magnification and a 3.4 mm working distance. The various steps involved, illustrated in figure 4.7, are as follows:

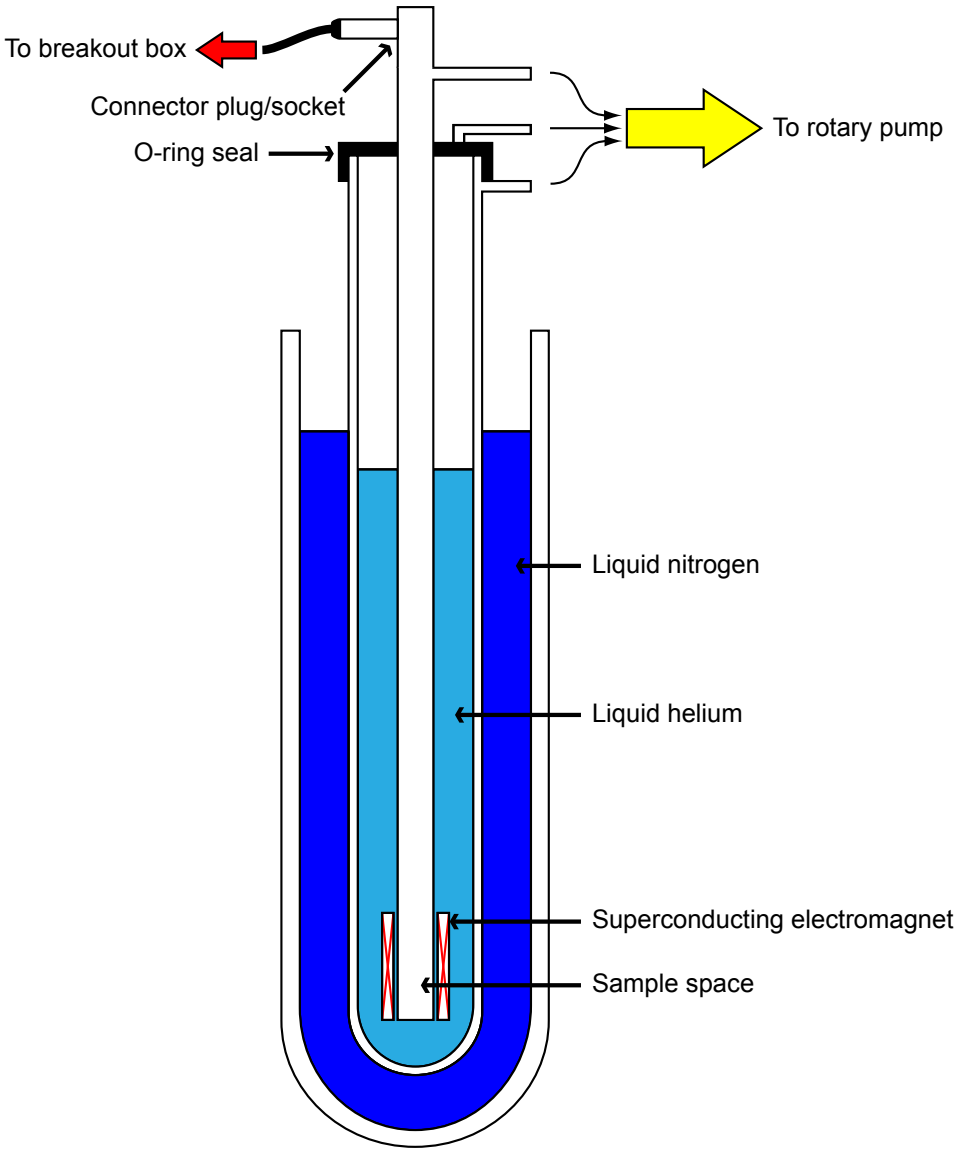

Figure 4.6: Schematic diagram of the cryostat used to make measurements.

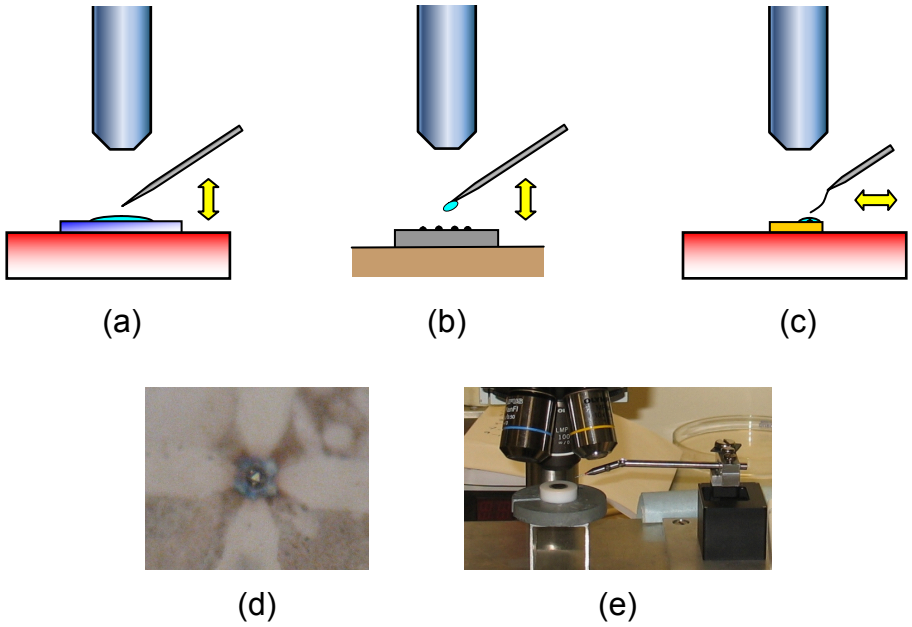

Figure 4.7: Micromanipulation of mesoscopic crystals. (a) - (c) sketches showing the various stages involved in picking up and moving around a crystal as described in the main text. (d) Optical image of a Pb crystal stuck onto a hall probe with paraffin wax. (e) Photograph of the micromanipulator setup with a working electrode.

(a) A small amount of paraffin wax is melted on a glass slide on a hot plate under the microscope. A tungsten tip with a point of 2μm is brought into contact with the melted wax so that a small blob, typically about 10μm in diameter, freezes around the end.

(b) The tip is withdrawn and the hot plate and glass slide are replaced by a working electrode with the desired deposited Pb samples on. A candidate crystal is selected using the microscope and the tungsten tip is brought down on top of it so that it is embedded in the wax. When the tip is lifted away the crystal is lifted off the surface.

(c) A Hall array is placed on the hot plate and the tungsten tip is brought down towards one of the leads of a Hall cross. When the paraffin wax touches the lead it will melt, depositing the embedded crystal. It is important to do this on a wide part of the lead far from the Hall cross as it is very easy to scratch the surface with a metal tip and hence destroy the Hall probe. The tungsten tip is then swapped for a thin nylon hair, the tip of which is usually less than 1μm across. This soft, flexible tip is used to push the crystal along the lead and into position on the Hall cross, the molten pool of wax acting as a lubricant making the task relatively straightforward.

(d) The Hall array is taken off the hot plate, allowing the wax to freeze onto the surface, both sticking the crystal in place and helping to protect it from oxidation. After a set of measurements the Hall array can be cleaned with acetone in a hot water bath set to about 60°C and used again.

To determine the magnetisation, M, of a sample it is necessary to measure the Hall voltage, V_H, from the Hall probe and the externally applied magnetic field, H. A superconducting coil that sits in the liquid helium bath is used to apply the field. The field is swept in small steps, usually of 1 or 2 G. After each step the Hall voltage is measured using either a Stanford Research SR830 digital lock-in amplifier, or a Princeton Applied Research 5210 analogue lock-in amplifier. If a second lock-in amplifier is used it is possible to simultaneously measure the response of a reference Hall probe with no sample on. The Hall current is modulated sinusoidally at 32Hz using a Philips PM 5109 low distortion RC generator. The magnitude of the current is set using a temperature-stable metal film resistor, either 1MΩ or 500KΩ for currents of 10μA or 20μA. This resistor is far larger than the resistance of the current path of the Hall array so it is reasonable to say the RC generator behaves as a current source.

Chapter 5

Superconducting Pb Nanowires

5.1 Introduction

As already mentioned, the majority of studies looking at mesoscopic superconductors have used nanopatterned thin films where the presence of disorder (e.g. in polycrystalline samples) and thin film geometries lead to type II behaviour. The nanowires studied here have been grown by electrodeposition, where the parameters are carefully controlled to ensure that the resulting nanowires are wide enough and clean enough to remain type I, but small enough to exhibit striking mesoscopic effects. Whilst there have been several previous studies looking at superconducting Pb nanowires grown by electrodeposition, this investigation takes a very different approach. For instance, previous studies have looked at much thinner polycrystalline nanowires, e.g. [106], or much thinner single crystal nanowires, e.g. [63] where the diameter of the nanowires was 50nm - smaller than the expected coherence length for all values of T. Both of these studies investigated the nanowire properties through transport measurements which gives less scope for characterisation of flux structures. Other investigations have used SQUID magnetometers to look at arrays of nanowires in a parallel field, e.g. [107] and [108]. However because a long cylinder in a parallel field has zero demagnetising factor, the ability to investigate the intermediate state in type I superconductors is limited in this type of arrangement. In the work presented here Hall magnetometry results of individual nanowires in a perpendicular magnetic field have been combined with 3D GL calculations in order to investigate

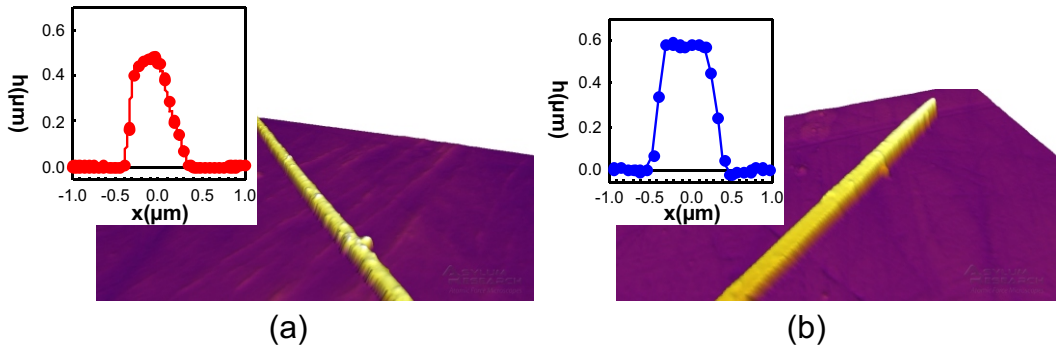

Figure 5.1: AFM images showing cross sections of nanowires grown using either Pb nitrate (a), or Pb acetate (b).

the flux patterns in these quasi 1D superconductors.

5.2 Experimental

The Pb nanowires studied here were grown by electrodeposition onto an HOPG electrode using the previously described method. As reported by Xiao *et al* [7] the cross section of the nanowire can be controlled through the choice of metal salt in the electrolyte. Nanowires with a round cross section can be grown using Pb nitrate and square cross sections can be achieved using Pb acetate. The results described here are for nanowires with a circular cross section, but both types of nanowire were grown and measured in an AFM, as shown in figure 5.1, so that it is possible to be confident of the cross sections of the nanowires investigated. An electrolyte of 5mM lead nitrate was used with a supporting electrolyte of 0.1M boric acid. The wires were grown by applying a reduction potential of -1.5V vs. an Ag/AgCl reference electrode for 60s.

Nanowires are placed onto the Hall probes using a slightly modified version of the previously described method. The nanowires readily stick to a nylon hair and so can be picked off of the working electrode without being embedded in paraffin wax, but getting them off of the hair onto the Hall probes is more challenging. This was achieved by melting a small amount of paraffin wax on the Hall probes, this helps to pull the nanowires off of the hair when they come into contact with the surface and also acts as lubrication allowing the nanowire to be pushed around on the surface and into position over the Hall cross. The majority of the wax evaporates before it resolidifies, the small amount left sticks the nanowire in place. The final positions of the nanowires can be seen in figure 5.2. The Hall

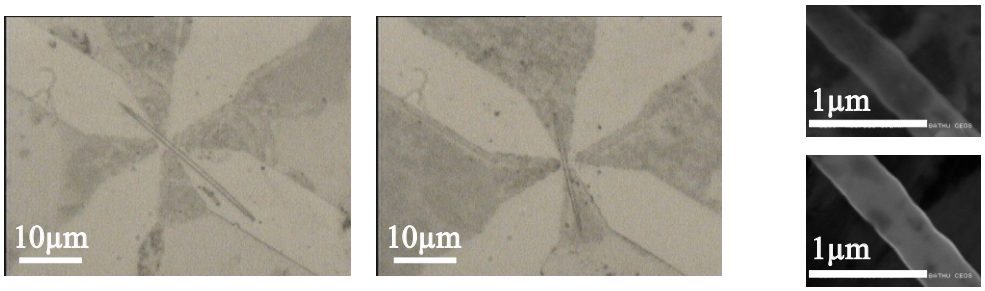

Figure 5.2: Optical images of the nanowires investigated in position on the Hall probes and SEM images of them taken after measurements had been taken.

probes were operated with a 20A 32Hz ac current and the Hall voltage detected with an analogue lock-in amplifier.

After all measurements were taken the samples were warmed up and moved from the Hall cross using the nylon hair. This was an attempt to pick up the nanowires and move them onto a different substrate in order to measure their dimensions via SEM, a necessary step as it is known that SEMs can damage 2DEG devices. Unfortunately the nanowires could not be removed from the Hall probes and were bent whilst attempting to do so. It was however possible to push them to one of the gold contact pads so that an SEM image could be taken and hence measure their widths (figure 5.2).

5.3 Results

Figure 5.3(a) shows several magnetisation loops for a 390nm diameter nanowire at different temperatures where the bulk critical fields, $H_c(T)$, are indicated by vertical dashed lines. In a bulk sample with the same cross-section fully reversible magnetisations would be expected to be seen due to the absence of the geometrical barrier in this cylindrical geometry [57], [51], [1]. Here however, it can be seen that there is a large degree of irreversibility, resulting from important superheating and surface superconductivity effects in mesoscopic samples. The ability to superheat a superconducting sample requires any surface defects to be smaller than the superconducting coherence length [35] and hence the phenomenon is not usually observed in bulk samples where it is very difficult to achieve such high quality surfaces. Surface superconductivity ultimately plays a much stronger role here than in bulk samples because the surface to volume ratio is so much larger in mesoscopic samples. As the applied field is increased from zero in all cases the

superconducting state is seen to survive to well above $H_c(T)$, clearly highlighting the role that surface superconductivity and superheating effects play in these nanowires. The presence of surface superconductivity leads to a small tail in the diamagnetic response at the end of the main superconductor-normal transition for $T \leq 5.6K$.

Surface superconductivity is theoretically expected to survive up to $H_{c3} \sim 2.39\kappa H_c$ [36], for a planar interface, where κ is the Ginzburg-Landau parameter and is known to have quite a strong temperature dependence in Pb; ~ 0.45 at $T \sim 0K$ and ~ 0.3 at $T \sim T_c$ for a clean bulk sample. For mesoscopic samples this temperature dependence can be different, depending on how ξ and λ change with T. For instance Stenuit *et al.* [108] find that $\lambda(T)$ is best approximated by the Gorter-Casimir two-fluid model where

$$\frac{\lambda_{GC}(T)}{\lambda_{GC}(0)} = \frac{1}{\sqrt{1-t^4}}, \tag{5.1}$$

where $t = T/T_c$. Combined with the $\xi(T)$ dependence of

$$\frac{\xi(T)}{\xi(0)} = \frac{1}{\sqrt{1-t}}. \tag{5.2}$$

This means that κ will vary with temperature as $[(1+t)(1+t^2)]^{-1/2}$. This temperature dependence agrees well with values of κ determined by transport measurements of Stenuit *et al.* for higher values of T, but diverges at lower values - Stenuit sees a flattening out of κ below $\sim 3K$.

This change in κ with T means that in Pb there is the unusual situation that H_{c3} exceeds H_c at low temperatures but falls below it near T_c when surface superconductivity no longer plays a role and the transition to the normal state becomes abrupt. This is further complicated in the mesoscopic regime due to additional enhancements of surface superconductivity when the size of the Cooper pair, ξ, becomes comparable to the size of the superconductor [38], [39]. For example in a thin slab in a parallel field this enhancement is predicted to occur when the ratio of the slab thickness to ξ becomes less than approximately 2.5, with H_{c3} then increasing rapidly with increasing confinement. Above this value H_{c3} is effectively independent of slab thickness. As the temperature increases ξ diverges as the temperature approaches T_c. The nanowires studied here are thick enough that confinement effects are negligible at very low temperature yet

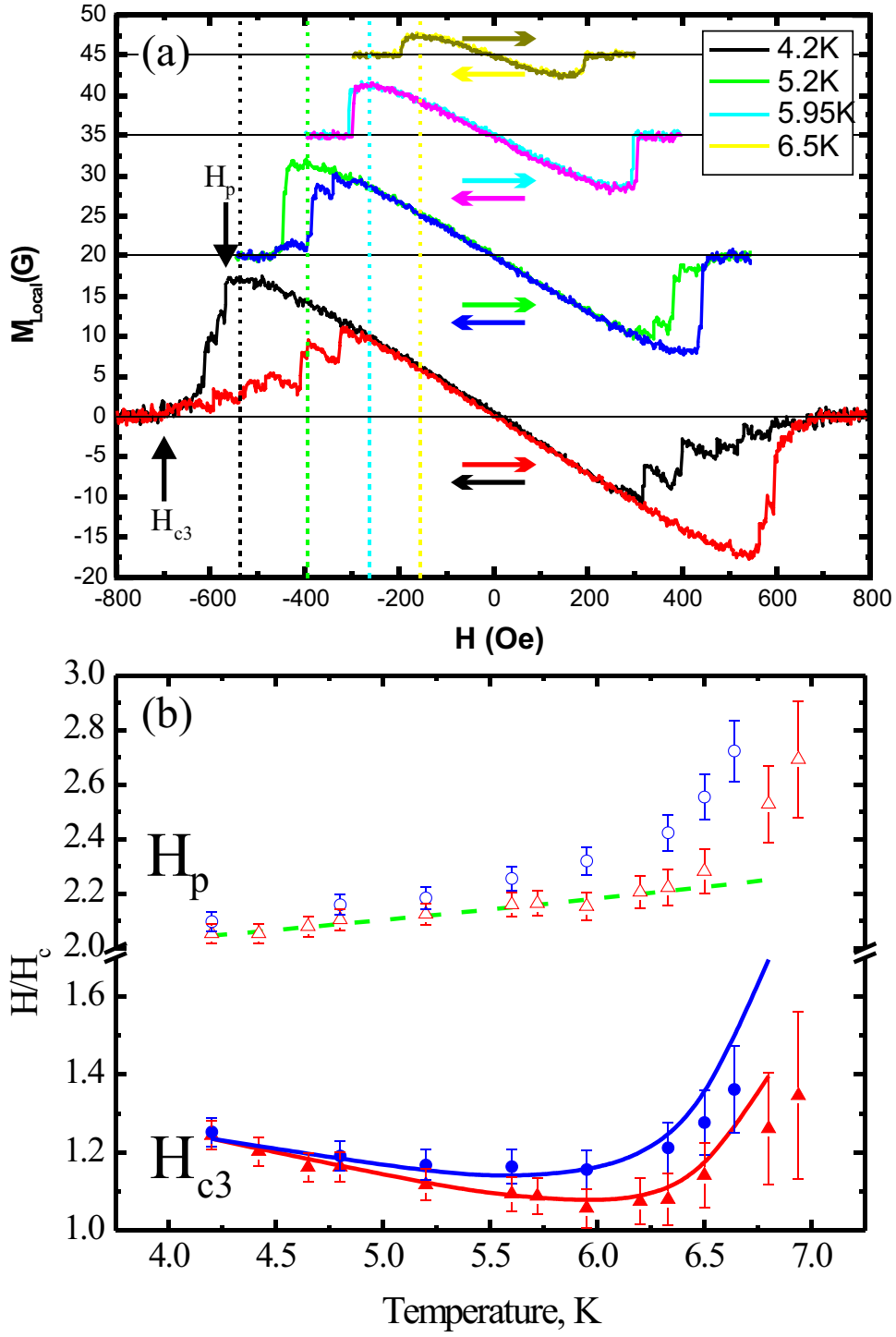

Figure 5.3: (a) Magnetisation curves at various temperatures for a 390nm diameter nanowire with a circular cross section. Dashed vertical lines show the bulk values of H_c for the different temperatures. Different colours represent different field sweep directions as indicated by the corresponding arrows. The arrows labelled H_{c3} and H_p illustrate the points taken for these values shown in (b). (b) Superheating field (H_p) and critical field of surface superconductivity (H_{c3}) acquired from magnetisation curves of nanowires with diameters of 390nm (circles) and 470nm (triangles) at different temperatures. Closed symbols show H_{c3} with the overlying solid line representing the expected value of a slab with the same thickness as obtained by Fink [38]. Open symbols show H_p corrected for the demagnetising factor, the dashed line shows the expected change in H_p with T, not the exact value, obtained from Matricon and Saint-James [47].

thin enough that these effects become significant at higher temperatures, even when T is not very close to T_c. As the temperature increases, this combination of decreasing κ and enhancement of H_{c3} at higher values of T leads to the situation shown in figure 5.3(b) where H_{c3} (normalised by the bulk H_c) is compared for two nanowires with different diameters, d. Here it can be seen that as T is increased there is an initial decrease in H_{c3} due to the decrease of κ before this trend is reversed due to the rapid increase in ξ close to T_c. As expected the enhancement of H_{c3} is more pronounced for the thinner nanowire but both nanowires have roughly the same value of H_{c3} at 4.2K where d/ξ is too large to affect this. As a rough guide the dependence of H_{c3} on T deduced from Fink's calculation of H_{c3} versus d/ξ for a thin slab, [38], has been included. This agrees very well with the measured results for most values of T, although there is some deviation as $T \rightarrow T_c$. The predicted values were determined by setting $\kappa(T_c)$ to 0.3, $\xi(0)$ to 83nm and using the above temperature dependences. Whilst these values are reasonable for a single crystal disorder-free nanowire, it is possible they are wrong. Indeed to obtain the same values of H_{c3}, the predicted values need to be multiplied by 1.25 (for both diameters of nanowire) although this is not unreasonable as there is likely to be an additional geometric enhancement for a nanowire geometry over that of a slab.

The temperature-dependence of κ also influences the superheating field which is known to increase approximately as $\kappa^{-0.5}$ for very small values of GL parameter. In order to determine if the superconductor exhibits superheating the field at which flux first penetrates, H_p, must be compared to the value expected taking into account the sample's demagnetisation factor. The demagnetisation factor for a bulk cylinder in a perpendicular magnetic field is 0.5, indicating that the magnetic fields at the surface are enhanced by a factor of two. This leads one to expect the first penetration of flux and formation of an intermediate state in these nanowires at $H = 0.5H_c$. In practice intermediate states are only observed for increasing fields at $T \leq 5.6K$ and always at $H_p > H_c$ just before the nanowire is driven completely normal. H_p is shown in figure 5.3(b) for two different nanowires (again normalised by the bulk H_c and including the correction for the demagnetisation factor). While this is greater than the superheating field predicted for a planar interface by a factor of approximately 1.25 at 4.2K, at lower temperatures the change in H_p with T is proportional to the rate predicted by the κ dependence given by Matricon [47], as shown by the dotted line. This superheating enhancement of 1.25 is consistent with the enhancement used for

predicting values of H_{c3}. It is possible to get the same values of H_{c3} by increasing the assumed value of $\kappa(0)$ but this would increase the enhancement factor needed for the observed values of H_p suggesting that the original value of $\kappa(0)$ is correct. H_p is larger in the thinner nanowire and in both nanowires the rate at which H_p increases with T near T_c is far greater than predicted, suggesting the presence of strong mesoscopic corrections to the superheating field in these nanowire samples.

Flux entering a superheated type I superconductor would be expected to drive it normal, however surface superconductivity prevents this from happening, allowing a few flux quanta to enter without turning the whole sample normal. Furthermore, it is known that flux within a superconductor can reinforce surface barriers in mesoscopic samples [50] allowing for further superheating of the intermediate state before it eventually becomes unstable leaving only surface superconductivity, which will be strongest near the sharp corners at the ends of the nanowire. The complete disappearance of the intermediate state at $T > 6.1K$ for the 390nm nanowire and $T > 6.4K$ for the 470nm nanowire can be attributed to divergence of the coherence length as the critical temperature is approached, eventually leading to a situation where ξ becomes larger than the width of the nanowire and the intermediate state becomes unstable. A similar effect has been seen by Geim *et al.* [5] as the size of Al superconducting disks was reduced at a fixed temperature. The exact point of disappearance of the intermediate state is predicted for a slab to be $d = 1.84\xi$. This matches well with the results seen here where, using the assumed dependence of $\xi(T)$ from above, in the 390nm nanowire at $6.1K$, $d = (1.8 \pm 0.1)\xi$ and in the 470nm nanowire at $6.4K$, $d = (1.9 \pm 0.1)\xi$, adding extra confidence to the chosen value of $\xi(T)$.

As the magnetic field is reduced for a nanowire in the normal state surface superconductivity will first nucleate around the ends and then spread along the edges before joining up in the middle. Flux through the nanowire is not fully quantised until this happens, a situation that can be recognised by the appearance of definite steps in the magnetization curve. Reducing the field from the normal state metastable trapped flux states are observed for $T \leq 6.1K$ that exist down to fields well below the bulk $H_c(T)$. In this temperature range the system is seen to switch between hierarchies of flux states with progressively reduced vorticity until eventually jumping back to the Meissner state. Transitions between these trapped flux configurations require the system to overcome barriers

between them, and increased thermal fluctuations at higher temperatures greatly reduces their ranges of metastability.

In order to better understand how these magnetisation curves relate to the flux distribution within the samples a series of 3D GL calculations have been performed on cylinders with similar dimensions to these nanowires. Computational overheads restrict the simulations to cylinders that are $1.8\mu m$ long, the calculations for magnetisation are then averaged over the area of the Hall probe to approximate the experimental conditions. The first simulation is shown in figure 5.4 for a 500nm diameter cylinder at 4.2K where $\kappa = 0.3$, this is slightly wider than any of the nanowires that have been measured and so the results cannot be directly compared, but is useful in allowing the visualisation of the possible flux evolution inside a nanowire whilst re-creating some of the features seen in the magnetisation curves. 3D Cooper pair density plots have been included for each vorticity state, L, and from these it is possible relate the progression of the flux distribution to specific features in the magnetisation curves. For instance it can clearly be seen that the nucleation of superconductivity at the ends spreads along the edges before encircling the whole sample. At this point the flux enclosed within is quantised and changes in magnetisation proceed in a more step like fashion, the same behaviour as has already been noted in the experimental data. As the applied field approaches H_c from the Meissner state there is a large amount of superheating and flux penetrating above H_c without driving the whole sample normal, i.e. a superheated intermediate state, again similar to the experimental data. It should also be noted that in this simulation superconductivity first nucleates at $0.92H_c$. For a superconducting slab with $\kappa = 0.3$ surface superconductivity would be expected to nucleate at $0.72H_c$, hence there is an additional enhancement of 1.28 - very similar to the value seen previously.

Figures 5.5(a)-(d) show minor magnetisation loops traced near the superconductor-normal transition from different starting points. Loops either start in the Meissner state, or in the normal state and are tracked to specific metastable states and then the sweep direction reversed in order to determine the stability range of each state. Since the Hall sensor only captures flux from a small fraction of the nanowire, it is difficult to assign exact flux distributions to experimentally observed states. Broadly speaking minor loops that start in the Meissner state approximately overlay those that start from the normal state, but there are several subtle differences which indicate that the flux configurations are not exactly

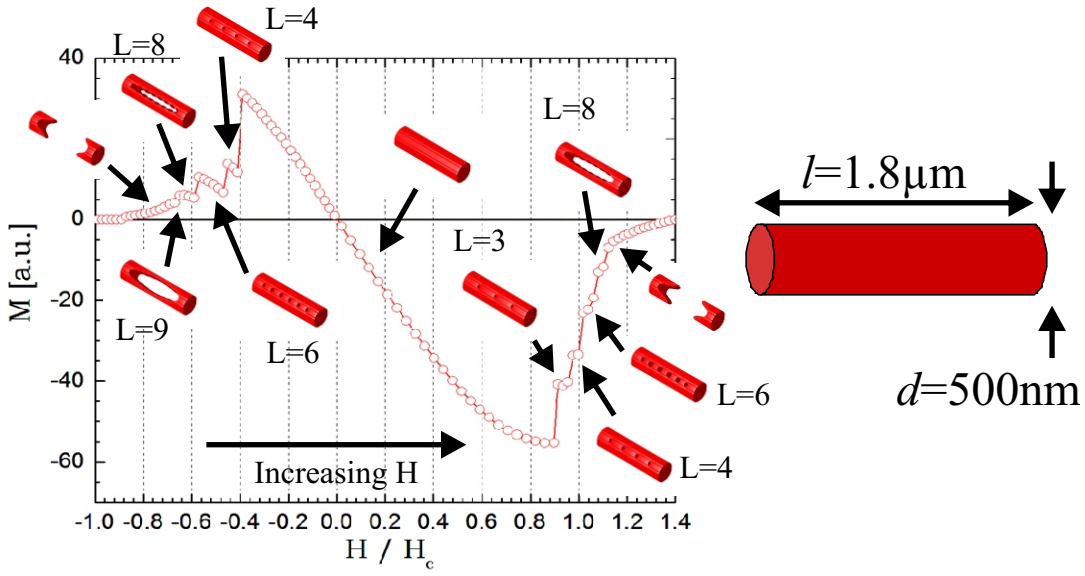

Figure 5.4: 3D GL simulation for a 500nm diameter cylinder at 4.2K with $\kappa = 0.3$ including 3D Cooper pair density plots showing the flux distribution within the cylinder at different fields.

the same in both cases. For example the trace that starts in the Meissner state and backtracks from the intermediate state at 5.2K in figure 5.5(a) appears to overlap the trace from the normal state, but does not jump back to the Meissner state until a somewhat lower field as highlighted at points (i) and (ii). Also the loop in figure 5.5(b) that reaches the same apparent plateau switches at point (iii) to a different higher vorticity intermediate state upon backtracking. Both observations suggest that the two different minor loops prepare slightly different flux configurations, and these differences are located quite far from the Hall sensor. At the higher temperature of 5.6K shown in figure 5.5(c) states starting from the Meissner state and the normal state clearly no longer coincide, and again are stable up to different applied fields indicated by points (iv) and (v). Also, back-tracked plateaux are not all stable out to the main superconducting-normal transition. Indeed the central trapped flux state suddenly increases its vorticity upon back-tracking to higher fields and appears to fall onto the lower trapped flux branch in figure 5.5(d) at point (vi).

It is not possible to determine the exact distribution of flux within the nanowires from these magnetisation measurements alone. The nanowires investigated here are $\approx 20\mu m$ long whilst only the magnetisation of the central $\approx 1 - 2\mu m$ can be directly observed. In order to overcome this limitation a second set of 3D GL calculations has been performed for cylinders with the same diameters as the measured nanowires allowing a more direct comparison between the two sets

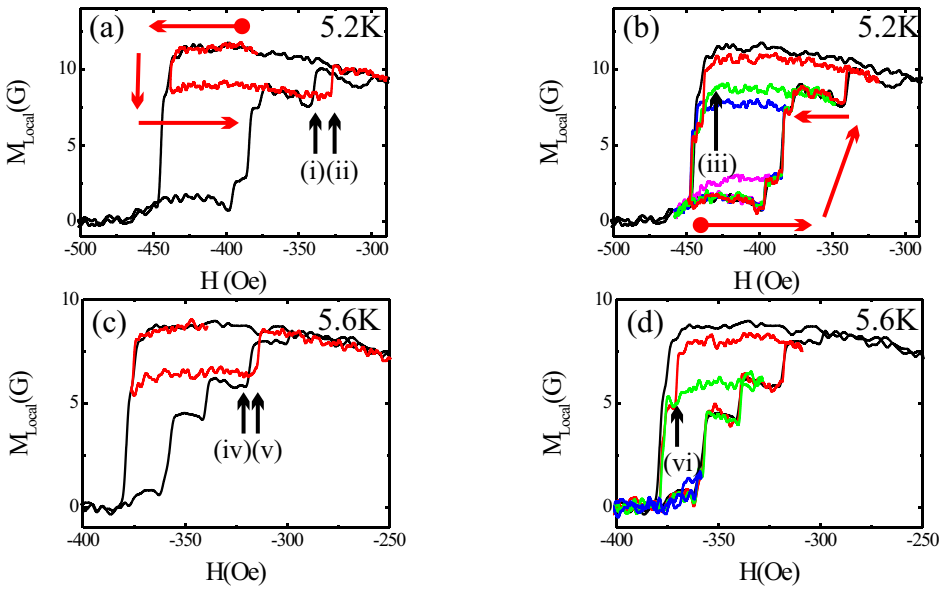

Figure 5.5: Magnetisation minor loops for 390nm diameter nanowire tracing out the full stability range of each vorticity state (as differentiated by different coloured lines) overlaid on top of the main magnetisation curve (black line). The red arrows indicate the direction of field sweep. The black arrows labelled (i) - (vi) relate to points explained in the text.

of results to be made. This is illustrated in figure 5.6 where a comparison is made between measured and calculated data for 390nm and 470nm diameter Pb nanowires at 5.2K. Again there is a restriction to simulations of cylinders that are $1.8\mu m$ long. Whilst there is a large difference in length of the two systems, it can be expected that there will be good agreement for low values of L when confinement due to the ends is weak. For higher values of L there is a greater constriction of flux in the simulated wire than in the measured nanowire making it more difficult to compare the two directly. For instance, in figure 5.6(a) it can be seen that the $L = 4$ state appears to be much more stable experimentally than in the simulated data. It is however almost certain that the longer length of the measured nanowire allows vortex populations to change far from the Hall sensor that do not appear to influence the recorded magnetisation data, or the apparent vorticity.

Agreement between simulation and experiment is not as good for the thinner 390nm diameter nanowire shown in figure 5.6(b). However, in both cases an abrupt discontinuous jump to the superconducting state as the field is reduced can be seen, in stark contrast to rather gradual onset that was observed in the thicker nanowire. Also the intermediate state is stable over a much narrower field range in both the experimental and simulated data when compared to the thicker

nanowire due to the much stronger lateral confinement making flux expulsion easier in this case.

As well as allowing an estimation of the different values of L from the measured magnetisation data to be made, GL simulations are especially useful in determining the likely distribution of flux within the nanowires. Cooper pair density plots, as shown in figure 5.6, highlight the effect of the extreme quantum confinement in the nanowire geometry. Unlike the intermediate state in bulk type I superconductors, which form large normal domains containing multiple flux-quanta, normal regions are 'squeezed' such that only single flux vortices can form in chains along the long axis of the nanowire. This is not always clear for large L from the Cooper pair plots, but can be confirmed by referring to the adjacent corresponding phase plots of the superconducting order parameter.

If it were possible to gradually increase the diameter of the nanowire from the values investigated here it is reasonable to expect to see a crossover at which the behaviour reverts to that of a classic type I superconductor with multi-quanta intermediate domains. There is indeed evidence for this broad trend in these measurements. The flux distribution in the thin nanowire is seen to approximate that of a type II superconductor with evenly spaced single quantum vortices. For the thicker nanowire, however, something intermediate between type I and type II behaviours is observed. Although there is still a chain of single quantum vortices, these are not uniformly distributed along the length of the nanowire, rather they form bunches that are reminiscent of the normal domains in macroscopic type I superconductors. Such bunching is also found to promote even vorticity states and explains the absence of some odd vorticity states (e.g., $L = 5$) in the thicker nanowire.

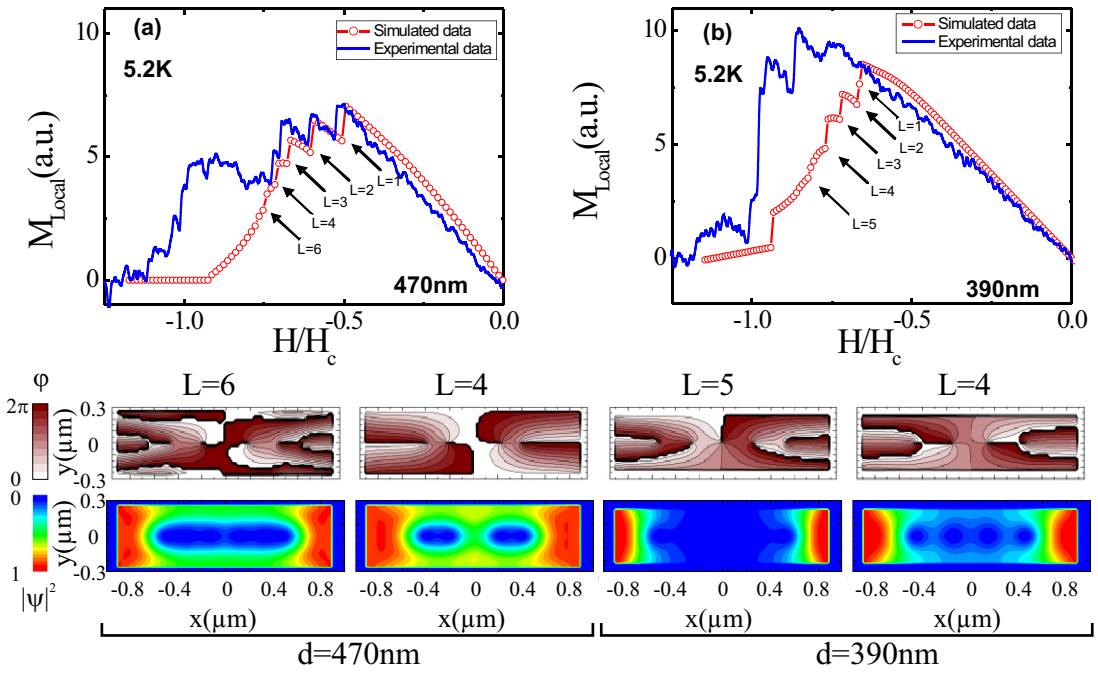

Figure 5.6: Top: Comparison of measured nanowire magnetisations and GL simulations of magnetisations for cylinders with the same diameter. Bottom: Cooper pair density plots, $|\psi|^2$, and phase plots, φ, showing the flux distribution for specific values of L.

Chapter 6

Superconducting Pb Triangles

6.1 Experimental

The Pb triangles were grown via electrodeposition, using the previously described method with an electrolyte of 5mM Pb nitrate and 0.05M nitric acid, by applying a reduction potential of -0.1V versus a Pb wire. The triangles were deposited onto a BDD electrode and immediately moved onto the Hall array, which was kept in an argon atmosphere between positioning each triangle and then placed in the cryostat sample space which was filled with helium. Whilst it is important to follow these steps to avoid allowing the triangles to oxidise, it does mean that the dimensions of the triangles investigated can not be as accurately measured as would be desirable. By measuring the dimensions of triangles deposited under the same conditions using an AFM, see for instance figure 6.1(a), it was found that these triangles have a linear relationship between the length of their sides and their height. They also have sloped sides, the angle of the slope being constant, at about 65°, regardless of the size of the triangle. It was therefore possible to measure the length of the sides of the triangles on the Hall array using an optical microscope and deduce their other dimensions to a reasonable degree of accuracy. Hall Magnetometry measurements were taken with two SR830 digital lock-in amplifiers, one being used to measure the Hall probe with a triangle on whilst the other measured an adjacent blank Hall probe to give a background signal which can later be subtracted from main data to give more accurate readings.

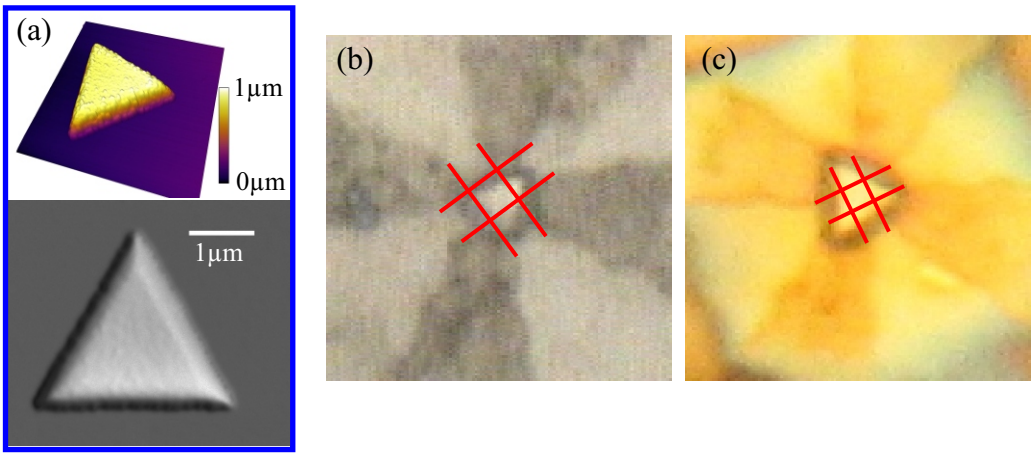

Figure 6.1: (a) AFM and SEM images of typical triangles grown under the same conditions as those measured in this work. (b) Optical image of the smaller triangle, with a base length of $1.8\mu m$, on the Hall probe. The red lines show the location of the Hall cross. (c) Optical image of the larger triangle, with a base length of $2.5\mu m$, on the Hall probe.

6.2 Results

The results described here are for two triangles of different sizes. The larger triangle has a base length of 2.5μm and height of 800nm. The smaller triangle has a base length of 1.8μm and height of 700nm.

Using a similar approach to that employed when examining the nanowire data, figure 6.2 shows measured values of H_{c3} for both triangles normalised by the bulk H_c, and also the measured values of H_p, again normalised by the bulk H_c. The values given for H_p allow for the demagnetising factor, which is estimated for each triangle as being equal to the demagnetising factor of the largest ellipsoid able to fit wholly within the triangle. This works out as approximately 0.5 for the large triangle, meaning the fields around its edge are increased by a factor of 2, and 0.45 for the small triangle, meaning the fields around its edge are increased by a factor of 1.8. As can clearly be seen, the two triangles show quite different behaviour. This is unlikely to be due to their difference in size, both triangles are too large for it to be reasonable to expect any enhancement to H_{c3} above that produced by their geometry at 4.2K. Instead the difference in behaviour can more likely be explained with reference to the triangle's relative position on the Hall probe, shown in figures 6.1(b) and (c). As can be seen in these optical images, most of the small triangle is over the Hall cross, including a corner, while only the central part of the large triangle is above the Hall cross. Hence because surface superconductivity survives up to higher fields in the corners, H_{c3}

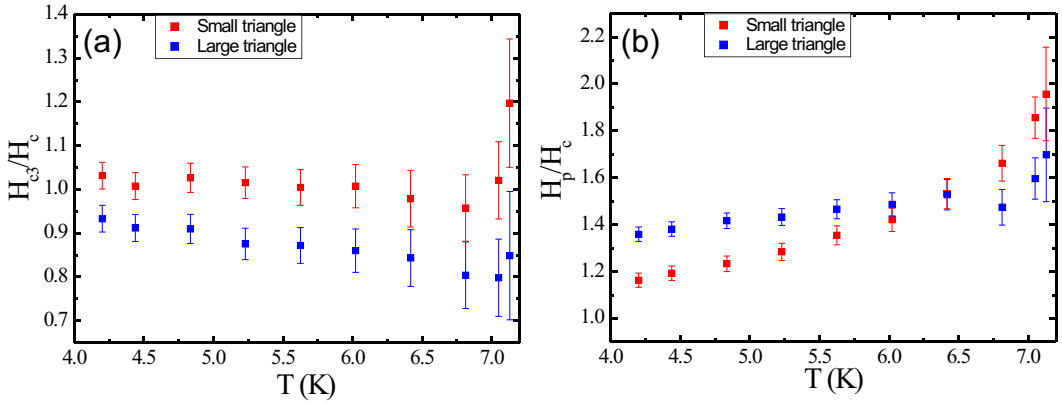

Figure 6.2: (a) Temperature dependence of H_{c3} for both triangles normalised by the bulk value of H_c. (b) Temperature dependence of H_p for both triangles normalised by the bulk value of H_c and allowing for the demagnetising field.

will appear higher in the smaller triangle, which has a corner directly over the Hall cross, than in the larger triangle where its size and position means than not all of the surface superconductivity will be measured. Similarly with the field of first penetration, H_p, flux enters first at the edges and due to the slope of the sides there will be a fairly large difference in field between this point and the point at which flux penetrates into the main body of the superconductor. The much faster rate of increase of H_p with T for the small triangle than for the large triangle can then be explained by the increase in the superconducting lengthscales with temperature, which makes flux penetration in the edges more 'visible' to the large triangle's Hall probe. It is not surprising that the value of H_p in the smaller triangle overtakes that of the larger triangle near T_c, as similar mesoscopic enhancements to those seen in the nanowire data can be expected. A similar situation of converging critical fields at higher temperature is not seen in the case of H_{c3}, as the increase in ξ with T leads to a much greater reinforcement due to size in the smaller triangle.

The values of H_{c3} found here are a factor of approximately 1.3 lower than for the nanowires, despite the predicted reinforcement due to a triangular geometry being higher [39]. Whilst it is possible for the values of κ to be different in the different samples, a far more likely explanation is that the decrease in H_{c3} is due to the sloped sides of the triangles. Indeed it is well known that for a semi-infinite plane, as the angle of applied field is altered so that the field changes from parallel to perpendicular, the nucleation field decreases to H_{c2} at a very rapid rate [109]. The situation here is very different to that of a semi-infinite plane at an angle to a field, making it very difficult to predict the exact decrease in H_{c3} expected

here, but a factor of 1.3 is entirely plausible. Weaker surface supercurrents will also provide weaker barriers to flux entry, and sloped sides provide a reduced geometric barrier compared to straight edges, hence the much lower values of H_p seen here compared to the nanowires.

Figure 6.3 shows magnetisation curves for both triangles at various temperatures. Immediately obvious is the fact that H_{cI}, the point at which superconductivity is destroyed (not counting the tail due to surface superconductivity), is much lower than the bulk value of H_c. This is a well known effect in large, thin slabs. The fact that it is seen here and not in the nanowire measurements is again an indication of the sloped sides providing smaller surface barriers, although such barriers are not totally absent as evidenced by the higher H_{cI} seen here in comparison with a large slab. For instance Cody *et al.* [110] found for thin lead slabs at 4.2K, H_{cI} was lowest for a thickness of roughly 800nm, about the same as the samples here. At this point $H_{cI}/H_c \approx 0.75$ while here for the large triangle $H_{cI}/H_c \approx 0.85$.

In increasing fields from the Meissner state, a major difference between the magnetisation curves of the two triangles is the way flux is seen to penetrate. Flux is seen to penetrate more smoothly in the smaller triangle, at lower temperatures this occurs in single quantum jumps, whereas flux penetrates in much larger jumps which are then stable for longer in the larger triangle. This behaviour however should be expected considering the earlier comments about the position of the triangles on the Hall probes. The Hall probe for the larger triangle mostly only 'sees' the centre of the triangle. Flux will then be seen to penetrate in a manner that is reminiscent of the geometrical barrier - flux will penetrate relatively easily the edges of the triangle but a larger increase in applied field is necessary to push flux up the slope of the triangle. At a critical point flux will reach the flat section and be pushed to the centre, relaxing the magnetic field and thus requiring another large increase in field before another bundle of flux can penetrate into the centre. Similar behaviour would be expected in the smaller triangle if only the field in the very centre was measured.

In decreasing fields from the normal state there are both striking similarities and large differences between the two triangles. As the applied field is decreased superconductivity nucleates around the edges forming a giant vortex in the centre. Surface superconductivity nucleates first at the bottom of the sloped edge but gradually moves further up as the field is reduced more. There is a minimal

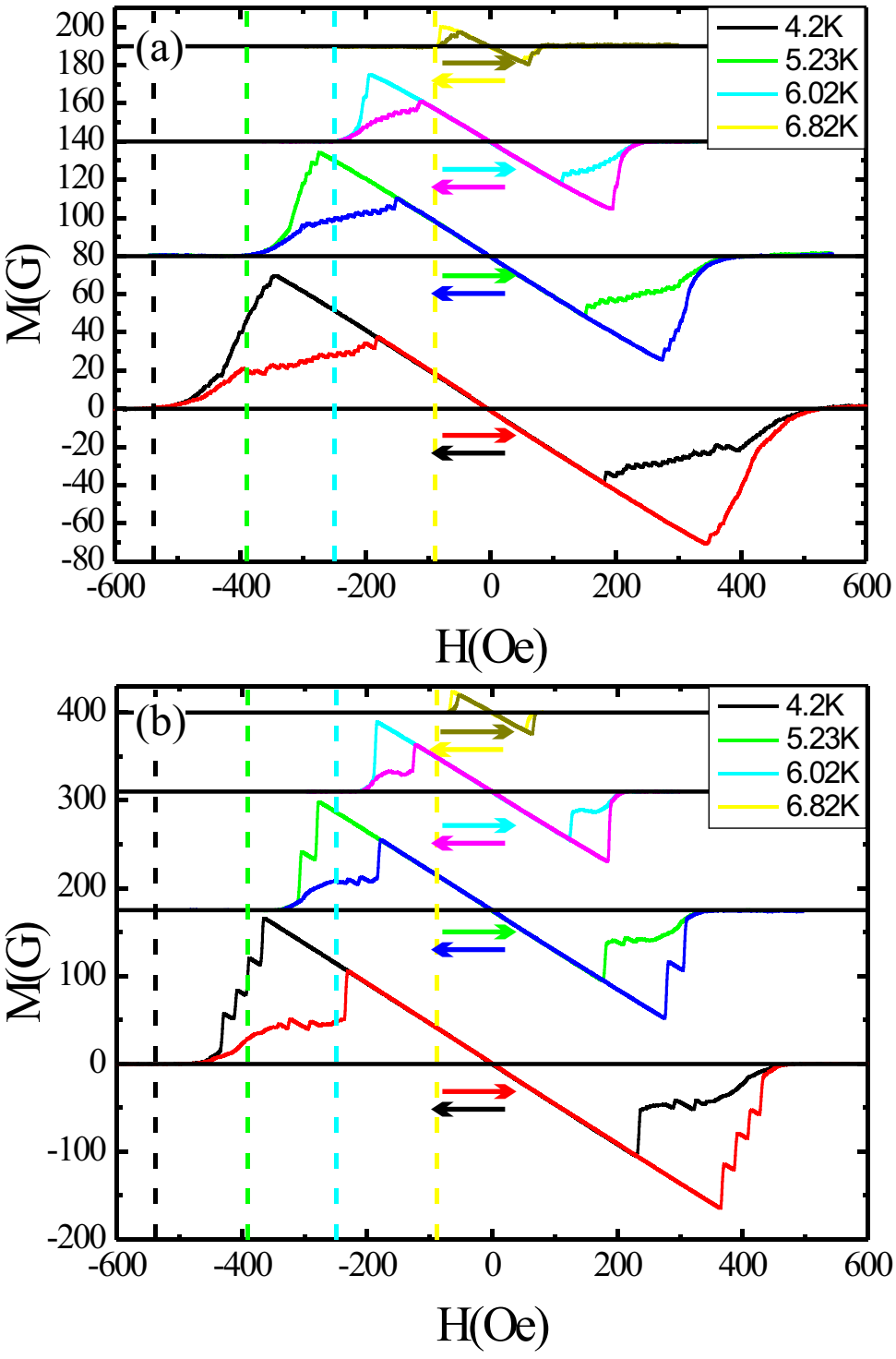

Figure 6.3: Magnetisation curves for the small triangle, (a), and the large triangle ,(b), at various temperatures. Dotted vertical lines indicate the bulk value of H_c. Different colours represent different field sweep directions as indicated by the corresponding arrows.

barrier to flux exit in this region because flux lines will shorten by moving down the slope, hence lowering their energy. This minimal barrier allows flux to exit in single quantum steps, which can be seen quite clearly in the small triangle, but as expected is harder to observe in the larger triangle. When all the flux has been expelled from the sloped edges it suddenly becomes harder for flux to leave the triangles and this is marked by a sudden change in the slope of the magnetisation curve. This point is quite easy to recognise in the large triangle and also in the small triangle at low temperatures, but gets progressively harder as the temperature increases.

As previously explored in the theory section, Pb samples of this thickness are expected to have a laminar period of approximately the same size as these triangles, it is therefore entirely plausible for the flux within these triangles to remain as a single giant vortex. This combination of a single normal domain containing a small number of flux quanta allows this regime to be explored in a novel way. By measuring the size of, and counting the number of all the steps in the magnetisation curve (backtracking from the Meissner state), it is possible to count exactly how many flux quanta are contained within the normal domain. For a type I superconductor the magnetic field within this normal domain should be approximately H_c, hence by multiplying the number of flux quanta by the flux of a single quantum ($20.7G\mu m^2$) and dividing by H_c it is possible to approximate the area of the giant vortex as a function of the applied field. Figure 6.4 shows the area of the giant vortex determined using this method versus the applied field normalised by the bulk H_c for both triangles. Because of the difficulty in counting the number of flux quanta in the large triangle at high fields the area of the giant vortex is plotted from the point at which the slope of the magnetisation curve changes, i.e. the point at which flux is expected to have been expelled from the sloped edges. When looking at this starting point for the large triangle it can be seen that at all temperatures the area is the same to within the quantisation limit - this greatly reinforces the idea that this is an accurate method of measuring the area of the normal domain and that the change in slope seen in the magnetisation curve at this point is due to all flux being expelled from the sloped edges. The same is true for the small triangle at low temperatures, but at higher temperatures (from 5.63K and up) the area at which the slope changes begins to shrink. This is most likely due to the increasing superconducting lengthscales. Note that it was not possible to discern a change in slope in the 6.41K data and so most of the steps have been included.

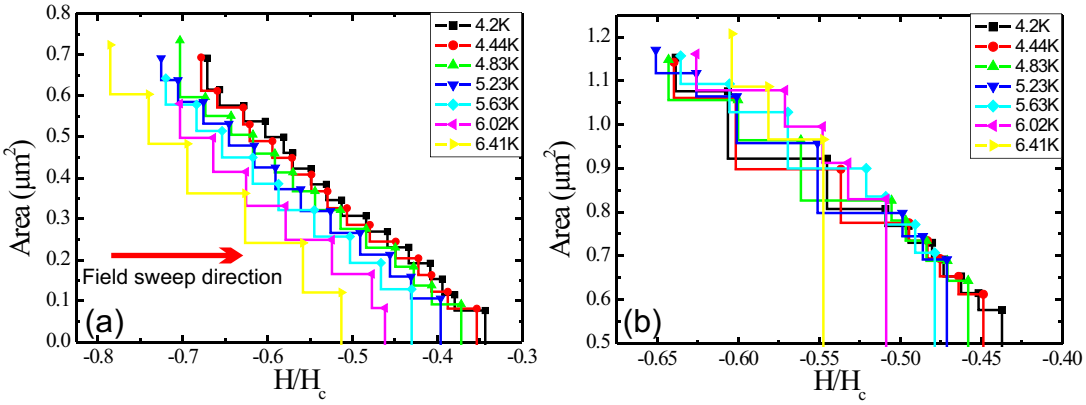

Figure 6.4: Estimated area of the normal domain as a function of the applied field normalised by the bulk H_c for (a) small triangle, (b) large triangle. The red arrow indicates the direction in which the field is swept.

Further understanding of these graphs can be obtained by considering the following: As the field is reduced for a given vorticity, the area of the normal region remains constant, as can be seen by the horizontal lines. Hence the magnetic field outside the triangle relaxes whilst remaining constricted within the normal domain - a type of inverse demagnetising effect. Because the area of the normal domain and the flux density within it remain constant, a plot of the area against the normalised applied field is in effect providing a good measure of the excess field in the normal domain. This excess field will exert an outward pressure on the central flux bundle and when the outward pressure becomes too great an amount of flux will be expelled from the superconductor. It is therefore important to compare how the two triangles react to this. In the large triangle, figure 6.4(b), almost all the switching points between vorticity states fall along the same line for all temperatures. This strongly suggests that there is, as expected, a barrier to flux exit. When the outward pressure from the excess field reaches a critical point this barrier is overcome and flux exits the sample, the fact that this point is consistent across all the temperatures measured suggests that this barrier is independent of lengthscale effects as might be expected for a large superconductor.

The situation is very different for the small triangle, figure 6.4(a). Whilst the gradient of the line along which flux switching takes place is consistent for different temperatures, the field at these points of flux switching is considerably more spread out than was the case for the large triangle. As the temperature increases flux is expelled from the superconductor earlier. This is very similar to the effect seen previously in the narrower nanowire, where increasing confinement as ξ

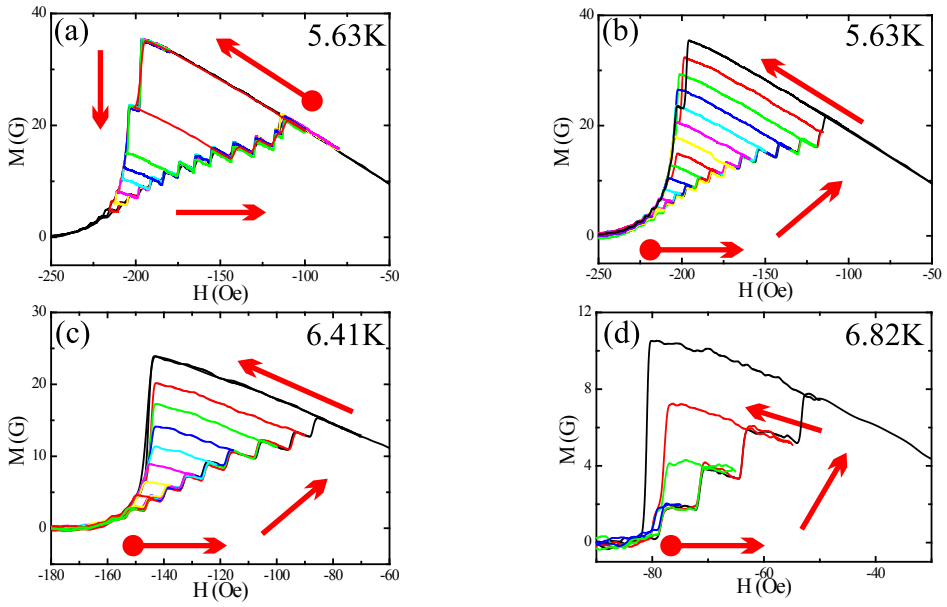

Figure 6.5: Minor loop magnetisation curves tracing out the full stability range of each vorticity state (as differentiated by different coloured lines) overlaid on top of the main magnetisation curve (black line) for the smaller triangle. Arrows indicate the direction of field sweep, the circle shows the starting point.

increases with T causes flux to be expelled earlier, suggesting the same process is happening here. Hence there is strong evidence that the points at which vorticity switches is largely driven by the mesoscopic nature of this sample.

Minor magnetisation loops have been performed for both triangles, figures 6.5 and 6.6, in order to explore the stability of the different vorticity states. At 5.63K, for both triangles, minor loops are performed starting in the Meissner state, sweeping out to an intermediate state and the backtracking all the way back to the Meissner state. A minor loop is then performed in the other direction that starts in the normal state and is taken to the same vorticity state as the intermediate state of the first minor loop before backtracking to the normal state. In both triangles these two loops overlap each other exactly and also backtrack perfectly the other vorticity states. This strongly suggests that, unlike with the nanowires, the flux distribution for a given vorticity state is the same regardless of the route taken to get to that vorticity, as would be expected if the flux was distributed as a single giant vortex.

For other minor loops that start in the normal region and then follow a particular vorticity back to the normal region, it is useful to consider the applied field at which, upon backtracking, additional flux penetrates and the state changes

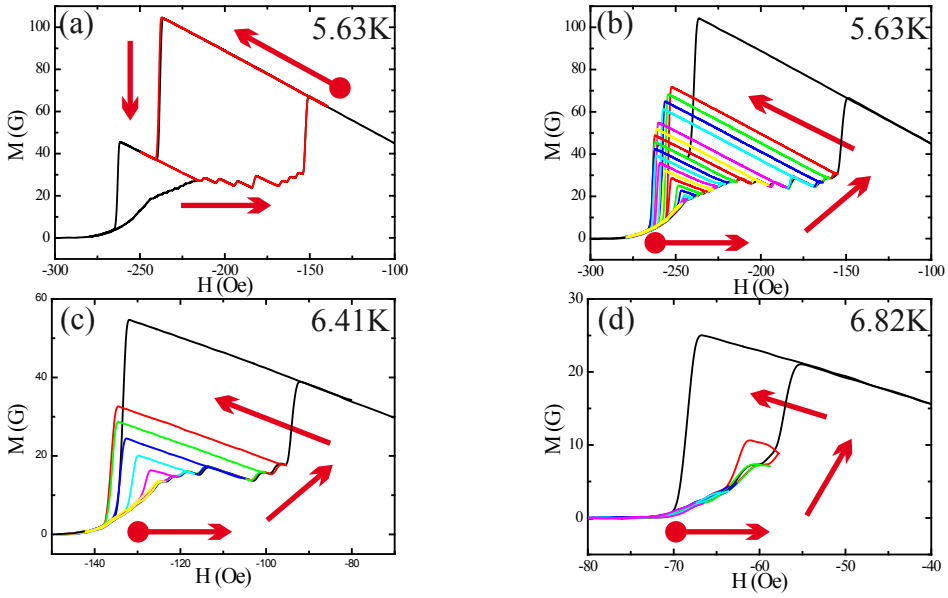

Figure 6.6: Minor loop magnetisation curves tracing out the full stability range of each vorticity state (as differentiated by different coloured lines) overlaid on top of the main magnetisation curve (black line) for the larger triangle. Arrows indicate the direction of field sweep, the circle shows the starting point.

vorticity, i.e. the stability of the state. The observed trend seen in all of these minor loops is most easily explained with reference to figures 6.6 (a) and (b). In figure 6.6 (a) it can be seen that as the applied field is swept so that the superconductor is driven from the Meissner state to the normal state, there exists a single intermediate state. The Meissner state switches to this intermediate state, which has a vorticity of 19, at -237Oe and this state is then stable to -262Oe before the superconductor is driven normal. Figure 6.6 (b) shows a series of vorticity states that return to the normal state at ever increasing applied fields, hence increasing in stability, as the vorticity increases until a vorticity of 19 is reached. This is the most stable vorticity and switches to the normal state at the same point as the intermediate state obtained by sweeping from the Meissner state. Higher vorticity states are then increasingly less stable as the vorticity increases. In cases where there is no intermediate state after flux first penetrates the Meissner state, as seen in figures 6.5 (c) and (d) and figures 6.6 (c) and (d), the lowest vorticity state represents the most stable state, with states becoming less stable as the vorticity increases.

This behaviour can be explained by the way flux penetrates into the triangle from the Meissner state. Because there is a barrier to flux entry, when flux does enter the superconductor it is likely to reach the equilibrium point for that particular

value of applied field and hence stabilities of lower vorticity states will be less but will grow as they approach this vorticity. This same behaviour of jumping to the equilibrium point is seen in bulk superconductors when superheated, or when flux penetrates over the geometrical barrier. The behaviour of higher vorticity states where the range of stability is seen to reduce as the vorticity grows, is explained due to this region representing a giant vortex state that extends into the sloped edges of the triangle. As the vorticity increases the height up the slope to which superconductivity extends reduces, reducing the barrier to flux entry and hence the stability range of the giant vortex state.

3D GL simulations have been carried out for a triangle with the same shape and size as the smaller triangle, as well as for a triangle with the same sized base and height but with straight edges, at 6.4K. Restrictions due to computational overheads have meant that it was not possible to simulate the larger triangle. A comparison of the magnetisation curves for the measured triangle and the simulated sloped edged triangle is shown in figure 6.7(a). All vorticity states in the simulated triangle relate to a single giant vortex, which considering the close match of the two magnetisation curves reinforces the belief that a single giant vortex is also seen in the real triangle. The major difference between the two sets of data is that superconductivity survives up to a slightly higher value in the simulated data than in the real data and H_{c3} is also higher. This could either be due to a difference in the relative superconducting lengthscales, for instance a higher κ would produce a higher value of H_{c3}, or it could be due to a slight difference in geometry. If the slope of the sides was greater than expected in the real triangle, which is not unreasonable as the geometry of this triangle was never measured directly, this would lead to a lower geometrical barrier and also a lower value of H_{c3}.

Figure 6.7(b) shows a comparison of the magnetisation curves for the two simulated triangles at 6.4K. By comparing the two sets of data it becomes apparent how large a role having sloped edges plays. In the triangle with straight edges the field of first penetration is a factor of 1.25 higher than for the triangle with sloped edges, and H_{c3} is a factor of about 1.1 greater. A far greater barrier to flux exit is also witnessed, with a single vortex state surviving down to almost zero applied field. Such weaker surface barriers in sloped edged triangles is perhaps why only giant vortex states are witnessed, rather than the more exotic states predicted by several theoretical papers on mesoscopic triangles e.g. [111], [112].

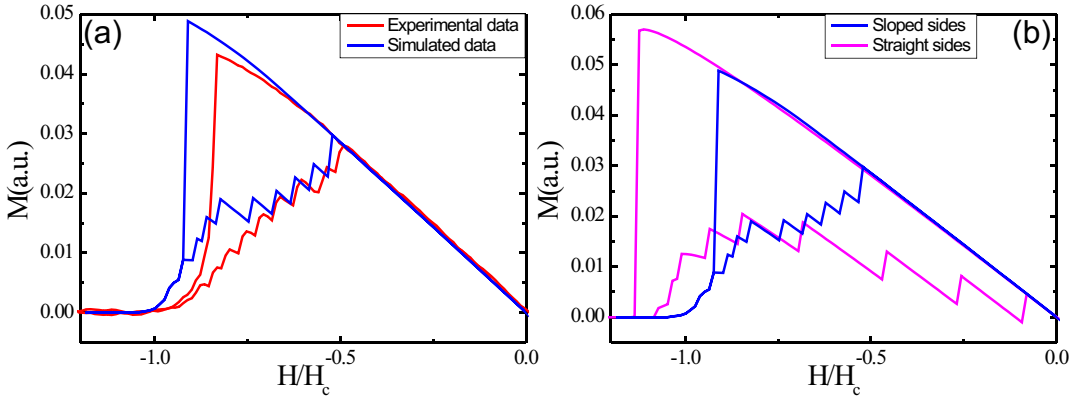

Figure 6.7: (a) Comparison of measured magnetisation of the smaller triangle at 6.41K and GL simulation of the magnetisation for a triangle of the same size at 6.4K. (b) Comparison of simulated magnetisation for a triangle with sloped sides, as with the triangles measured here, and a triangle with straight sides but the same sized base and height.

For instance [113] predicts the vorticity to evolve as defined by a set of "magic" numbers which preserve the triangular symmetry - going so far as predicting the formation of anti-vortices in order to preserve symmetry. Such states can only exist in the presence of very strong surface barriers. As an example consider the case of a giant vortex in a decreasing field. As witnessed in this work, as the field is decreased the excess field will act to pull the giant vortex apart. This is balanced by the associated energy cost of increasing the size of the S/N interface in a type I superconductor. For a sample with a weak barrier to flux exit, as with the triangles here, when the excess field becomes too large flux can simply leave the sample, hence no particular flux hierarchy followed. For a sample with very strong barriers to flux exit, when the excess field becomes large flux is unable to leave the sample, rather the energy cost of the giant vortex splitting into several smaller vortex states is offset by the energy associated with the excess field.

Chapter 7

Superconducting Pb Icosahedron and Tripod

7.1 Introduction

Over the past decade, one of the major research directions in mesoscopic superconductivity was so-called "quantum tailoring", i.e. the engineering of the superconducting properties of the sample by its size and shape [114], [60]. The influence of sample geometry is particularly important for vortex matter, as individual vortices in type-II superconductors were found to strongly interact with the edge currents, due to the small size of the sample in units of characteristic lengthscales. As a result, in superconducting squares, vortex states with total vorticity that are a multiple of four showed enhanced stability [115], [112], and a similar analogy can be drawn for other polygons. However, previous experimental studies have been restricted to thin, flat samples, and electrodeposition enables the next step to be taken in this research - to grow truly three-dimensional, highly faceted samples, where the sample as a whole has distinct geometry, and surfaces are composed of units of very pronounced symmetry. In addition, the material used here (Pb) is a type-I superconductor (in bulk), which makes these microcrystals very different from previously studied samples. It is therefore expected that the properties of these samples would show a very complex interplay between the nucleation of surface superconductivity, surface barriers, geometrical shape, and temperature-dependent lengthscales and the GL parameter.

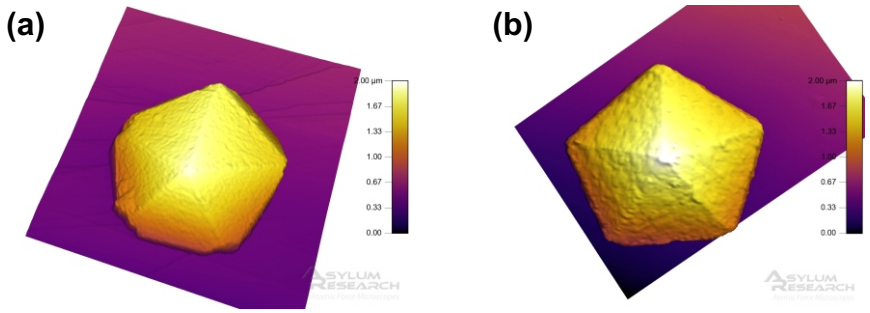

Figure 7.1: AFM images of Pb pentagons deposited from either Pb nitrate solution (a), or Pb acetate solution (b). These images highlight that Pb nitrate solutions give sharp edges with smooth surfaces, while Pb acetate solutions give a rougher surface.

7.2 Experimental

Pb polyhedra can be grown via electrodeposition using a variety of electrolytes. Using Pb nitrate and Pb acetate it is possible to grow a variety of similar structures, however it was found that Pb nitrate allowed the growth of crystals with smoother surfaces and more well defined facets, as illustrated in figure 7.1, and for this reason was used when growing the polyhedra studied here instead of Pb acetate.

The results for two Pb structures are presented here. The first is a half-icosahedron (figure 7.2(a)); an icosahedron that has been sliced through the centre so that it has a flat hexagonal base with a flat triangle on top. The total width of this crystal is about $1.5\mu m$ with each triangular face having a side length of about $1\mu m$. The second is a tripod structure (figure 7.2(b)) that has a triangular base with three legs pointing upwards from each corner. In the studied crystal, each leg is roughly $5\mu m$ long and $0.5\mu m$ wide while the edge of the triangular base is $1\mu m$ long. The Pb crystals were grown by electrodeposition onto a highly oriented pyrolytic graphite substrate (HOPG). An electrolyte of 5mM lead nitrate with a supporting electrolyte of 0.1M nitric acid was used. The half-icosahedron was grown by applying a reduction potential of -0.05V vs. a Pb wire reference electrode for 60s. The tripod was grown by applying a reduction potential of -0.15V for 60s (typical SEM images of these results are shown in figure 7.2(c)).

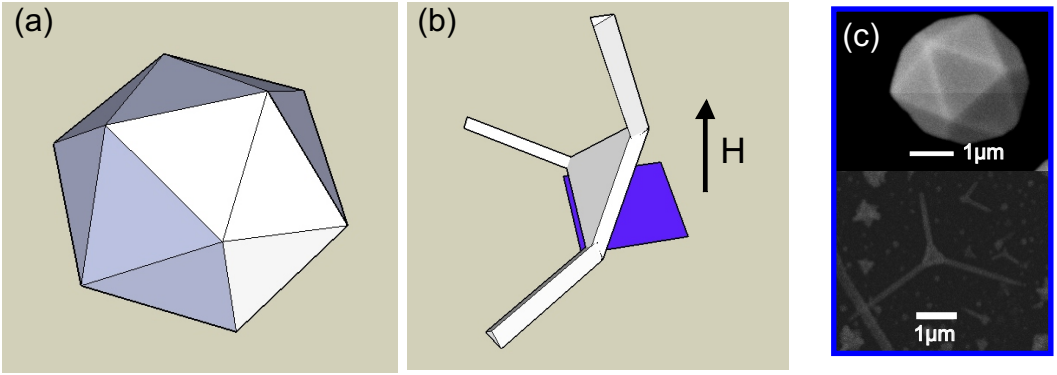

Figure 7.2: (a), (b) Sketches showing the geometry of the two Pb structures that have been investigated. (b) also shows the orientation of the tripod on the Hall probe. The shaded square underneath represents the active area of the Hall probe. (c) SEM images of similar Pb structures to the ones investigated here, grown under the same conditions.

7.3 Results & Discussion

The superconducting properties of the samples are characterised by Hall magnetometry, where the magnetic response of the samples is measured in increasing and decreasing applied magnetic fields, all the way to saturation i.e. full destruction of superconductivity. As already known, flux entry and exit in the samples manifests in the M(H) curves in a step-like, quantized manner. Therefore, by measuring and comparing the size of the jumps in the magnetisation curve it is possible to determine how many quanta of flux are entering or leaving the sample at a given applied field.

7.3.1 Half-icosahedron

Figure 7.3 shows a typical M(H) curve for the half-icosahedron, at 4.9K. As the field is gradually increased the sample exhibits clear Meissner screening up to applied field of 400Oe. Beyond that point, flux penetration is observed over a narrow range of fields before the sample is driven normal at 425Oe, which roughly corresponds to the critical field of bulk Pb at that temperature. First flux entry during the sweep-up is measured to be up to 3 flux quanta, corresponding to the jump labelled b in figure 7.3. A suggested likely flux distribution for this case is given in figure 7.4. The subsequent jump in the M(H) curve corresponds to the entry of 6 flux quanta, followed by another 6 before the sample transits to the normal state. For the reverse sweep (sweep-down), superconductivity is first recovered at the lateral surfaces. This results in a gradual quantisation of the flux

in decreasing fields, and vortex states nucleate in a "giant" form. Note also that formation of multi-quanta vortices is favourable due to the type I nature of the sample. The state labelled g is believed to represent a giant vortex where a large normal area is located in the centre of the sample, encircled by a superconducting area. As the field is decreased further, the vortex states are back tracked to the point of flux expulsion. Using the same methodology, it is established that flux leaves in multiples of 3 flux-quanta, and the states with vorticity 15 (state f), 12 (e), and 3 (b) are identified. The last observed state is actually a single-vortex state (a). Therefore, based on the combined results of up- and down- sweeps, it is reasonable to conclude that flux entry and exit are guided by the C3 symmetry of the upper facet of the crystal as well as the C3 symmetric arrangement of identical facets on the sloped sides of the sample. The single vortex state is recovered in the measurement as it never conflicts with the symmetry of flat polygonal samples.

To verify this, the measurement was repeated at a higher temperature, 5.6K. The M(H) curve shown in figure 7.3 does not show any flux penetration on the sweep up and the sample remains in the Meissner state up to the critical magnetic field. In the reverse sweep however, very similar flux penetration to the 4.9K measurement is seen. The sequence is slightly different, with transitions in vorticity of $15 \rightarrow 12 \rightarrow 6 \rightarrow 3$ and eventually back to the Meissner state. Therefore, at both temperatures the size of the flux jumps is found to be dependent on the geometry of the sample. As flux enters or leaves, it must do so in a way that preserves the symmetry of the vortex state with respect to the complex shape of the crystal. The latter shape is best described in terms of the C3 symmetry of the facets and their spatial arrangement, hence most jumps in M(H) characteristics correspond to multiples of 3 flux quanta.

7.3.2 Tripod

Geometrically speaking, the tripod studied here is a far more complex structure than the half-icosahedron. Therefore, the magnetisation curves (see figure 7.5) exhibit extremely complicated behaviour, which is very difficult to interpret in terms of vortex arrangements. However, one prominent and novel result is observed - the large amount of flux trapped in this structure as the applied field changes polarity. In addition, it is observed that flux trapping diminishes with increasing temperature.

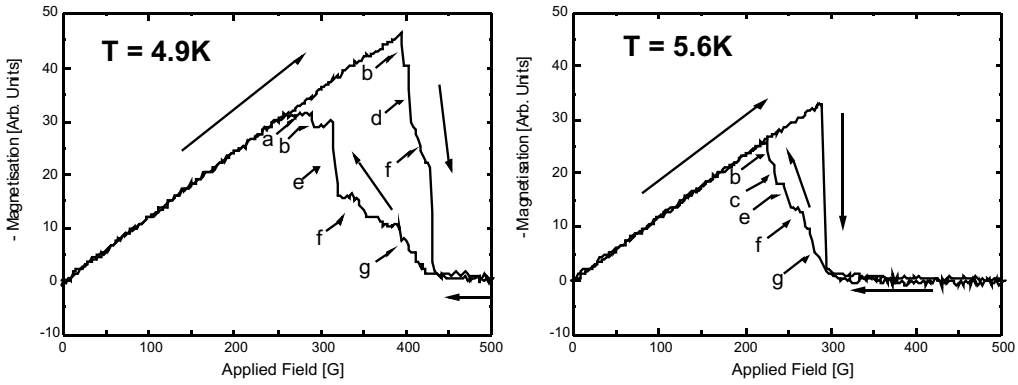

Figure 7.3: Magnetisation curve for the half-icosahedron at 4.9K and 5.6K. Labelled steps refer to flux distribution shown in figure 7.4.

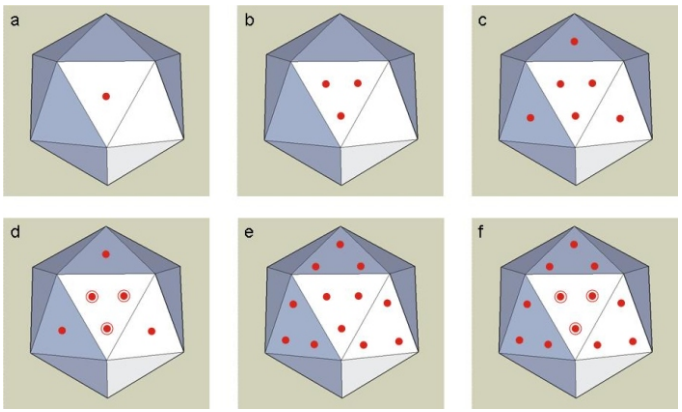

Figure 7.4: Possible flux distribution for specific flux quantisations. Double circles represent two flux quanta. Areas labelled g in figure 7.3 refer to a giant vortex of varying vorticity and a representation of this has not been included here.

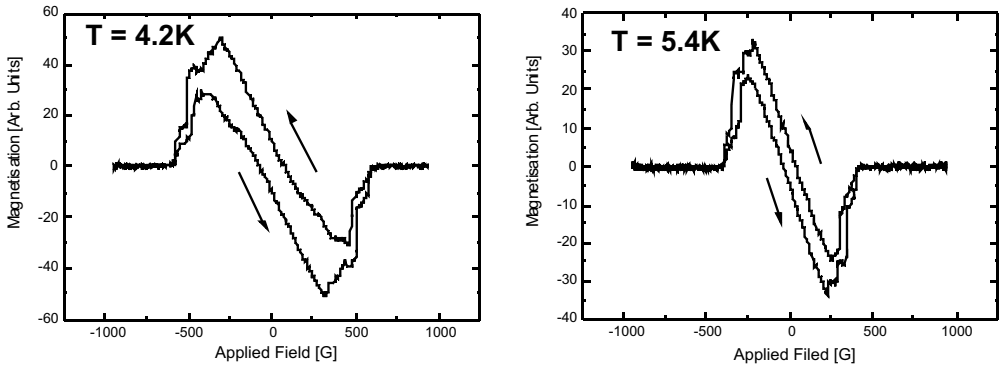

Figure 7.5: Magnetisation curves for the tripod at 4.2K and 5.4K. Arrows show the direction of field sweep.

To shed light on this phenomenon, one must take into account the position of the structure of the Hall bar (see figure 7.2(b)), which strongly suggests that flux remains trapped in the vertically standing leg of the tripod. Based on the earlier nanowire results, nanowires with similar dimensions to those of the tripod's legs have shown no such flux pinning when they lie perpendicular to the direction of the applied field. At present, no plausible explanation of this behaviour can be offered, but this measurement is reported as an illustration of the richness and complexity of the flux matter in truly 3D superconducting samples.

Chapter 8

Conclusions and Further Work

During the course of this work Hall array magnetometry measurements have been used to measure the magnetic response of a variety of individual Pb mesoscopic crystals grown by electrodeposition.

8.1 Hall Magnetometry Results

Results for Pb nanowires of different diameters, when combined with 3D GL simulations, clearly demonstrate that geometrical confinement in these quasi-1D systems leads to intermediate and trapped flux states composed of discrete single quantum vortices. Underlying such distinctly type II behaviour there are nevertheless characteristic type I signatures: pairs of vortices are sometimes found to 'bind' into vortex molecules, strongly reminiscent of type 1.5 superconductivity that has recently been identified in the two-band superconductor MgB_2 [116], and the hierarchy of observed flux distributions exhibits preferred vorticity states. Mesoscopic effects are seen to greatly increase the critical fields in line with theory, and predictions for the temperature dependence of superconducting lengthscales have been made that are consistent with both the measurements and simulations.

Two different sized 3D Pb triangles with sloped edges were investigated and found to display significant differences in behaviour. Whilst mesoscopic effects can be seen in both triangles, specifically an increase in H_{c3} as $T \rightarrow T_c$, flux exit in the larger triangle is seen to be largely independent of the temperature suggesting

that it is too large for mesoscopic effects to play a role in this particular aspect. Conversely flux in the smaller triangle is seen to be increasingly 'squeezed' out as the temperature is increased by ever increasing confinement, an effect similar to the results seen in the nanowire measurements. Comparisons are made with GL simulations that highlight the importance of geometry on driving the formation of flux structures. The sloped edges of the measured triangles is seen to drastically reduce surface barriers allowing flux to enter and leave the sample far easier than would be expected from a similar sample with straight edges. These lower barriers in turn allow the flux within the superconductor to form a single giant vortex in a fairly typical display of type I superconductivity.

A different approach was taken for analysing the magnetisation results for a Pb icosahedron. By measuring and comparing the size of the steps in the magnetisation curves at different temperatures it was possible to see that flux enters in bundles of a size guided by the 3-fold symmetry of the sample. As it was clear the flux was being driven by the symmetry of the sample it was then possible to postulate how the flux is likely to be distributed within it. In the same chapter a tripod was also examined, but complex the shape produced an equally complex magnetisation curve making understanding the corresponding flux behaviour very difficult. The large overall size made the tripod too big to perform GL simulations on but one aspect of the results was worth noting, namely the large amount of temperature dependent flux trapping. One possible position for flux to be trapped is in the vertical leg of the tripod, which when considering the previously measured behaviour of perpendicular nanowires suggests a very different set of behaviour would be observed in nanowires in different orientations.

8.2 Further Work

There are a number of natural extensions to the work presented here. As the nanowires became thicker, their behaviour appeared to change from that of a type II superconductor to something approaching that of a type I superconductor. By investigating progressively thicker wires a more accurate picture of this transition can be obtained.

The ability to perform accurate GL simulations of the investigated systems is limited to a degree by the uncertainty in the superconducting parameters. Transport measurements can be used to determine these parameters and while contacts can

be made most easily to nanowires, indeed similar measurements have already been carried out by other groups [108], transport measurements have been made on other superconducting mesostructures in the past [6]. Being able to apply contacts can also enable these superconductors to be used in practical applications, for instance superconducting nanowires have been used as single photon detectors [117]. By knowing the superconducting parameters to a greater degree of accuracy it would then become useful to be able to 'tune' these parameters. This could be achieved by depositing metal alloys and controlling the percentage of each metal, a good candidate system would be tin/lead alloys.

Better control of the electrodeposition, for instance the ability to reproducibly deposit the same shaped structures on a large area, is desired for practical uses of microcrystals but this would also allow other methods of investigation to be employed. For instance the Bitter decoration technique allows the direct observation of flux distribution within a mesoscopic superconductor but it is somewhat destructive to the sample being measured, hence to gain a good idea of the flux evolution over a range of fields and temperatures large arrays of similar structures need to be produced so that small numbers of structures can be measured at a particular field and temperature for many different fields and temperatures, e.g. [118]. Other magnetic imaging techniques are unlikely to be successful with these samples, for instance magneto optical imaging does not have the required resolution for such small samples and scanning techniques are best suited to flat samples, rather than the 3D microcrystals measured during the course of this work.

References

[1] R. Prozorov. Equilibrium topology of the intermediate state in type-I superconductors of different shapes. *Physical review letters*, 98(25):257001, 2007.

[2] L.D. Landau. Unbranched model of intermediate state. *Phys. Z. Sowjetunion*, 11:129–138, 1937.

[3] A.D. Hernández and D. Domínguez. Magnetic properties of the intermediate state in small type-I superconductors. *Physical Review B*, 72(2):20505, 2005.

[4] V.V. Moshchalkov, L. Gielen, C. Strunk, R. Jonckheere, X. Qiu, C.V. Haesendonck, and Y. Bruynseraede. Effect of sample topology on the critical fields of mesoscopic superconductors. *Nature*, 373:319–322, 1995.

[5] A. K. Geim, I. V. Grigorieva, S. V. Dubonos, J. G. S. Lok, J. C. Maan, A. E. Filippov, and F. M. Peeters. Phase transitions in individual sub-micrometre superconductors. *Nature*, 390(6657):259–262, 1997. 10.1038/36797.

[6] A. Kanda, B.J. Baelus, F.M. Peeters, K. Kadowaki, and Y. Ootuka. Experimental evidence for giant vortex states in a mesoscopic superconducting disk. *Physical review letters*, 93(25):257002, 2004.

[7] Z.L. Xiao, C.Y. Han, W.K. Kwok, H.H. Wang, U. Welp, J. Wang, and G.W. Crabtree. Tuning the architecture of mesostructures by electrodeposition. *J. Am. Chem. Soc*, 126(8):2316–2317, 2004.

[8] M.J. Van Bael, J. Bekaert, K. Temst, L. Van Look, V.V. Moshchalkov, Y. Bruynseraede, G.D. Howells, A.N. Grigorenko, S.J. Bending, and G. Borghs. Local observation of field polarity dependent flux pinning by magnetic dipoles. *Physical Review Letters*, 86(1):155–158, 2001.

[9] H.K. Onnes. The resistance of pure mercury at helium temperatures. *Communications from the Physical Laboratory of the University of Leiden*, 120b, 1911.

[10] H.K. Onnes. The liquefaction of helium. *Communications from the Physical Laboratory of the University of Leiden*, 108:3–23, 1908.

[11] H.K. Onnes. The sudden disappearance of the ordinary resistance of tin, and the super-conductive state of lead. *Communications from the Physical Laboratory of the University of Leiden*, 133:61–68, 1913.

[12] W. Meissner and R. Ochsenfeld. Ein neuer effekt bei eintritt der supraleitfähigkeit. *Naturwissenschaften*, 21(44):787–788, 1933.

[13] F. London and H. London. The electromagnetic equations of the supraconductor. *Proceedings of the Royal Society of London. Series A, Mathematical and Physical Sciences*, 149:71–88, 1935.

[14] F. London. *Superfluids: Macroscopic theory of superfluid helium*, volume 1. Wiley, New York, 1950.

[15] V.L. Ginzburg and L.D. Landau. On the theory of superconductivity. *Zh. Eksper. Teor. Fiz*, 20:1064–1082, 1950.

[16] L.D. Landau. On the theory of phase transformations II. *Soviet Phys. JETP*, 11:627, 1937.

[17] J. Bardeen, L.N. Cooper, and J.R. Schrieffer. Microscopic theory of superconductivity. *Physical Review*, 106(1):162–164, 1957.

[18] P.G. De Gennes. *Superconductivity of metals and alloys*. W.A. Benjamin, New York, 1966.

[19] M. Tinkham. *Introduction to superconductivity*. McGraw-Hill, 1996.

[20] A.B. Pippard. An experimental and theoretical study of the relation between magnetic field and current in a superconductor. *Proc. Roy. Soc.*, A216:547–568, 1953.

[21] A.A. Abrikosov. On the magnetic properties of superconductivity of the second type. *Soviet Phys. JETP*, 5:1174–1182, 1957.

[22] K. Fossheim and A. Sudbo. *Superconductivity: Physics and Applications*. John Wiley & Sons, 2005.

[23] H.F. Hess, R.B. Robinson, R.C. Dynes, J.M. Valles Jr, and J.V. Waszczak. Scanning-tunneling-microscope observation of the Abrikosov flux lattice and the density of states near and inside a fluxoid. *Physical review letters*, 62(2):214–216, 1989.

[24] W.H. Kleiner, L.M. Roth, and S.H. Autler. Bulk solution of Ginzburg-Landau equations for type II superconductors: Upper critical field region. *Phys. Rev*, 133(5A):1226–1227, 1964.

[25] J. Pearl. Current distribution in superconducting films carrying quantized fluxoids. *Applied Physics Letters*, 5:65–66, 1964.

[26] J.A. Osborn. Demagnetizing factors of the general ellipsoid. *Physical Review*, 67(11-12):351–357, 1945.

[27] E.D. Torre. *Magnetic hysteresis*. IEEE Press, 2000.

[28] D.E. Farrell, R.P. Huebener, and R.T. Kampwirth. Direct observation of growth of the landau domain structure. *Solid-State Commun.*, 11(12):1647–1649, 1972.

[29] R.P. Huebener. *Magnetic flux structures in superconductors*. Springer-Verlag Berlin, 1979.

[30] P.G. de Gennes. *Superconductivity of Metals and Alloys*. Addison-Wesley, 1989.

[31] L.D. Landau and E.M. Lifshitz. *Electrodynamics of Continuous Media*. Pergamon Press, 1960.

[32] F.E. Harper and M. Tinkham. The Mixed State in Superconducting Thin Films. *Physical Review*, 172(2):441–450, 1968.

[33] G.D. Cody and R.E. Miller. Parallel and Perpendicular Magnetic Transitions of Superconducting Films and Foils of Lead. *Physical Review Letters*, 16(16):697–701, 1966.

[34] V.S. Egorov, G. Solt, C. Baines, D. Herlach, and U. Zimmermann. Superconducting intermediate state in white tin near Hc: new results by μSR. *Physica B: Physics of Condensed Matter*, 289:393–395, 2000.

[35] J. Feder and D.S. McLachlan. Superheating and supercooling in single spheres of tin, indium, and gold-plated indium. *Physical Review*, 177(2):763–776, 1969.

[36] D. Saint-James and P.G. De Gennes. Onset of superconductivity in decreasing fields. *Phys. Lett*, 7(5):306–308, 1963.

[37] A.C. Rose-Innes and E.H. Rhoderick. *Introduction to superconductivity*. Pergamon Oxford, 1969.

[38] H.J. Fink. Vortex Nucleation in a Superconducting Slab near a Second-Order Phase Transition and Excited States of the Sheath near H_{c3}. *Physical Review*, 177(2):732–737, 1969.

[39] V.A. Schweigert and F.M. Peeters. Influence of the confinement geometry on surface superconductivity. *Physical Review B*, 60(5):3084–3087, 1999.

[40] H.T. Jadallah, J. Rubinstein, and P. Sternberg. Phase transition curves for mesoscopic superconducting samples. *Physical Review Letters*, 82(14):2935–2938, 1999.

[41] A. Houghton and F.B. McLean. Nucleation of superconductivity in wedge geometry. *Physics Letters*, 7:172–174, 1965.

[42] A.P. Van Gelder. Nucleation of Superconductivity above H_{c3}. *Physical Review Letters*, 20(25):1435–1436, 1968.

[43] D.A. Dikin, V. Chandrasekhar, V.R. Misko, V.M. Fomin, and J.T. Devreese. Nucleation of superconductivity in mesoscopic star-shaped superconductors. *The European Physical Journal B*, 34(2):231–235, 2003.

[44] C.P. Bean and J.D. Livingston. Surface barrier in type-II superconductors. *Physical Review Letters*, 12(1):14–16, 1964.

[45] P.G. De Gennes. Vortex nucleation in type II superconductors. *Solid State Communications*, 3:127–130, 1965.

[46] Orsay Group on Superconductivity. *Quantum Fluids, Proceedings of the Sussex University Symposium 16-20 August 1965*. North-Holland Publishing Company, 1966.

[47] J. Matricon and D. Saint-James. Superheating fields in superconductors. *Physics Letters, A*, 24, 1967.

[48] M.P. Garfunkel and B. Serin. The Formation of a Boundary between Normal-Conducting and Superconducting Metal. *Physical Review*, 85(5):834–840, 1952.

[49] J. Feder, S.R. Kiser, and F. Rothwarf. Superheating and supercooling in the superconducting transition of small indium spheres. *Physical Review Letters*, 17(2):87–89, 1966.

[50] A.D. Hernández and D. Domínguez. Surface barrier in mesoscopic type-I and type-II superconductors. *Physical Review B*, 65(14):144529, 2002.

[51] J. Provost, E. Paumier, and A. Fortini. Shape effects on the magnetization of superconducting lead at 4.2 K. *Journal of Physics F: Metal Physics*, 4:439–448, 1974.

[52] L.D. Landau and E.M. Lifshitz. *Theoretical Physics, Vol. 8, Electrodynamics of Continuous Media*. Pergamon Press, 1984.

[53] A. Fortini and E. Paumier. Thermodynamics of metastable processes in the magnetization of type-I superconductors. *Physical Review B*, 14(1):55–60, 1976.

[54] A. Fortini, A. Hairie, and J.P. Girard. First-stage magnetization and metastable migration field in a type I superconducting slab. *Journal of Mathematical Physics*, 20:2139, 1979.

[55] E. Zeldov, A.I. Larkin, V.B. Geshkenbein, M. Konczykowski, D. Majer, B. Khaykovich, V.M. Vinokur, and H. Shtrikman. Geometrical barriers in high-temperature superconductors. *Physical Review Letters*, 73(10):1428–1431, 1994.

[56] M.V. Indenbom and E.H. Brandt. Comment on "Field Induced 3D to 2D Crossover of Shielding Current Path in $Bi_2Sr_2CaCu_2O_x$". *Physical Review Letters*, 73(12):1731–1731, 1994.

[57] J.R. Clem, R.P. Huebener, and D.E. Gallus. Gibbs free-energy barrier against irreversible magnetic flux entry into a superconductor. *Journal of Low Temperature Physics*, 12(5):449–477, 1973.

[58] M. Benkraouda and J.R. Clem. Magnetic hysteresis from the geometrical barrier in type-II superconducting strips. *Physical Review B*, 53(9):5716–5726, 1996.

[59] N. Morozov, E. Zeldov, M. Konczykowski, and R.A. Doyle. Geometrical and distributed surface barriers in $Bi_2Sr_2CaCu_2O_8$. *Physica C: Superconductivity and its applications*, 291(1-2):113–131, 1997.

[60] L.F. Chibotaru, A. Ceulemans, V. Bruyndoncx, and V.V. Moshchalkov. Symmetry-induced formation of antivortices in mesoscopic superconductors. *Nature*, 408(6814):833–834, 2000.

[61] E.S. Sadki, S. Ooi, and K. Hirata. Focused-ion-beam-induced deposition of superconducting nanowires. *Applied Physics Letters*, 85:6206, 2004.

[62] W. Li and P.A. Warburton. Low-current focused-ion-beam induced deposition of three-dimensional tungsten nanoscale conductors. *Nanotechnology*, 18:485305, 2007.

[63] G. Yi and W. Schwarzacher. Single crystal superconductor nanowires by electrodeposition. *Applied Physics Letters*, 74:1746, 1999.

[64] S. Michotte, L. Piraux, F. Boyer, F.R. Ladan, and J.P. Maneval. Development of phase-slip centers in superconducting Sn nanowires. *Applied Physics Letters*, 85:3175, 2004.

[65] A. Müller, S.E.C. Dale, M.A. Engbarth, S.J. Bending, and L.M. Peter. Shape-controlled electrodeposition of tin crystals from Sn (II)-fluoroborate solutions. *CrystEngComm*, 2010.

[66] P.T. Kissinger and W.R. Heineman. *Laboratory techniques in electroanalytical chemistry*. Marcel Dekker Inc, 1996.

[67] I.V. Markov. *Crystal growth for beginners*. World scientific River Edge, NJ, 1995.

[68] K. Sangwal. Growth kinetics and surface morphology of crystals grown from solutions: Recent observations and their interpretations. *Progress in Crystal Growth and Characterization of Materials*, 36(3):163–248, 1998.

[69] E. Budevski, G. Staikov, and WJ Lorenz. Electrocrystallization nucleation and growth phenomena. *Electrochimica Acta*, 45(15-16):2559–2574, 2000.

[70] J.W. Gibbs. *The Collected works Volume I*. Yale university press, 1948.

[71] M. Volmer and A. Weber. Keimbildung inubersattigten gebilden. *Z. phys. Chem*, 119:277–301, 1926.

[72] R. Becker and W. Doring. The kinetic treatment of nuclear formation in supersaturated vapors. *Ann. Phys*, 24:719–752, 1935.

[73] L. Frakas. *Z. phys. Chem*, 125:236, 1927.

[74] J.W. Mullin. *Crystallization*. Butterworth-Heinemann Boston, 2001.

[75] J.V. Zoval, R.M. Stiger, P.R. Biernacki, and R.M. Penner. Electrochemical Deposition of Silver Nanocrystallites on the Atomically Smooth Graphite Basal Plane. *J. Phys. Chem*, 100(2):837–844, 1996.

[76] KK Cline, M.T. McDermott, and R.L. McCreery. Anomalously slow electron transfer at ordered graphite electrodes: influence of electronic factors and reactive sites. *The Journal of Physical Chemistry*, 98(20):5314–5319, 1994.

[77] R.M. Penner. Mesoscopic metal particles and wires by electrodeposition. *Journal of Physical Chemistry B-Condensed Phase*, 106(13):3339–3353, 2002.

[78] J.L. Barton and J.O.M. Bockris. The electrolytic growth of dendrites from ionic solutions. *Proceedings of the Royal Society of London. Series A, Mathematical and Physical Sciences*, pages 485–505, 1962.

[79] K.I. Popov, M.D. Maksimović, J.D. Trnjančev, and M.G. Pavlović. Dendritic electrocrystallization and the mechanism of powder formation in the potentiostatic electrodeposition of metals. *Journal of Applied Electrochemistry*, 11(2):239–246, 1981.

[80] K.I. Popov, N.V. Krstajic, R.M. Pantelic, and S.R. Popov. Dendritic electrocrystallization of lead from lead nitrate solution. *Surface Technology*, 26(2):177 – 183, 1985.

[81] S. Ino. Epitaxial growth of metals on rocksalt faces cleaved in vacuum. II. Orientation and structure of gold particles formed in ultrahigh vacuum. *J. Phys. Soc. Jpn*, 21:346, 1966.

[82] S. Ino and S. Ogawa. Multiple twinned particles at earlier stages of gold film formation on alkalihalide crystals. *J. Phys. Soc. Jpn*, 22(6):1365–1374, 1967.

[83] J.G. Allpress and J.V. Sanders. The structure and orientation of crystals in deposits of metals on mica. *Surface Science*, 7(1):1–25, 1967.

[84] L.D. Marks. Experimental studies of small particle structures. *Reports on Progress in Physics*, 57:603–603, 1994.

[85] V.G. Gryaznov, J. Heydenreich, A.M. Kaprelov, S.A. Nepijko, A.E. Romanov, and J. Urban. Pentagonal symmetry and disclinations in small particles. *Crystal Research and Technology*, 34(9):1091–1119, 1999.

[86] G. Wulff. On the question of speed of growth and dissolution of crystal surfaces. *Zeitschrift Fur Krystallographie Und Mineralogie*, 34(5/6):449–530, 1901.

[87] W.L Winterbottom. Equilibrium shape of a small particle in contact with a foreign substrate. *Acta Metallurgica*, 15:303–310, 1967.

[88] L.D. Marks. Modified Wulff construction for twinned particles. *J. Cryst. Growth*, 61:556–566, 1983.

[89] L.D. Marks. Surface structure and energetics of multiply twinned particles. *Philosophical Magazine A*, 49(1):81–93, 1984.

[90] R. De Wit. Partial disclinations. *Journal of Physics C: Solid State Physics*, 5:529–534, 1972.

[91] M.M. Krishtal. Fivefold twins or disclinations?(Discussion). *Metal Science and Heat Treatment*, 49(3):108–110, 2007.

[92] A. Howie and L.D. Marks. Elastic strains and the energy balance for multiply twinned particles. *Philosophical Magazine A*, 49(1):95–109, 1984.

[93] G. Wranglén. Dendrites and growth layers in the electrocrystallization of metals. *Electrochimica Acta*, 2:130–146, 1960.

[94] E.H. Hall. On a new action of the magnet on electric currents. *American Journal of Mathematics*, 2(3):287–292, 1879.

[95] A. Oral, S.J. Bending, and M. Henini. Real-time scanning Hall probe microscopy. *Applied Physics Letters*, 69:1324–1326, 1996.

[96] A.K. Geim, S.V. Dubonos, J.G.S. Lok, I.V. Grigorieva, J.C. Maan, L.T. Hansen, and P.E. Lindelof. Ballistic hall micromagnetometry. *Applied Physics Letters*, 71:2379–2381, 1997.

[97] C.G. Smith. Low-dimensional quantum devices. *Reports on Progress in Physics*, 59:235–282, 1996.

[98] R. Dingle, H.L. Störmer, A.C. Gossard, and W. Wiegmann. Electron mobilities in modulation-doped semiconductor heterojunction superlattices. *Applied Physics Letters*, 33:665–667, 1978.

[99] S.J. Bending and A. Oral. Hall effect in a highly inhomogeneous magnetic field distribution. *Journal of Applied Physics*, 81(8):3721–3725, 1997.

[100] X.Q. Li and F.M. Peeters. Scattering on circular inhomogeneous magnetic field profiles in an electron waveguide junction. *Superlattices and microstructures*, 22(2):243–248, 1997.

[101] C.W.J. Beenakker and H. van Houten. Magnetotransport and nonadditivity of point-contact resistances in series. *Physical Review B*, 39(14):10445–10448, 1989.

[102] C.J.B. Ford, S. Washburn, M. Büttiker, C.M. Knoedler, and J.M. Hong. Influence of geometry on the Hall effect in ballistic wires. *Physical review letters*, 62(23):2724–2727, 1989.

[103] A.K. Geim, I.V. Grigorieva, J.G.S. Lok, J.C. Maan, S.V. Dubonos, X.Q. Li, F.M. Peeters, and Y.V. Nazarov. Precision magnetometry on a submicron scale: magnetisation of superconducting quantum dots. *Superlattices and microstructures*, 23(1):151–160, 1998.

[104] C.W.J. Beenakker and H. van Houten. Billiard model of a ballistic multiprobe conductor. *Physical Review Letters*, 63(17):1857–1860, 1989.

[105] A. Kastalsky and J.C.M. Hwang. Study of persistent photoconductivity effect in n-type selectively doped AlGaAs/GaAs heterojunction. *Solid State Communications*, 51(5):317–22, 1984.

[106] S. Ishii, E.S Sadki, S. Ooi, Y. Ochiai, and K. Hirata. Superconducting properties of lead nanowires fabricated by electrochemical deposition. *Physica C: Superconductivity*, 426:268–272, 2005.

[107] G. Stenuit, S. Michotte, J. Govaerts, and L. Piraux. Vortex matter in lead nanowires. *The European Physical Journal B*, 33(1):103–107, 2003.

[108] G. Stenuit, S. Michotte, J. Govaerts, and L. Piraux. Temperature dependence of penetration and coherence lengths in lead nanowires. *Superconductor Science and Technology*, 18(1):174–182, 2005.

[109] K. Yamafuji, E. Kusayanagi, and F. Irie. On the angular dependence of the surface superconducting critical field. *Physics Letters*, 21(1):11–13, 1966.

[110] G.D. Cody and R.E. Miller. Magnetic Transitions of Superconducting Thin Films and Foils. I. Lead. *Physical Review*, 173(2):481–493, 1968.

[111] L.F. Chibotaru, A. Ceulemans, V. Bruyndoncx, and V.V. Moshchalkov. Vortex entry and nucleation of antivortices in a mesoscopic superconducting triangle. *Physical Review Letters*, 86(7):1323–1326, 2001.

[112] V.R. Misko, V.M. Fomin, J.T. Devreese, and V.V. Moshchalkov. Stable vortex-antivortex molecules in mesoscopic superconducting triangles. *Physical review letters*, 90(14):147003, 2003.

[113] C. Carballeira, G. Teniers, VV Moshchalkov, LF Chibotaru, and A. Ceulemans. Vortex states inside the superconducting phase of a thin microtriangle. *EPL (Europhysics Letters)*, 75:936–942, 2006.

[114] A.K. Geim, S.V. Dubonos, I.V. Grigorieva, K.S. Novoselov, F.M. Peeters, and V.A. Schweigert. Non-quantized penetration of magnetic field in the vortex state of superconductors. *Nature*, 407(6800):55–57, 2000.

[115] B.J. Baelus and F.M. Peeters. Dependence of the vortex configuration on the geometry of mesoscopic flat samples. *Physical Review B*, 65(10):104515, 2002.

[116] V. Moshchalkov, M. Menghini, T. Nishio, QH Chen, AV Silhanek, VH Dao, LF Chibotaru, ND Zhigadlo, and J. Karpinski. Type-1.5 Superconductivity. *Physical review letters*, 102(11):117001, 2009.

[117] G.N. Goltsman, O. Okunev, G. Chulkova, A. Lipatov, A. Semenov, K. Smirnov, B. Voronov, A. Dzardanov, C. Williams, and R. Sobolewski. Picosecond superconducting single-photon optical detector. *Applied Physics Letters*, 79:705, 2001.

[118] IV Grigorieva, W. Escoffier, J. Richardson, LY Vinnikov, S. Dubonos, and V. Oboznov. Direct observation of vortex shells and magic numbers in mesoscopic superconducting disks. *Physical review letters*, 96(7):77005, 2006.